ECMWF LIBRARY

EUROPEAN CENTRE FOR MEDIUM RANGE WEATHER FORECASTS

TECHNICAL REPORT NO. 7

****

October 1977

A TEN-DAY HIGH-RESOLUTION NON-ADIABATIC SPECTRAL INTEGRATION; A COMPARATIVE STUDY

By

A.P.M. Baede and A.W. Hansen
EUROPEAN CENTRE FOR MEDIUM RANGE WEATHER FORECASTS

Fitzwilliam House
Skimped Hill
Bracknell, Berkshire
United Kingdom

1. Introduction

Until recently the main emphasis in the development of NWP models has been with grid-point models. Consequently such models have been tested extensively as to their forecasting capabilities. Indeed several studies have been published dealing with the medium range weather forecasting potentiality of such models (Miyakoda et al (1971); Druyan et al (1975); Somerville et al (1974)). Lately extensive comparative studies were published by ECMWF (Arpe et al (1976); Gauntlett et al (1977).

Less study has been devoted to spectral models although from a numerical point of view such models seem fully competitive to grid-point models. Bourke (1974) published results of a series of short range forecasts with a rhomboidal (J = 15) low resolution multi-level spectral model for the southern hemisphere. Little physical parameterization was included and only RMS difference scores were presented. Later a more extensive study was undertaken by Bourke et al (1977). Their southern hemisphere 24 h and 48 h forecasts with a semi-implicit 7-level rhomboidal J = 15 model were compared with a filtered baroclinic grid-point model and found to have superior RMS and S1 skill scores both at 500 mb and mean sea level pressure, although shortcomings were noticed consistent with the low horizontal resolution and the data problems in the southern hemisphere. A comparable study was published by Daley et al (1976A and 1976B), based on over a year operational experience with a semi-implicit model with moist processes included. This 5-level model had a horizontal rhomboidal J = 20 resolution, although occasionally a J = 30 integration was performed. A comparison with 36 h grid-point model forecasts on the basis of some objective skill scores led them to the conclusion that the spectral model is highly competitive in terms of both accuracy and computational efficiency.

In order to study the climatology of their spectral model and to evaluate the parameterization of physical processes, Bourke et al (1977) undertook a simulation of the January climatology using again a rhomboidal (J = 15) truncation and the GFDL levels (Miyakoda(1973)) in the vertical. The physical parameterizations were close to those used by GFDL and by us in this study. A horizontal ∇^2 diffusion in the top half of the rhomboid was applied. In spite of the relatively low resolution a fair simulation of the January climatology was obtained. This study also showed the suitability of the semi-implicit technique for such studies, although no comparison was made with an explicit integration. These studies showed that spectral models, even with low resolution and with semi-implicit time integration compare favourably with grid-point models as far as short range numerical weather forecasting or climate simulations are concerned. However,no studies have been published on the problem of extended range forecasting with relatively high horizontal resolution. It was decided to undertake a study in this area within the framework of the sequence of studies at ECMWF on the frequently used data set of 1st March 1965. Preliminary studies of different aspects of low resolution integrations are discussed elsewhere (Hansen and Baede, 1977). In this report we discuss a semi-implicit integration with maximum attainable resolution (triangular M = 40), limited by ECMWF's present computer resources. Similar work is undertaken at present at GFDL (T.Gordon, private communication).

Section 2 presents a very brief description of the model for the rest referring to a previous report (Hansen and Baede (1977)).

In Section 3 the results are discussed and compared with both the NMC analyses and the results of other grid-point integrations. The main emphasis is put on a comparison with an integration with the N48 GFDL model. A synoptic comparison as well as conventional objective scores are applied. Moreover the energetics of the integration are examined, including the heat balance of the atmosphere, subject to the physical parameterizations. Some attention is given to a comparison of the precipitation forecasts of the different models.

Finally in Section 4 the conclusions of this study are summarised.

After completion of this report, preliminary results became available of of 10-day integration of ECMWF's grid-point model with GFDL physics and a horizontal resolution corresponding to N48. In an annex to this report we present a preliminary comparison of this integration with T40.

2. The Model

The model, used in this study was the same as the T21 model described in Hansen and Baede (1977). A comprehensive description of its adiabatic part can be found in Hoskins and Simmons (1975). We limit the discussion here to a brief description of the spectral representation and the finite difference approximations in the vertical and in time.

Spectral expansions were truncated in a triangular way as follows :

$$x(\lambda,\mu) = \sum_{m=-M}^{+M} \sum_{n=m}^{M} X_n^m P_n^m(\mu)\, e^{im\lambda}$$

where $P_n^m(\mu)$ is an associated Legendre polynomial of the first kind. With the computer resources, available at present at ECMWF a maximum resolution of M = 40 could be achieved. This model will be referred to as T40.

The vertical σ-coordinate grid was defined as follows (Miyakoda, 1973):

$$\sigma_k = S_k^2 (3-2S_k),\ S_k = \frac{2k-1}{18},\ k = 1,2,\ldots.,\ 9$$

giving nine levels.

Vertical advection terms are approximated by the following scheme :

$$(\sigma\frac{\partial x}{\partial\sigma})_k \rightarrow \frac{1}{2\Delta\sigma_k}\left[\sigma_{k+\frac{1}{2}}(x_{k+1} - x_k) + \sigma_{k-\frac{1}{2}}(x_k - x_{k-1})\right]$$

The integration of the hydrostatic equation is carried out as follows :

$$\phi_k - \phi_{k+1} = \alpha_k(T_k + T_{k+1}), \alpha_k = \tfrac{1}{2}\ln\frac{\sigma k+1}{\sigma_k}$$

The lowest half layer is assumed to be isothermal and therefore

$$\phi_9 - \phi_* = \alpha_9 T_9,\ \alpha_9 = \ln\frac{1}{\sigma_9}$$

in which ϕ_* is the geopotential at the surface. This procedure is different from the one used in GFDL's model (N48) and ECMWF's models (D24,D48) in that in these models the integration proceeds from half level to half level, followed by an averaging to calculate the geopotential at the full levels.

The conversion term $\kappa T\frac{\omega}{p}$ in the thermodynamic equation is computed such as to conserve the total energy in combination with the above described integration of the hydrostatic equation.

The semi-implicit time stepping technique described by Hoskins and Simmons was used, allowing a time step length of 20 minutes. No attempt was made to integrate the model explicitly, because the available computer time was prohibitive. For the reference temperature profile around which the gravity wave terms are linearised we chose the horizontal σ-surface mean temperature.

That the choice of the reference temperature field is by no means trivial, was discussed recently by Simmons et al (1977). They showed that the semi-implicit scheme may become unconditionally unstable if the local static stability differs significantly from the reference static stability. We however did not encounter such problems, perhaps because our vertical resolution is insufficient for this effect to become apparent.

A linear ∇^4 horizontal diffusion was applied to all prognostic quantities except the surface pressure with a diffusion coefficient $K = 4.8 \times 10^{15} m^4 sec^{-1}$. This number was chosen as to produce the same e-folding time of 36 h for the shortest waves as in the T21 integrations, described in Hansen and Baede (1977).

For a description of the GFDL physical parameterization package, which was applied unchanged in this study, we refer to Miyakoda (1973) and to previous reports in this series (Arpe et al, 1976; Gauntlett et al, 1977; Hansen and Baede, 1977). Suffice it to give a summary here in Table I.

Physical Parameterization	Type and Comments
1. Radiation	Manabe and Strickler (1964) / Manabe and Wetherald (1967). Radiation calculation is dependent on: (i) Climatological distribution of absorbers (H_2O, CO_2, O_3) (ii) Climatological surface temperature for sea and sea ice points. (iii) Specified zonal mean cloudiness. (iv) Specified limits of sea ice extent. (v) Time dependent surface albedo influenced by snow, soil moisture, ice. (vi) Specified absorptivity, reflectivity and height of zonal mean clouds.
2. Vertical Diffusion	Mixing length hypothesis. $\ell = 0$ at 2.5 km. No vertical diffusion of temperature.
3. Surface Fluxes	Bulk aerodynamic formulae. $C_d = 0.002$.
4. Convection (moist and dry)	Energy conserving convective adjustment type. Critical relative humidity for onset of moist adjustment = 0.8.
5. Hydrology	Account taken of rainfall, evaporation, snow accumulation, snow melt and run-off.

TABLE I : Summary of physical parameterization included in all models discussed in this report.

In this report the T40 integrations will be compared with other integrations, which are indicated by symbols.
Table II explains the meaning and refers to the description of these models and integrations. It should be stressed that, apart from the horizontal numerical schemes, the differences between these models are found in the horizontal diffusion and the integration of the hydrostatic equation. The physical parameterizations in all integrations are identical. For this reason Table II represents also information about the applied horizontal diffusion scheme.

Symbol	Meaning	Horizontal Diffusion	Reference
T40	This integration	$K.\nabla^4 X, K=4.8\text{x}10^{15} m^4 s^{-1}$	This report
T21	Low resolution spectral integration	$K.\nabla^4 X, K=6.0\text{x}10^{16} m^4 s^{-1}$	Hansen and Baede,1977
T48	GFDL N48 9-layer model	Non-linear diffusion (Smagorinsky)	Arpe et al, 1976, Miyakoda,1973.
D24	ECMWF grid-point model 9-layer N24 version	$K.\nabla^2 X, K=2.5\text{x}10^5 m^2 s^{-1}$	Gauntlett et al,1977
NL2	ECMWF grid-point model. 9-layer N24 version	Non-linear diffusion $K.\lvert\nabla^2 X\rvert.\nabla^2 X$ (K is variable-dependent)	Gauntlett et al,1977
D48	ECMWF grid-point model. 9-layer N48 version	Non-linear diffusion $K.\lvert\nabla^2 X\rvert.\nabla^2 X$ (K is variable-dependent)	Gauntlett et al,unpubl
NMC	Set of NMC analyses of forecast period	-	Arpe et al, 1976.

TABLE II: The models referred to in this report

3. Results

As already stated in the introduction, the main emphasis in the discussion of the results will be put on a comparison with the N48 GFDL grid-point model. This is done by using the comprehensive diagnostic package, used also in previous studies (re. for example Arpe et al, 1976). Following roughly the same plan as used by Gauntlett et al (1977) in their study of an extended range integration with ECMWF's grid-point model, we start with a synoptic comparison on the basis of 500 mb and 1000 mb maps and supported by some Hovmöller diagrams. Next RMS errors and anomally correlation coefficients will be compared followed by an examination of the energetics of the integrations. Some attention will be paid to a comparison of precipitation forecasts of different models.

3.1 Synoptic Comparison

The experiment is based on the 1st March 1965 00Z data set, which was obtained from GFDL. This case has been studied extensively, both by groups at GFDL (Miyakoda et al, 1970, 1971, 1974) and at ECMWF (Arpe et al, 1976; Gauntlett et al, 1977). For a synoptic description of the development on the northern hemisphere during the ten days following this date we refer to these publications.
Rather than comparing the maps in detail, we shall select some striking extra-tropical features in both the 500 mb and the 1000 mb maps (see figs. 3.1.1 - 3.1.21).

3.1.1 Synoptic Comparison at 500 mb

a.) Anticyclone South of Greenland

The development of this anticyclone and its degeneration to a ridge at 30° W during the first three days is rather well predicted. As in the N40 run, the position of the high at day 2 is too far to the West. At day 3 the ridge is at the correct position and the intensity, although weaker than reality, is predicted better than by any other model.

b.) The Trough-Ridge System over E. Atlantic and W. Europe

The further development of the ridge described in the previous section, together with the trough over W. Europe is vital for the synoptic evolution over W. Europe later on in the forecast period. In reality this system moves slowly to the east, the ridge maintaining its identity and developing into a high at the end of the period. In the N48 run the ridge is much too weak already by day 3 and indeed over the whole period. This seems related to the general failure to maintain the double frontal structure over the Atlantic and Europe.

Although the intensity of the trough-ridge system is slightly better in the T40 integration than in the others, the displacement is much too fast. At day 5 the phase difference is about 20^{o}, with T40 forecasting the ridge over W. Europe, where in reality the trough is found. This can also be observed in the Hovmöller diagrams of wavenumbers 4 - 9 at 50^{o}N (fig. 3.1.24).

Referring to the maps, we observe that T40 predicts a weakening of the ridge after day 6 and the appearance of a new eastward moving ridge, which by day 9 is slightly west of the British Isles. Note that this is not the ridge which is found there in reality.

c.) The Double Ridge over Central Asia

The T40 prediction of the development of this system during the first three days is comparable to the N48 forecast. The eastward shift is well predicted. As in all other forecasts the intensity of the most westerly ridge is overestimated, whereas the opposite is true for the most easterly one.

d.) The Lows over the United States

Initially the analysis shows the formation of an intense cut off low at 110^{o} W due to an outbreak of cold air on the east flank of a ridge along the east coast. This low moves slowly to the east to join an already existing low at the west coast by day 6, together intensifying the Canadian trough. Neither of the models is able to simulate this development properly, particularly after day 2. The T40 integration is no exception.

At day 3 a new low is formed off coast by another outbreak of cold air. This low remains fairly stationary. In the N48 run the development of the second low takes place from the Continent rather than from the Pacific. In T40 instead the formation of a second low can be followed from day 6, much too late and too far to the east. Both models fail completely in forecasting this development.

e.) Arctic and Sub-Tropical Front

During the whole forecast period the analysis clearly shows the existence of two fronts between 140^{o} W and 120^{o} E. None of the models is able to reproduce this feature. This is also seen in figure 3.1.22 which shows the zonally averaged meridional temperature gradients. All models reproduce the subtropical front, be it too weak. The arctic front is absent in all models after day 3, although the T40 run seems to produce a new arctic front after day 8.

3.1.2 Synoptic Comparison at 1000 mb

a.) The Initial Cyclone near New Foundland

This cyclone is in reality almost stationary, only slightly moving to the NE, and has by day 4 developed into a double system because it is joined by a cyclone, moving eastwards over the United States of America. The T21 integration was the only one which described this development adequately at least till day 6. The hope that T40 might do even better, was unfounded. Already, on day 1 the low is further south than in reality or any of the other integrations. It then starts moving north-eastwards, much too early. Moreover the low approaching over the United States of America is too weak, although much better forecast than by the N48. As in the N48 the NE moving low develops into an intense cyclone off the Norwegian coast, quite different from the observed development.

b.) Low Pressure Area over Europe during First Half of the Period

The low pressure area over Europe consists mainly of two cyclones. The cyclone over S. Europe moves to the NE, which was well predicted by all models, except that the spectral model shows too fast a movement, resulting in a displacement of ten or more degrees. The other cyclone over N. Europe propagates southward, reaching France by day 4. In the forecasts this movement stops near Scotland.

c.) Siberian High

The Siberian high is almost stationary during the first five days with slightly fluctuating intensity. In the second half of the forecast period the high pressure area weakens and splits up in different cells. In the forecasts the decay starts earlier. Both spectral models show a revival of the high during the last day.

d.) Cyclogenesis near Japan

In both reality and the models a low is formed around day 2 near Japan. The NMC analyses show a rather slow development of this low, which intensifies only when it combines with an already existing low over the Pacific. All models exhibit a much faster development, T40 being the fastest of all. This model reaches its maximum intensity by day 4, whereas both N48 and NMC analyses reach their maximum intensity by day 6. All low resolution models underestimate the intensity of this system.

Hovmöller diagrams are a convenient way of presenting the development of atmospheric waves, particularly in spectral space. Figures 3.1.23 and 3.1.24 show Hovmöller's diagrams for the 500 mb geopotential height at 50N for two wavenumber regimes : the planetary waves n = 1 - 3 and the baroclinic waves n = 4 - 9. As already found in previous studies on the same data set, all models show a considerable skill in predicting the evolution of the phase of the planetary waves. The predicted amplitude of these waves however is continuously decreasing unlike reality. Figure 3.1.23 shows that the T40 model is no exception. In fact, comparing N48 and T40 in detail, there is little to choose between both models.

Clearly, the quality of the forecasts of the baroclinic waves is lower. We have already noted the high phase speeds in the Eastern Atlantic and W. European area. In this regard the N48 seems to be the better forecast. In other details T40 seems superior, for example the development of the trough starting at around 130°E where N48 predicts a wrong intensity. A peculiarity which is evident from this figure is the large increase in amplitude of the systems during the later part of the forecasts. In fact all models and to a lesser extent also the observed circulation show a minimum baroclinic activity half way during the forecasting period. N48 however shows a much stronger recovery than T40.
This point will be discussed later on in more detail.

Summarising, we must conclude that there is little to choose between the N48 and T40 integrations. The phase change of the longest waves is well described, but important failures can be noticed in both models in the prediction of synoptic systems.

3.2 Conventional Objective Verification

Let us begin with saying a few words about the definition and the properties of the verification scores that will be presented. Two verification scores are selected: the anomaly correlation coefficient and the RMS-error.

We define (Miyakoda et al, 1972) the error of a quantity Z as

$$\delta Z(t) = Z_p(t) - Z_t(t)$$

where $Z_p(t)$ and $Z_t(t)$ are the predicted and observed (true) values of Z at time t. Furthermore we define the anomaly:

$$\Delta Z(t) = Z(t) - Z_n$$

where Z_n is the climatological monthly mean, taken from Jenne (1969). Averaging over the N-hemisphere north of 20°N is indicated by a bar $\overline{}$.

The anomaly correlation coefficient C_a is now defined as:

$$C_a(t) = \frac{\overline{\Delta Z_p(t) \cdot \Delta Z_t(t)}}{\sqrt{\overline{(\Delta Z_p)^2}} \quad \sqrt{\overline{(\Delta Z_t)^2}}}$$

For an accurate formulation of C_a in the wavenumber groups we refer to Arpe et al (1976). C_a has the important property that it will approach zero asymptotically for $t \to \infty$.

The RMS error is defined as :

$$\mathrm{rms}(t) = \sqrt{\overline{(\delta Z)^2}}$$

This quantity is always compared with two no-skill scores : the RMS-error of persistence :

$$\mathrm{rmsp}(t) = \sqrt{\overline{[Z_t(t) - Z_t(0)]^2}}$$

and the normal RMS-error :

$$\mathrm{NORM} = E\sqrt{\overline{[\Delta Z_t(t)]^2}^{\,t}}$$

Here the averaging operator $\overline{}^{\,t}$ indicates space averaging over the N-hemisphere north of 20°N, followed by time averaging over all days of the appropriate month. The operator E indicates an ensemble mean over six individual months of NMC data of the years 1965 - 1970.

It can be shown that the asymptotic level of the RMS-error of persistence is $\sqrt{2}$ times the normal RMS-error.

$$\lim_{t \to \infty} \mathrm{rmsp}(t) = \sqrt{2} \cdot \mathrm{NORM}$$

The asymptotic level of the RMS-error is the same, if $\overline{\Delta Zp(t)^2} = \overline{\Delta Z_t(t)^2}$:

$$\lim_{t \to \infty} rms(t) = \sqrt{2}.NORM$$

provided that predicted and observed values have the same spatial variance and the model has no systematic bias. If however the predicted values have much smaller spatial variance than the observed, as is the case in T21, the RMS-error approaches NORM asymptotically:

$$\lim_{t \to \infty} rms(t) = NORM \text{ if } \overline{\Delta Z_p(t)^2} << \overline{\Delta Z_t(t)^2}$$

If $\overline{\Delta Z_t^2} = NORM^2$ and $\overline{\Delta Z_p^2} = \alpha^2 . NORM^2$ then the following relation between rms (t) and $C_a(t)$ holds

$$rms(t) = NORM. \sqrt{(1+\alpha^2 - 2\alpha \, .C_a(t))}$$

If $\alpha=1$, i.e. if predicted and observed height variances are equal this reduces to

$$rms(t) = \sqrt{2.} \; NORM \; .\sqrt{1 - C_a(t)}$$

For $\alpha<<1$, i.e. if the predicted height variance is much too small, as is the case in T21, it follows that

$$rms(t) \simeq NORM$$

and therefore contains no useful information any more. This means that RMS-errors should be interpreted with some care.

Particularly when models are compared with different variance spectra, no useful conclusions can be drawn from a difference in RMS-errors. A lower RMS-error does not necessarily indicate a better performance. This should be keptin mind when comparing N48 and T40 with T21. However, throughout the forecasting period the kinetic energy spectra of N48 and T40 are in good agreement with the observed one and therefore we may compare the RMS scores of these integrations with some confidence.

The two quantities rmsp(t) and NORM represent two types of no-skill forecasts. As soon as the RMS-error of the forecast reaches NORM, there is no skill left in the forecast from the RMS point of view and we might as well have taken the climatological mean. Similarly when the forecast RMS-error reaches the persistence asymptotic level, we might as well have taken the initial values.

Now going to figure 3.2.1, which exhibits the RMS-error of height, averaged over the troposphere and over the N-hemisphere north of 20^{O}N, we note first of all (see top-figure, labelled TOTAL), that all models are considerably better than persistence throughout the forecasting period, but that they all reach NORM by day 6 - 8. In the wavenumber group 1 - 3 this level is reached after 8 - 10 days and in the baroclinic wave group after 4.5 days. The shortest waves show no forecasting skill after 1 - 2 days already and seem to have reached their asymptotic level by day 3. Examination of the asymptotic levels reveals that only the baroclinic waves 4 - 9 behave according to the above given theory. The RMS-errors of height of the longest waves still show an upward trend at the end of the period and have by no means reached the persistence level. In the shortest wave group 10 - 20 the asymptotic level of the RMS-errors is consistently lower than the persistence-level and closer to NORM. This may indicate too little variance in this part of the height spectrum of the models. In the zonal part all asymptotic levels, including that of persistence, are close to NORM. This may indicate that the zonal NORM is not representative for this particular ten-day period. This is supported by the observation that anomaly correlation coefficient of persistence of the zonal part levels off to a constant positive level (fig. 3.2.4).

As can be observed from figure 3.2.1 there is some indication that the N48 integration scores consistently lower RMS-errors than the T40 integration after day 6. A closer examination of the different wave number groups suggests that this is caused mainly by a better performance in the longest waves. The differences are however very small and might well be within the limits of statistical significance. Moreover, as pointed out above, none of the models shows forecasting skill from the RMS point of view after day 6, so it is doubtful whether it is sensible to claim superiority of one model over the others during that period. Taking this into account, the impression is that N48 and T40 show a fully comparable performance. Further evidence for the equivalence of both models is obtained from figures 3.2.2 and 3.2.3 showing time-height and time-latitude plots of the total RMS height error. It is evident that the distribution of RMS errors in both plots is highly identical even in detail.

Now turning to the anomaly correlation coefficient, figure 3.2.4 shows more convincingly than the RMS-errors a better performance of N48 during the second half of the forecasting period. This may be related to the above mentioned faster propagation of waves in the T40 model, because the correlation coefficients are more sensitive to phase-, than to amplitude errors.

We are unable to explain the relatively good performance of T21. The remarks made above concerning the variance differences do not apply here. It may suggest that the amplitude errors of the T21 integration are much more serious than the phase errors. The mutual correlation between the models (figure 3.2.5) and the RMS height differences (figure 3.2.6) shows the high correlation between N48 and T40, thus confirming the equivalence of the performance of both models.

Summarising we may conclude that, although the usefulness of the objective verification scores is doubtful, there is some indication that N48 performs slightly better than T40, particularly for the longest waves. More integrations are required, however, to establish the statistical significance of this difference.

3.3 Energetics

A proper simulation of the energetics of the atmosphere, including the conversion between different forms of energy, is of great importance not only for climate simulations, but most probably also for the problem of medium range weather forecasting.

Before new physical parameterization schemes, adapted to this problem can be developed, a study and understanding of the response of models to conventional schemes is necessary. In this section we will show some of the results obtained in this study. We will present some statistics on kinetic energy (KE) and available potential energy (APE) and the conversion between the zonal and eddy components of these energies. It should be stressed once more (see Arpe et al, 1976) that the energy calculations are based on geostrophic rather than real winds in order to facilitate the comparison with observed data which do not include winds. Finally, we will pay some attention to the heat balance of the atmosphere in the model.

3.3.1 Kinetic energy

Figure 3.3.1 shows the tropospheric KE spectrum and the 500 mb height spectrum, averaged over the last 2½ days of the forecast period. The T40 spectrum is in good agreement with both the NMC and the N48 spectra. The lack of energy in all wavenumbers larger than four in the T21 integration is not found in T40. This is probably due to its higher resolution but might also be influenced by its much smaller horizontal diffusion coefficient.

Figure 3.3.2 shows the time dependence of the KE over the northern hemispheric troposphere. In all models there is a lack of KE in all wave groups, except perhaps in the zonal component. From all plots, however, it can be seen that most of the deficiency is already present in the initial state, apparently due to a difference between the GFDL- and NMC analyses and to the different interpolation steps involved. The KE deficiency in the long waves increases in all integrations. T40 is no exception in any of these features. In the baroclinic wave group T40 follows roughly the same pattern as N48.

During the first four days the initial increase and subsequent decrease of KE is well predicted, although at a lower level. All models have a very low level of baroclinic activity around day 5. Although less pronounced, T40 shows the same strong increase of baroclinic activity as N48. We mentioned this already above in our discussion of the Hovmöller diagrams. Figures 3.3.3 and 3.3.4 show that this increase in both models is concentrated near the average position of the jet stream at about 40^{o}N and 300 mb.
Figures 3.3.5 and 3.3.6 show the height distribution of the kinetic energy as a function of time for two different wave groups. The first figures show clearly the loss of KE in the longest waves. This may well be connected with the vertical resolution in view of the observation that the effect is even stronger in the UCLA model integration with only 6 levels. (Arpe et al,1976).

It should be pointed out, however, that also the horizontal resolution of the UCLA model is lower and rather like N24. The maximum at day 2 in wavenumbers 4 - 9 is well predicted by N48. T40 is less successful here.

In summary T40 shows the same shortcomings in its prediction of KE developments as N48. The seemingly superior prediction by the latter model of some details in the later part of the forecast period may be caused by the unrealistically strong increase of baroclinic activity.

3.3.2 Available potential energy

The tropospheric available potential energy (APE) north of 20^{O}N as a function of time is shown in figure 3.3.7. Most of the comments on the KE apply to this figure as well : a general deficit of APE over the whole forecast period, particularly in the spectral models; a steady decrease of energy in the longest waves and a dramatic increase in the baroclinic waves beyond day 7. The zonal APE shows a steady increase in the N48 run from day 3 till day 7, which may be related to the onset of baroclinic activity at day 7. Inspection of figures 3.3.8 and 3.3.9, which display the vertical distribution of APE as a function of latitude halfway during the forecast period reveals that also T40, due to its vertical resolution, is unable to cope with the sharp vertical gradients near the tropopause. It should be noted that the unrealistic N48 values near the ground in figure 3.3.9 are not found in T40. Gauntlett et al (1977) attributed these spurious maxima to the finite difference formulation of the ω-term in the thermodynamic equation.

3.3.3 Energy conversion

For reasons explained in Arpe et al (1976) the examination of the energy conversions is limited to the transfer of energy between the zonal and eddy components of KE and APE separately. Conversions between APE and KE were not calculated for want of reliable data.

Figures 3.3.10 and 3.3.11 show the tropospheric energy transfer north of 20°N between the zonal and eddy components of KE (CK) and APE (CA) respectively. Positive numbers indicate a positive energy flow from zonal to eddy energy. T40 follows the other models in predicting the trend quite well for the first few days and then declining to a level lower than NMC. In general the observed transfers show a much larger variability than the model transfers,but we should point out that the high NMC variability is not necessarily realistic. Indeed a comparison of analyses from different sources (Arpe,K., private communication) reveals that the energy transfer variability may show considerable differences.

Particularly in the long waves none of the models can describe the large positive kinetic energy flow after day 3. Moreover all models underestimate by a factor of two the positive transfer of APE. Figure 3.3.12 shows that the long wave KE conversion is strongly concentrated near the jet stream. Although the T40 prediction is "best", it underestimates the maximum by a factor of six ! The mid-tropospheric APE long wave energy conversion (figure 3.3.13) is predicted not only with the wrong intensity but also at the wrong place.

The conclusion must be that none of the models, including T40 can cope with the energy transfers during the forecasting period.

Let us now concentrate on the energy input into the atmosphere by physical processes. Figures 3.3.14 and 3.3.15 show the global energy input into the atmosphere due to rainfall (latent heat release), and the sensible heat flux from the ground.

The most prominent feature, which dominates the whole energy balance, is the large latent heat release due to rainfall around day 3 and its subsequent relaxation, which is still continuing at the end of the period. The peak value is in the order of 50 % higher than the climatological mean. During the first two days there is a net increase of the water content of the atmosphere of about 5 %, because the evaporation from the ground is much larger than the precipitation (see figure 3.3.16).

The most likely explanation is that the initial divergence field, and therefore the initial vertical velocities, are unrealistic. This is strongly suggested by comparison of the 1000 mb analysis (figure 3.1.1) and the initial divergence at the lowest sigma-level (figure 3.3.18). The situation may possibly be aggravated by an inaccurate humidity analysis, such that initially the humidity is not at the right places to be precipitated by the synoptic systems. It takes several days before equilibrium is restored. In fact, although precipitation is still larger than evaporation by the end of the 10-day period, they are approximately in balance when averaged over the whole period as can be seen in figure 3.3.16.

Another intriguing feature is found in figure 3.3.15. Both spectral models show a negative sensible heat flux throughout the forecast period, in contrast to the grid point models and to climatology. This may be related to the observation that the globally averaged radiational cooling is less in the spectral models than in the grid-point models. We have, however, not been able to explain this.

The global atmospheric heat balance due to the different physical processes is shown in figure 3.3.17. Clearly the lack of balance during the first half of the period is caused by the spurious peak in the latent heat release. The balance seems to relax and level off to a constant positive value at the end of the period which may be due to the fact that dissipative processes are not taken into account.

The question how the models deal with the initial deficit and subsequent excess input of energy into the atmosphere cannot easily be answered without further detailed analyses. Figure 3.3.19 shows the global potential plus internal and total energy in the T40 integration as a function of time. The effect of the imbalance is clearly seen and equilibrium seems to be restored only after 4.5 days. Because the effect of the spurious behaviour of the latent heat release will presumably mainly affect the tropical zone, it is likely to affect the available potential energy as well, and the zonal part of it in particular. This is probably also the reason why it cannot be observed in figure 3.3.7 which does not include the tropical zone. Without further studies it is impossible to assess the effect of the presumably substantial variation of available potential energy, but it might be the reason for the initial decrease and subsequent increase of baroclinic activity in the model.

3.4 Precipitation

The low resolution T21 spectral integration (Hansen and Baede, 1977) revealed some peculiarities in its prediction of precipitation. Firstly, the shape of the precipitation patterns looked rather unrealistic compared with these produced by the grid-point models. It did not produce the familiar oblong or band shaped patterns of the grid-point models but rather circular patterns. Furthermore, the T21 integration produced a persistent spurious area of snow and rainfall over S.E. Asia. Also the response of the T21 model to the presumably poor initial vertical velocities was rather different from the response of the grid-point models.

All these features are apparently caused by the low horizontal resolution of the T21 model because the T40 integration shows none of them. Figures 3.4.1 - 3.4.3 display the predicted rainfall patterns at day 1, 5 and 10. The difference in shape between T21 and the other models is obvious. Less obvious from these plots is the disappearance of the persistent precipitation pattern over S.E. Asia but this was confirmed by a closer inspection of all results including snow fall. The response of the models to the initial humidity analysis was already discussed above.

Concluding, we may say that T40 has the same rainfall prediction characteristics as the grid-point models. No verification of the forecasts was attempted for want of reliable data.

4. Conclusions

The purpose of the integration described in this report was to assess the capabilities of high resolution spectral models to compete with grid-point models in extended range weather forecasting. To this end a spectral model was combined with the same physical parameterization schemes as those used in previous grid-point and low resolution spectral model studies; (Arpe et al, 1976; Gauntlett et al, 1977; Hansen and Baede, 1977), and integrated with a triangular M = 40 horizontal truncation, using a semi-implicit time stepping scheme. The initial data set was for 1st March 1965 00Z. The results of this integration have been compared in this report with the results of the previous grid-point and low resolution spectral integrations. The main emphasis, however, is put on a comparison with the N48 GFDL model integration.

A synoptic comparison shows that there is little to choose between the N48 and the T40 integration. As with all other models, the spectral model gives a good description of the phase change of the longest waves. The prediction of the synoptic systems shows striking failures, particularly too high phase speeds during the first half of the period over the Atlantic and European regions and over the Western Pacific.

The objective verification on the basis of RMS errors and anomaly correlation coefficients suggests a slightly better performance of N48, although the statistical significance was not established. Moreover, because RMS-errors are very susceptible to differences in variance and therefore to differences in the horizontal diffusion, care should be taken before drawing conclusions from these findings in view of the fact that all models had different horizontal diffusion schemes.

Energy transfers are as badly predicted by the spectral model as by any of the other models. The variability of these conversions seems much too low.

Particularly the large abnormal energy transfer from zonal to eddy kinetic energy half way through the forecast period is missed completely.

The heat budget of the atmosphere is unbalanced during most of the forecast period, probably due to a poor initial divergence field. The response to this of the T40 integration is similar to that of the grid-point models, unlike the low resolution T21 model. An intriguing but unexplained feature is the negative sensible heat flux in the spectral models in contrast to a positive flux in the grid-point models.

The general conclusion of this study is that spectral models with sufficiently high horizontal resolution are certainly not inferior to well tested grid-point models in their extended range weather forecasting capability. Their competitiveness with respect to efficiency was shown already in previous studies.

Acknowledgements

The authors express gratitude to the Geophysical Fluid Dynamics Laboratory/NOAA, Princeton, U.S.A. for supplying the initial data for this study and to Drs. B.J.Hoskins and A.J. Simmons of the U.K. Universities Atmospheric Modelling Group, University of Reading, for making their spectral model available.
We would also like to thank Drs.K.Arpe, D.Burridge and B.Machenhauer for their helpful comments.

Annex

Preliminary Comparison with ECMWF's Grid-Point Model (D48)

After completion of this report, preliminary results became available of a 10-day integration of ECMWF's grid-point model with GFDL physics and horizontal resolution corresponding to N48. This integration is referred to as D48. In this annex we present a brief preliminary comparison of T40 and D48.

A visual inspection of the 1000 mb and 500 mb maps reveals that T40 and D48 are much closer than T40 and N48. As an example, figure A1 shows 500 mb forecasts from D48 at day 5 and day 9, to be compared with figures 3.1.6 and 3.1.10. This is substantiated by the objective verification scores. Figures A2 and A3 for example show the mutual correlations of height and RMS height differences between NMC, N48, T40 and D48. Clearly in all wave groups, except the shortest, T40 and D48 are closest. Figures A4 and A5 show the correlations of height and RMS errors. Again both integrations are close, with the RMS height error suggesting a slight advantage for T40 at the end of the period. This is, however, not confirmed by the correlation of height.

In this context it should be stressed once more that the T40 integration used a semi-implicit timestep of 20 minutes, whereas the D48 integration proceeded explicitly with a time step of 2½ minutes.

Without further research it will be difficult to establish the cause of the close similarity of both integrations. Although the spectral model is not strictly energy and enstrophy conserving both quantities are conserved to a high degree. It may be that these conservation properties together with a fairly high horizontal resolution can explain the similarity. Whatever the reason is, these results suggest that under certain conditions a convergence of numerical solutions of widely different schemes may be achieved in spite of differences in the time stepping scheme, the horizontal diffusion or the integration of the hydrostatic equation. This conclusion, however, is based on one case and further research will certainly be required.

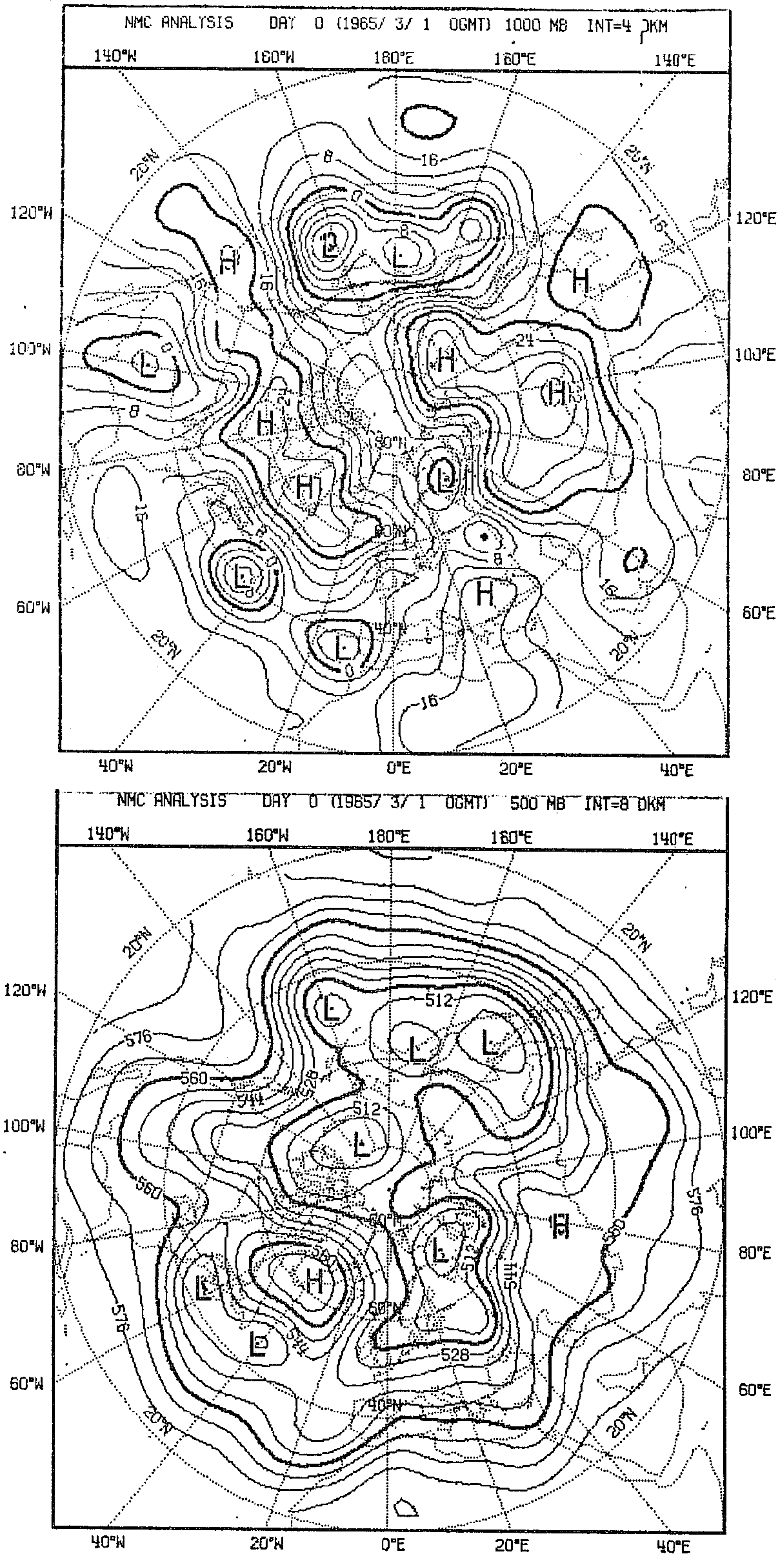

Fig. 3.1.1 Day 0 observed maps of 500 mb (top) and 1000 mb (bottom) geopotential height.

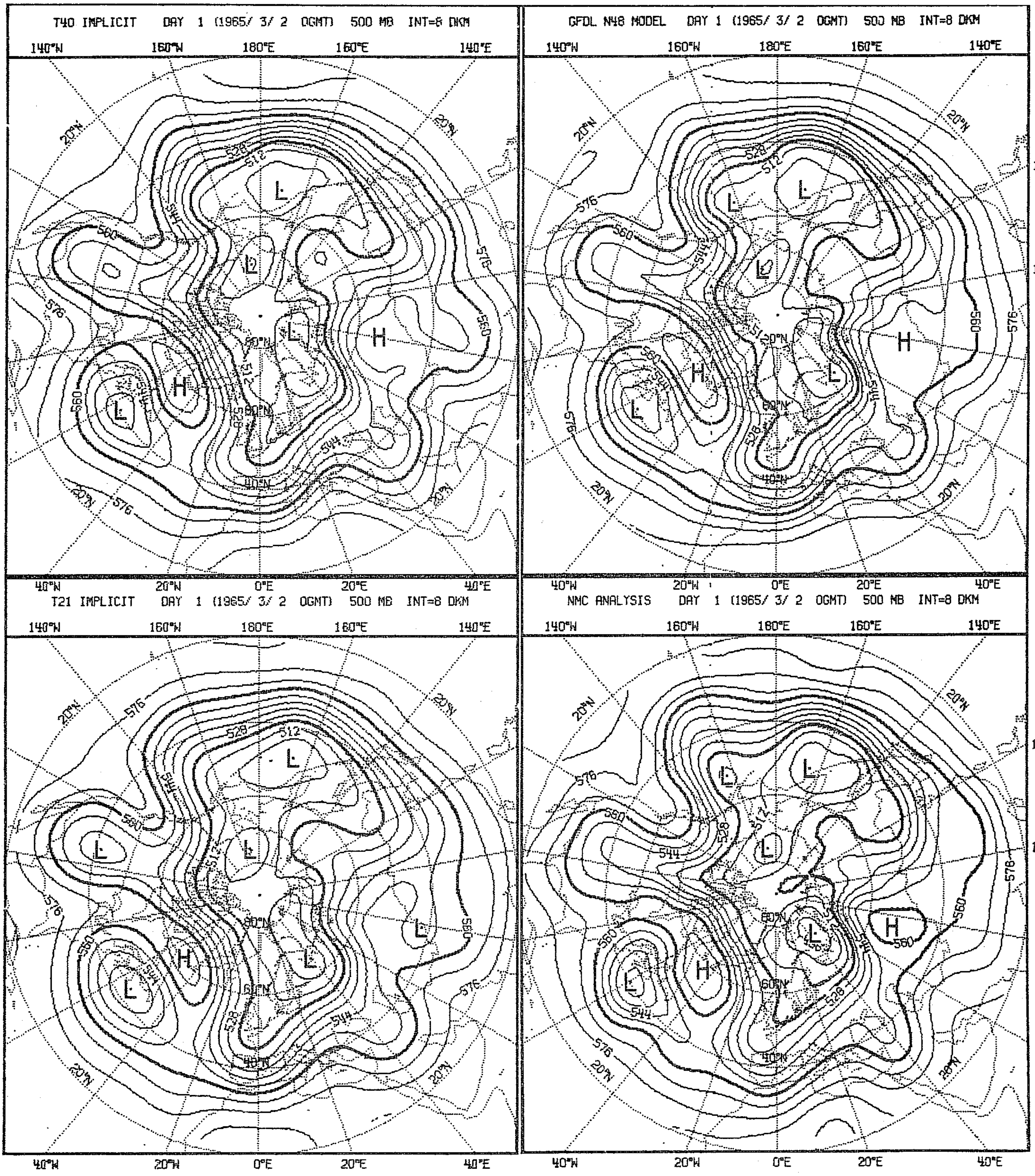

Fig. 3.1.2 Observed (bottom right) and predicted fields of 500 mb geopotential height, day 1.

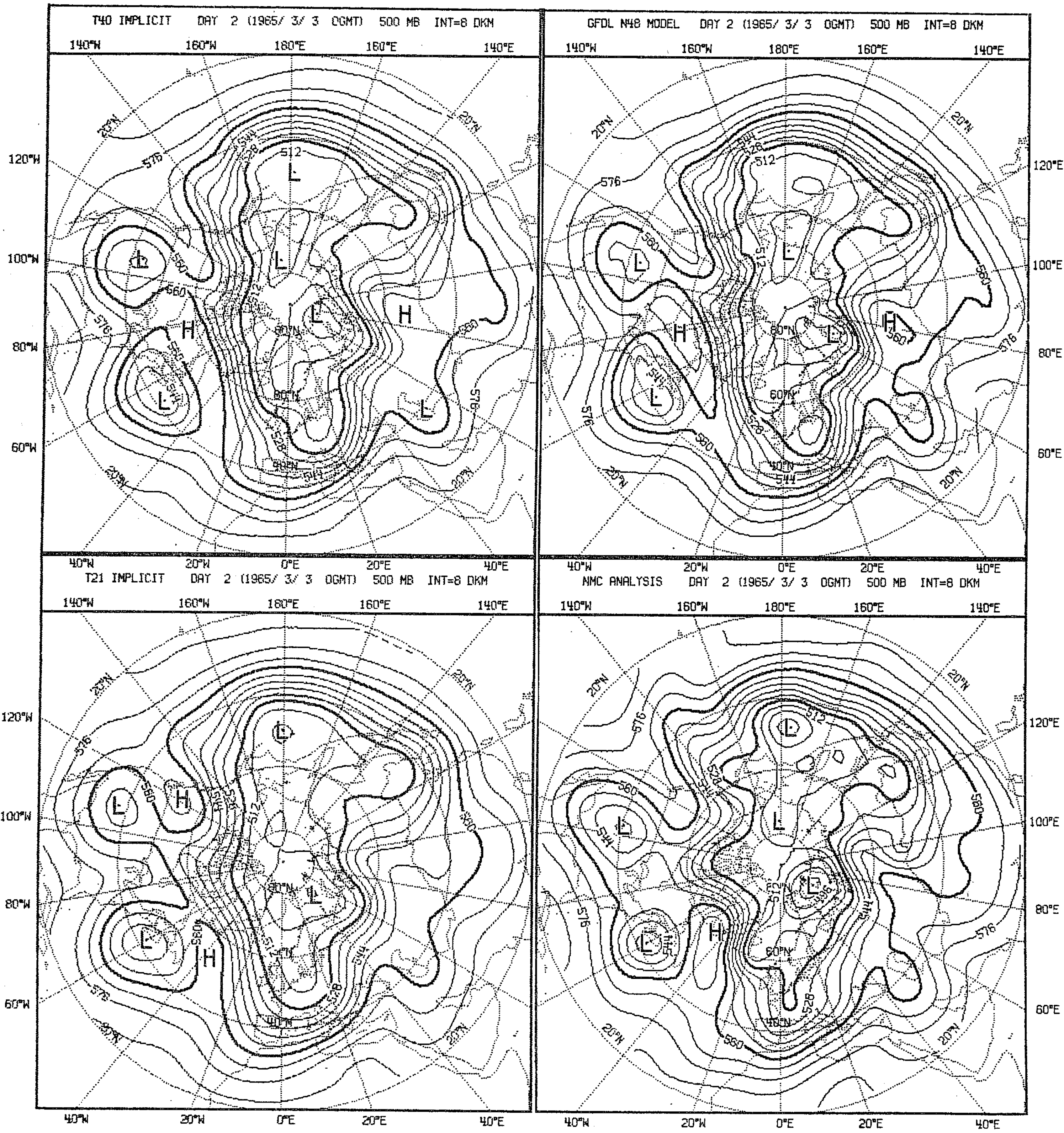

Fig. 3.1.3 Observed (bottom right) and predicted fields of 500 mb geopotential height, day 2.

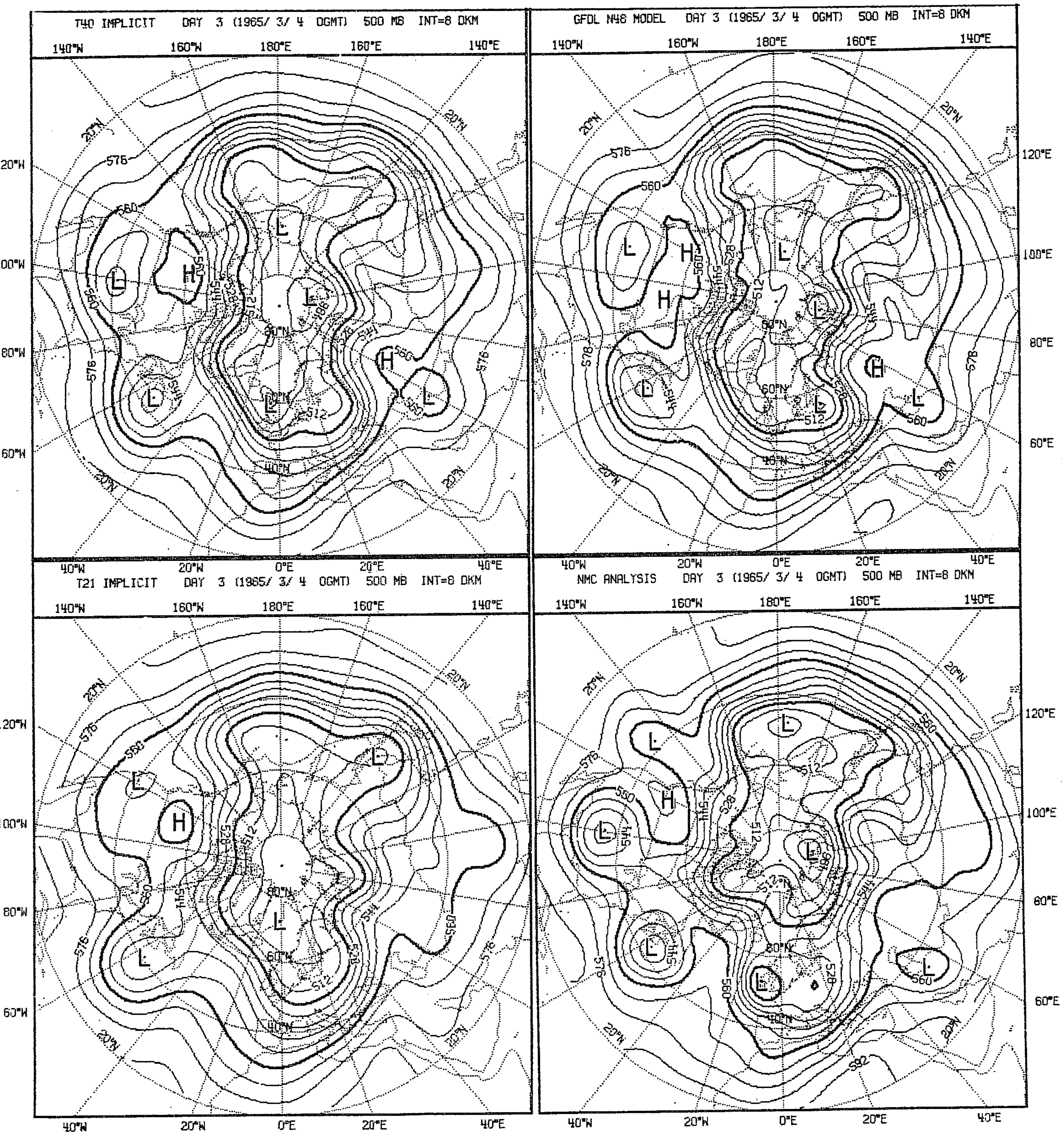

Fig. 3.1.4 Observed (bottom right) and predicted fields of 500 mb geopotential height, day 3.

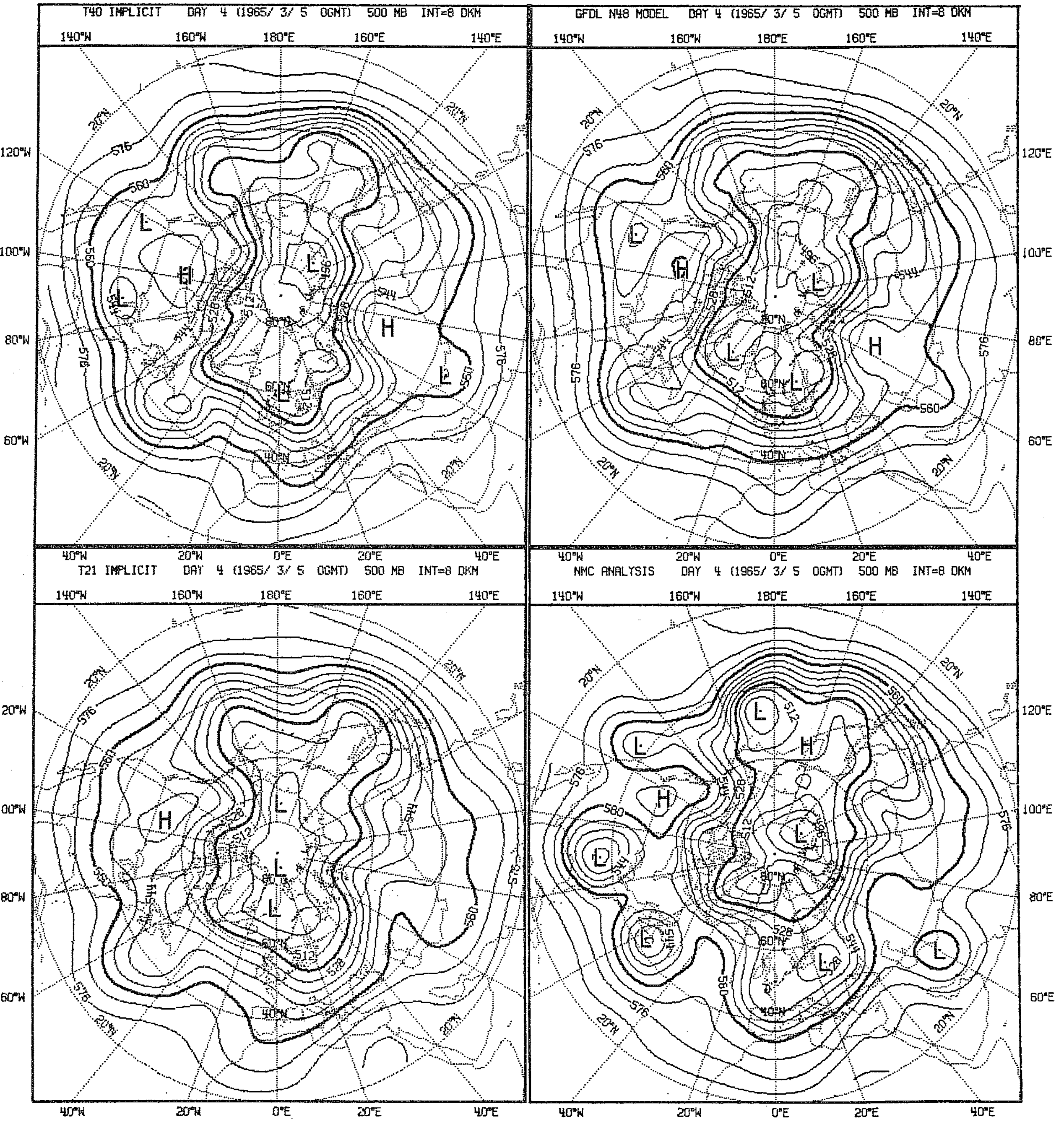

Fig. 3.1.5 Observed (bottom right) and predicted fields of 500 mb geopotential height, day 4.

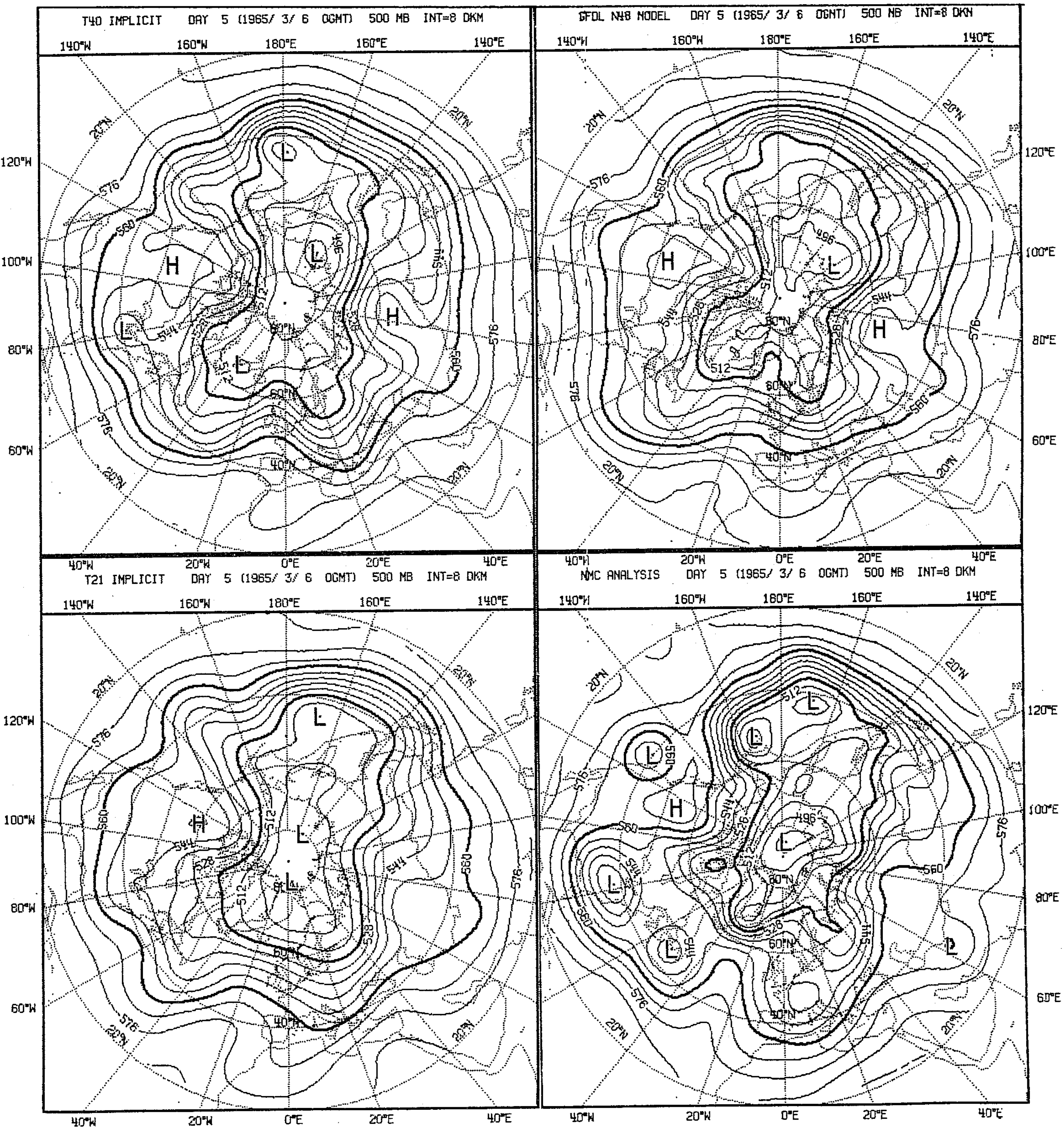

Fig. 3.1.6 Observed (bottom right) and predicted fields of 500 mb geopotential height, day 5.

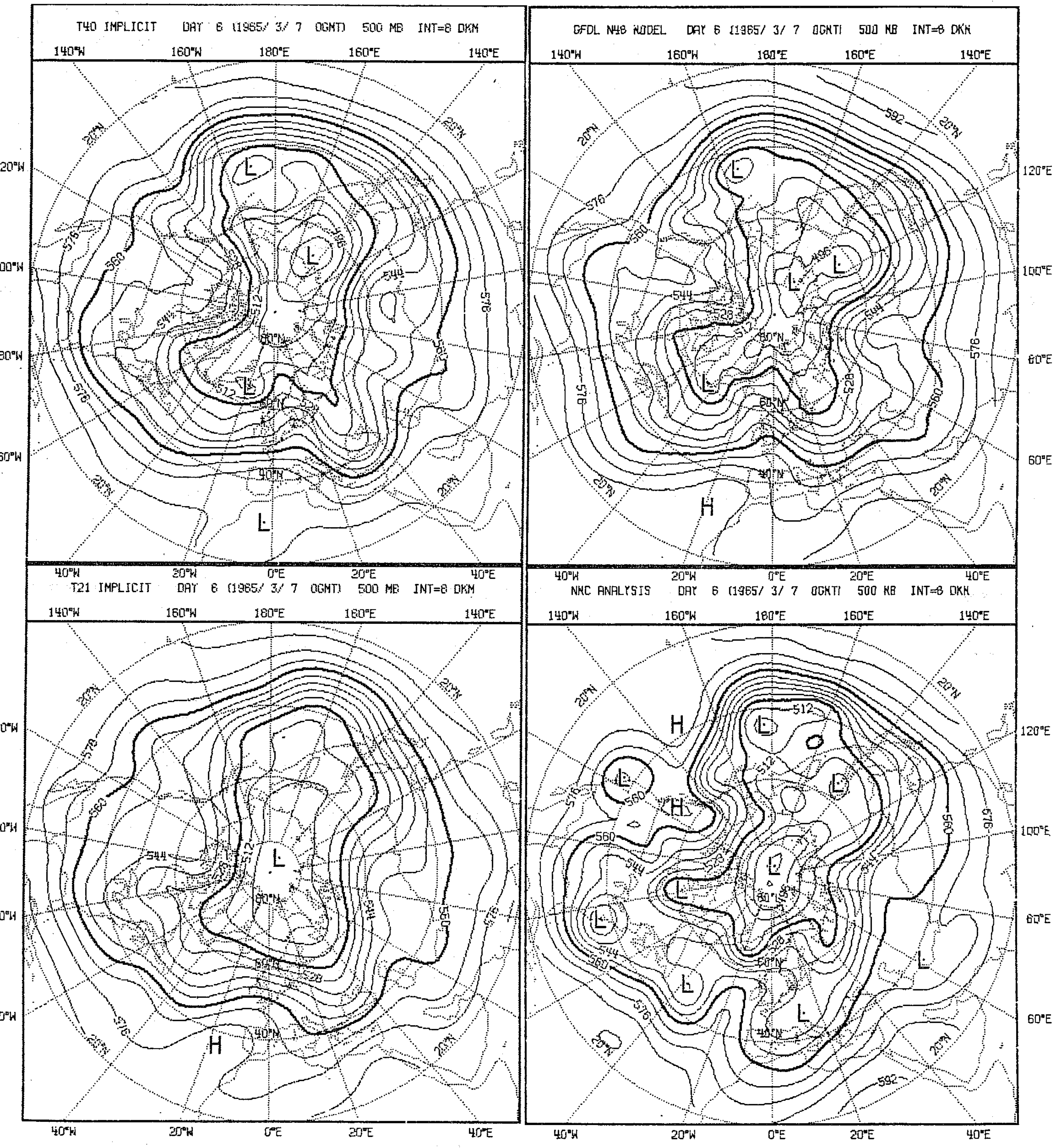

Fig. 3.1.7 Observed (bottom right) and predicted fields of 500 mb geopotential height, day 6.

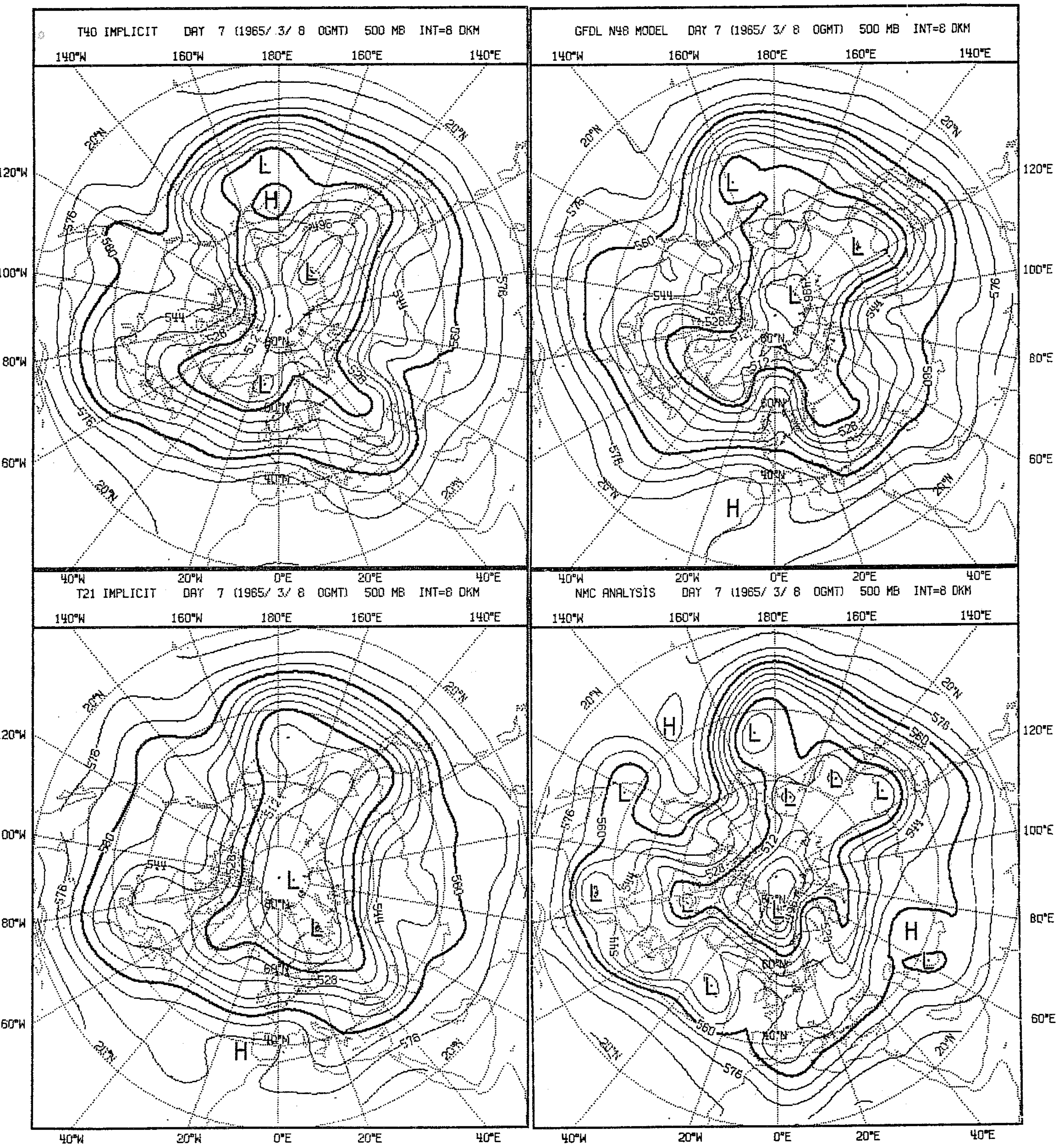

Fig. 3.1.8 Observed (bottom right) and predicted fields of 500 mb geopotential height, day 7.

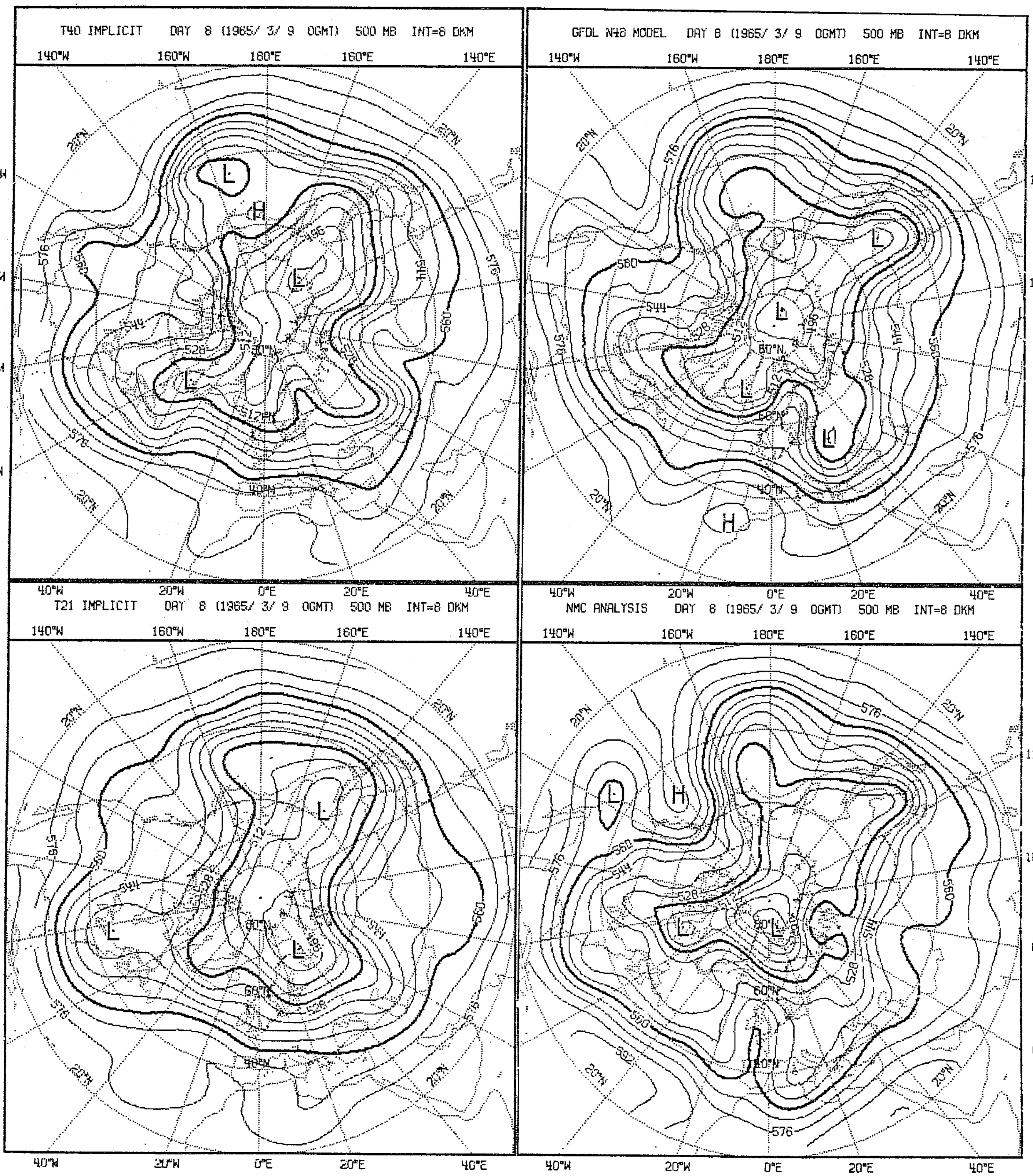

Fig. 3.1.9 Observed (bottom right) and predicted fields of 500 mb geopotential height, day 8.

LIBRARY

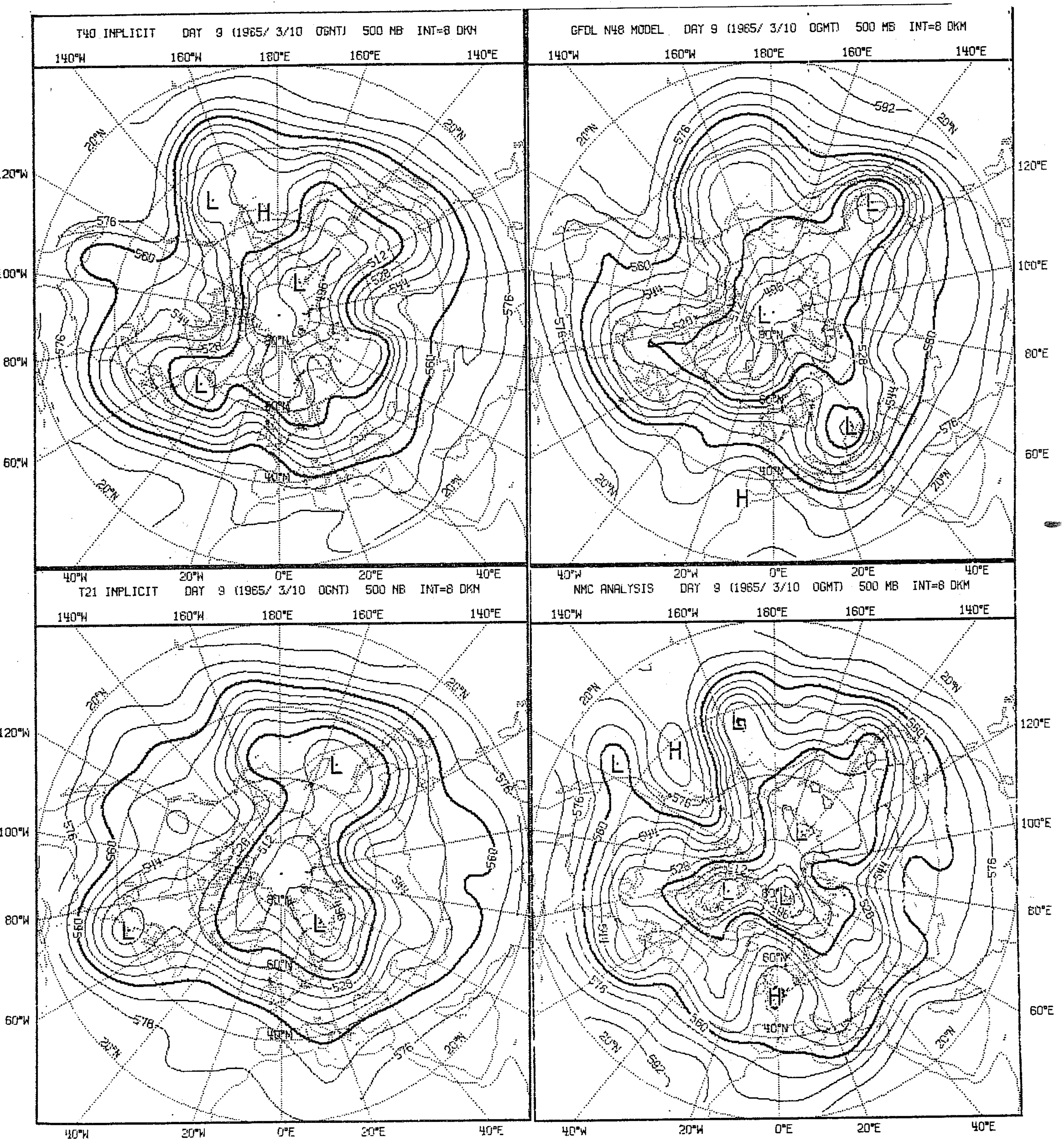

Fig. 3.1.10 Observed (bottom right) and predicted fields of 500 mb geopotential height, day 9.

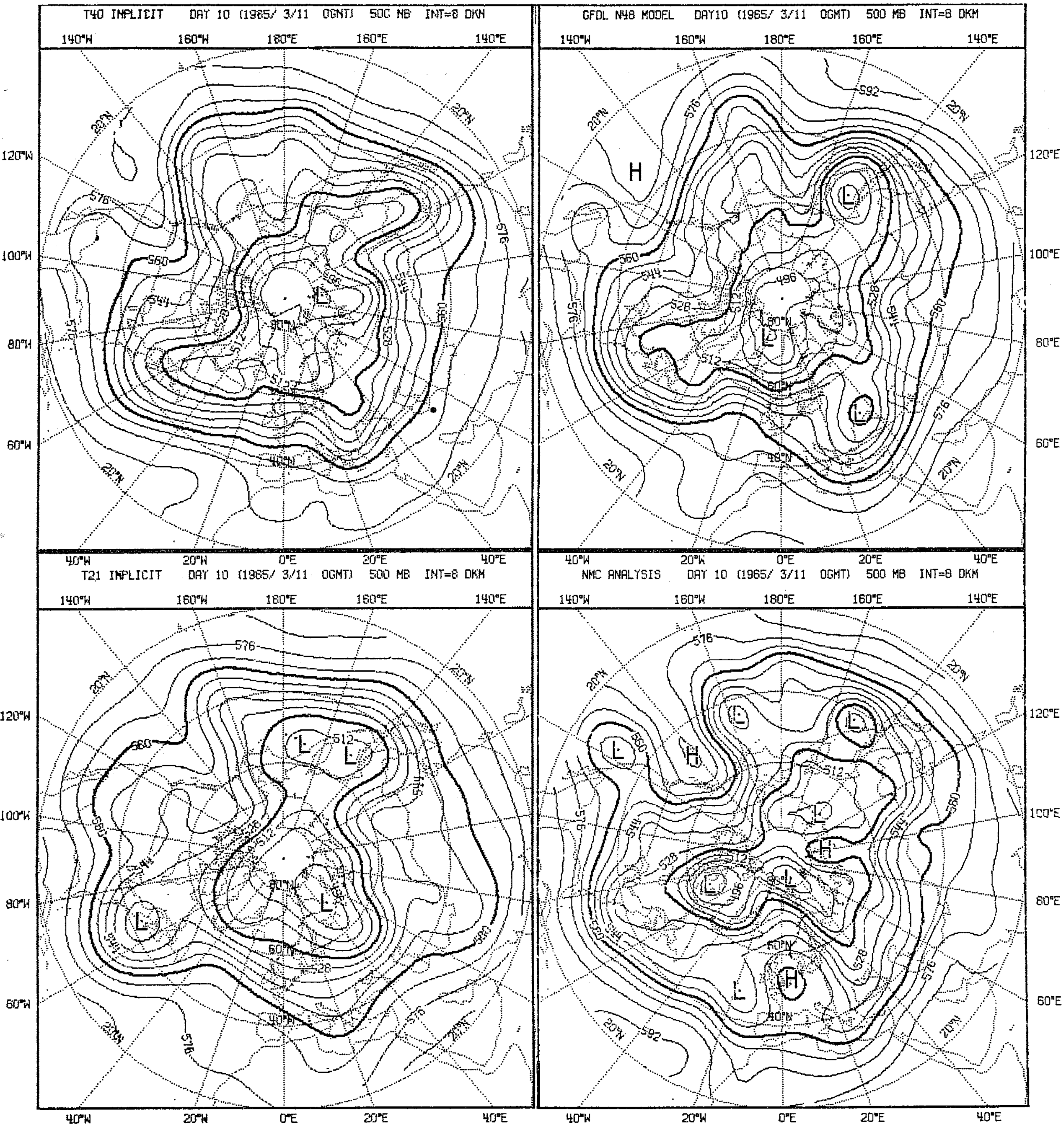

Fig. 3.1.11 Observed (bottom right) and predicted fields of 500 mb geopotential height, day 10.

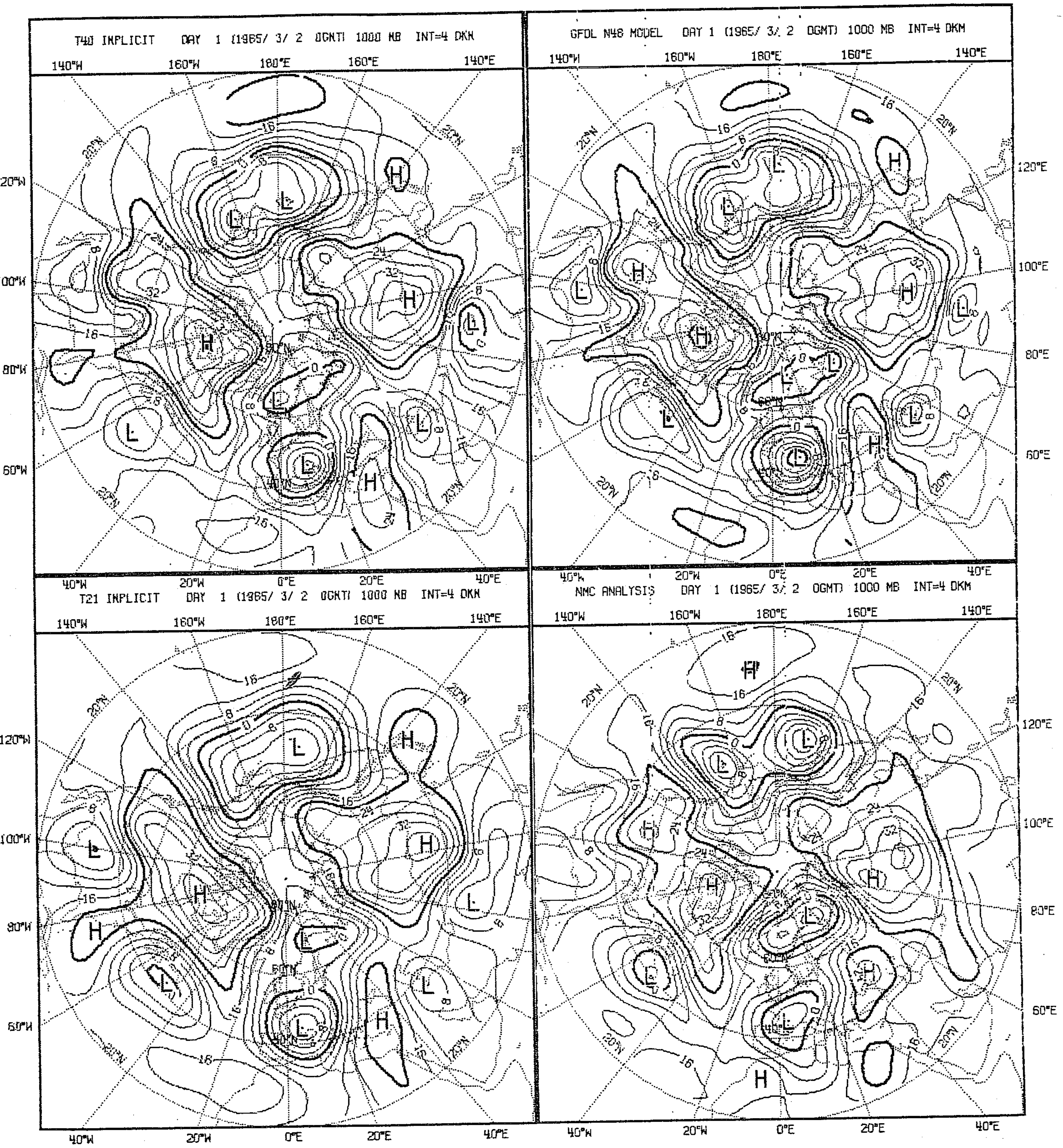

Fig. 3.1.12 Observed (bottom right) and predicted fields of 1000 mb geopotential height, day 1.

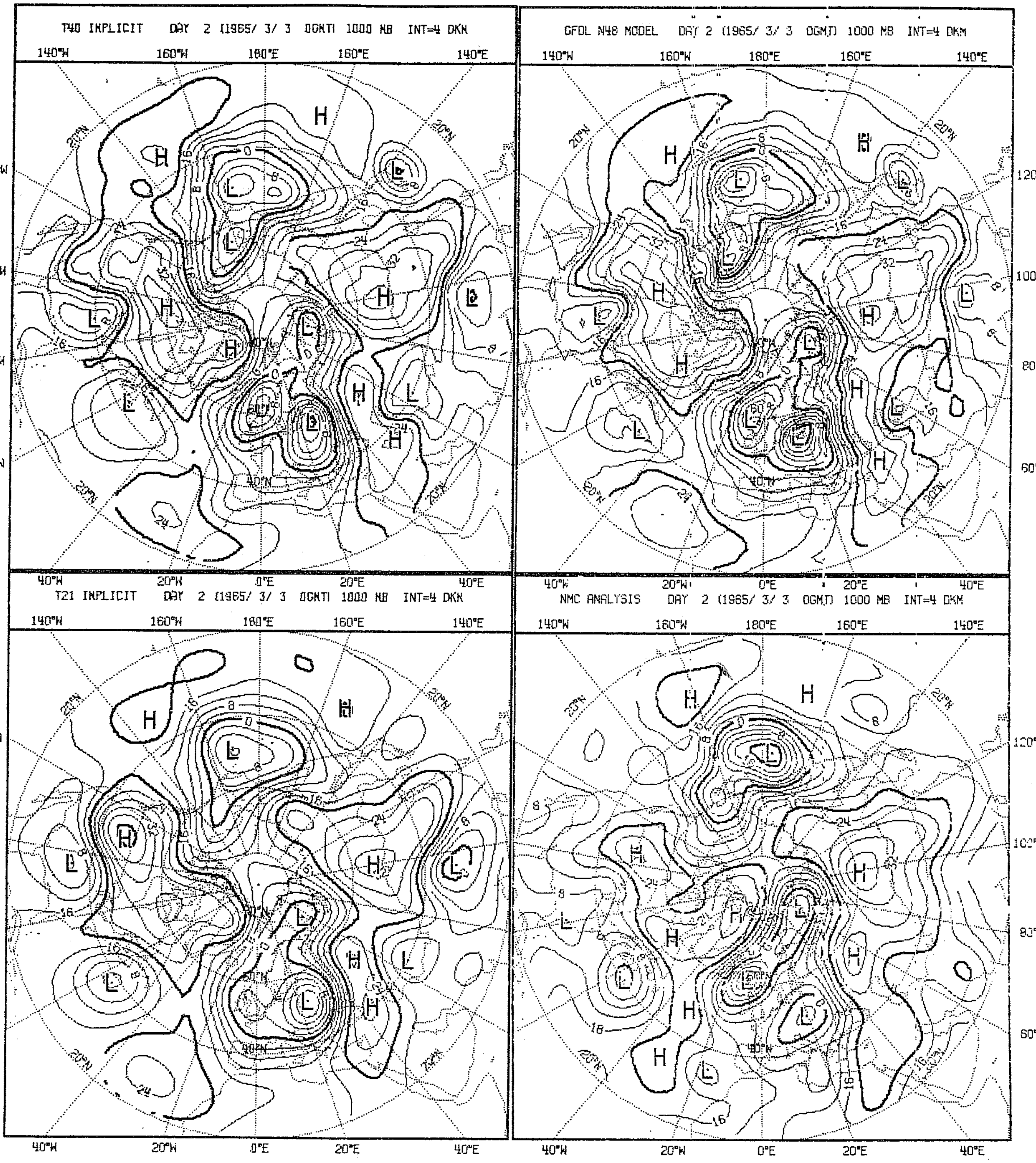

Fig. 3.1.13 Observed (bottom right) and predicted fields of 1000 mb geopotential height, day 2.

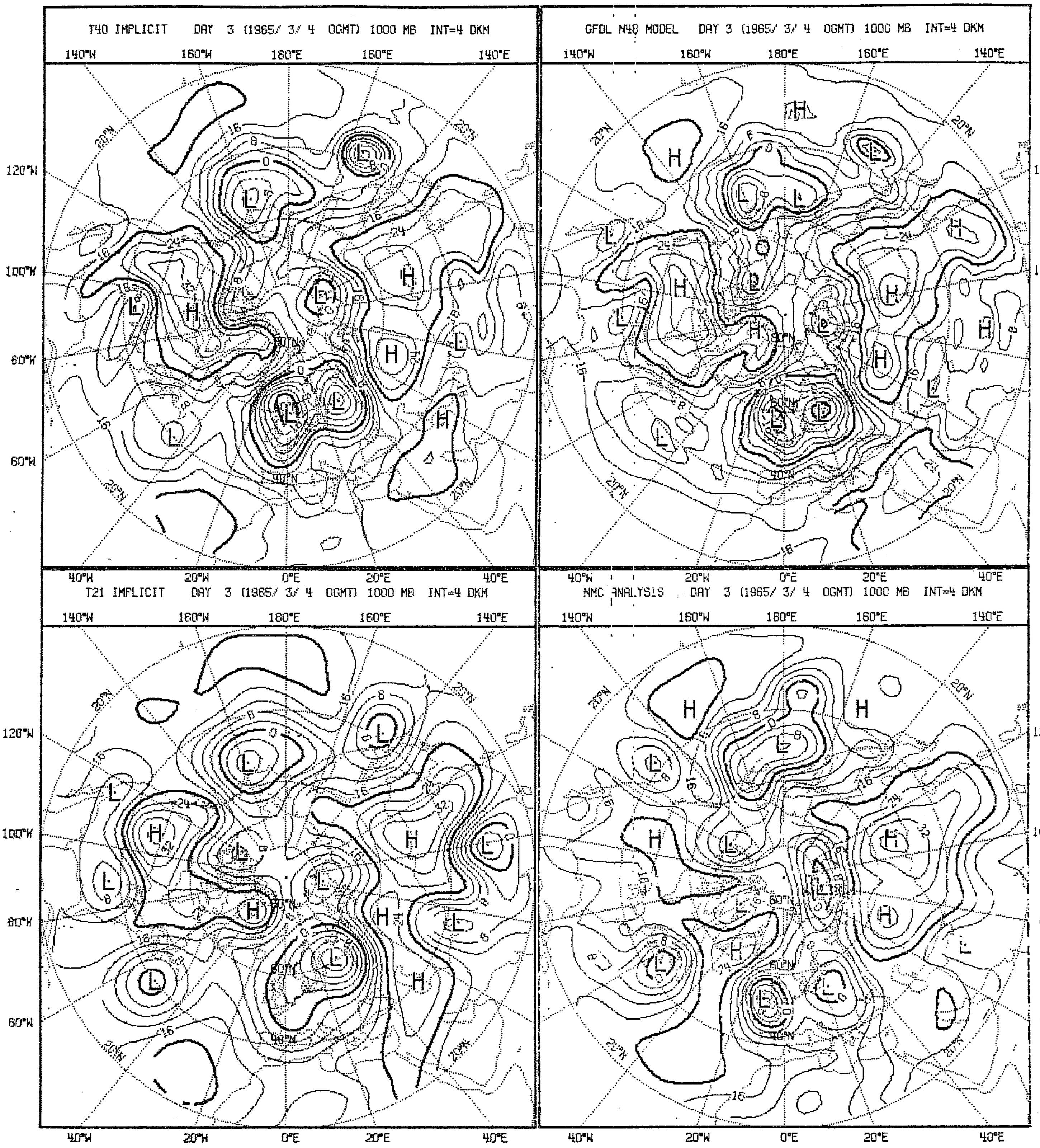

Fig. 3.1.14 Observed (bottom right) and predicted fields of 1000 mb geopotential height, day 3.

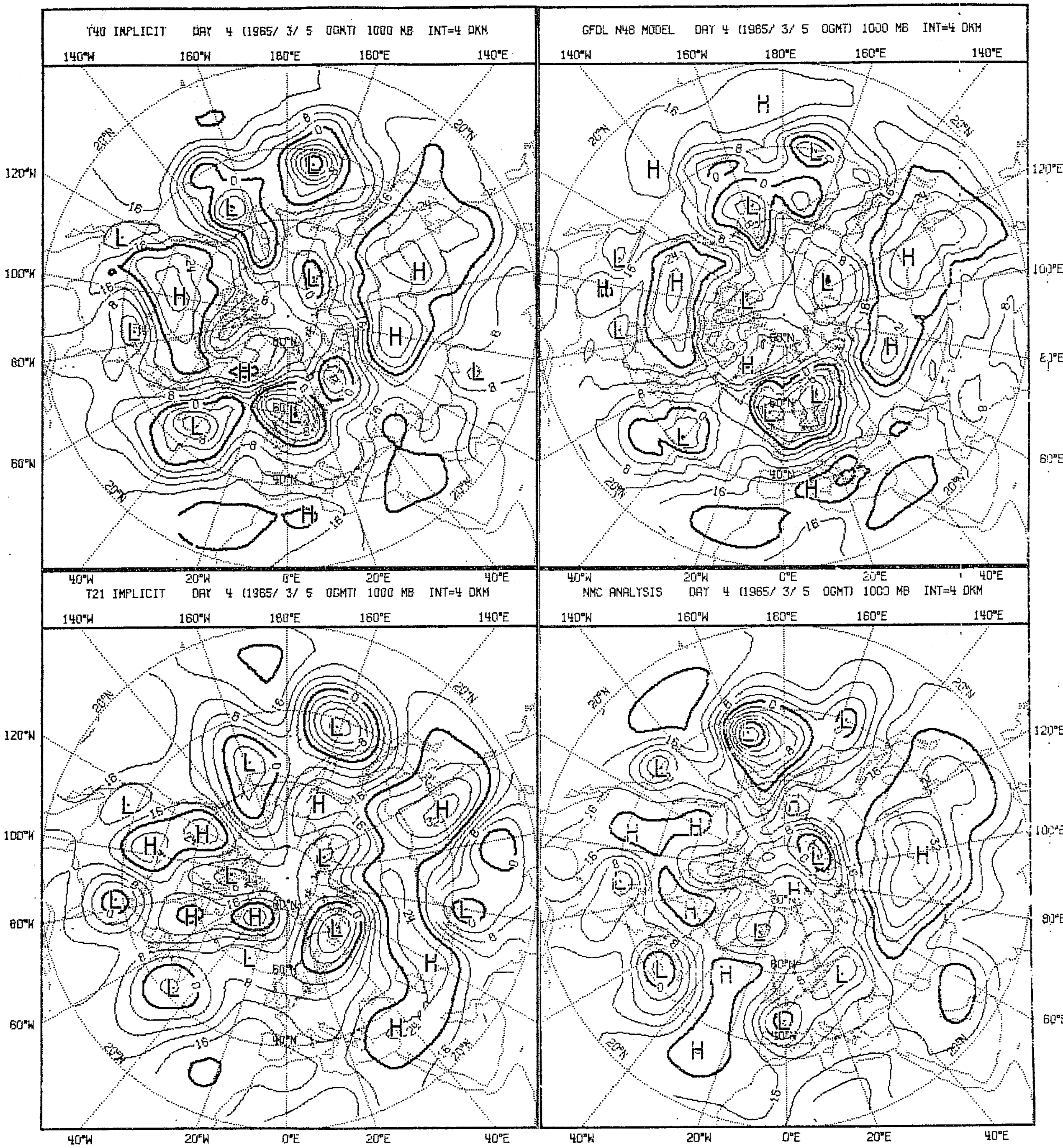

Fig. 3.1.15 Observed (bottom right) and predicted fields of 1000 mb geopotential height, day 4.

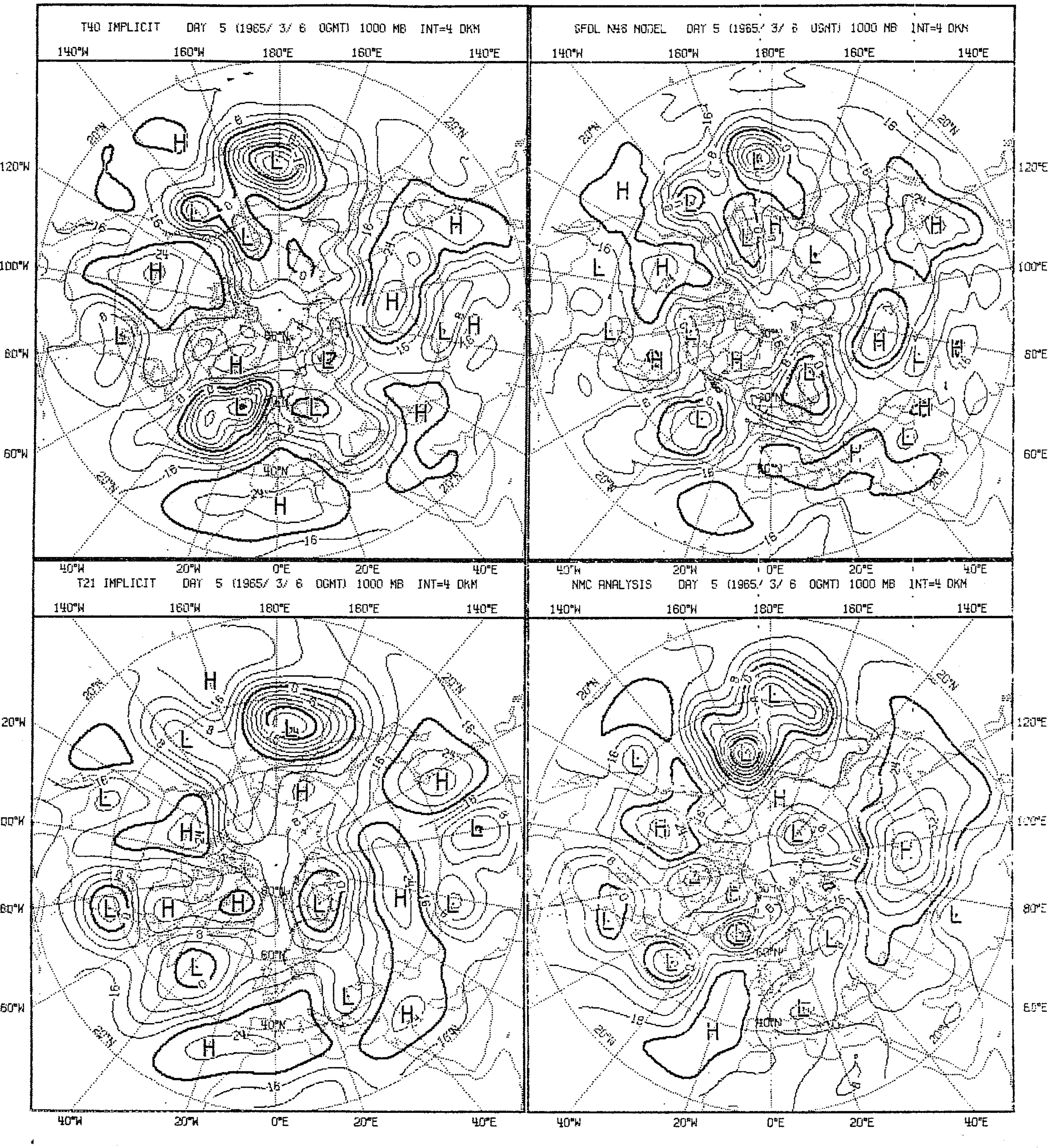

Fig. 3.1.16 Observed (bottom right) and predicted fields of 1000 mb geopotential height, day 5.

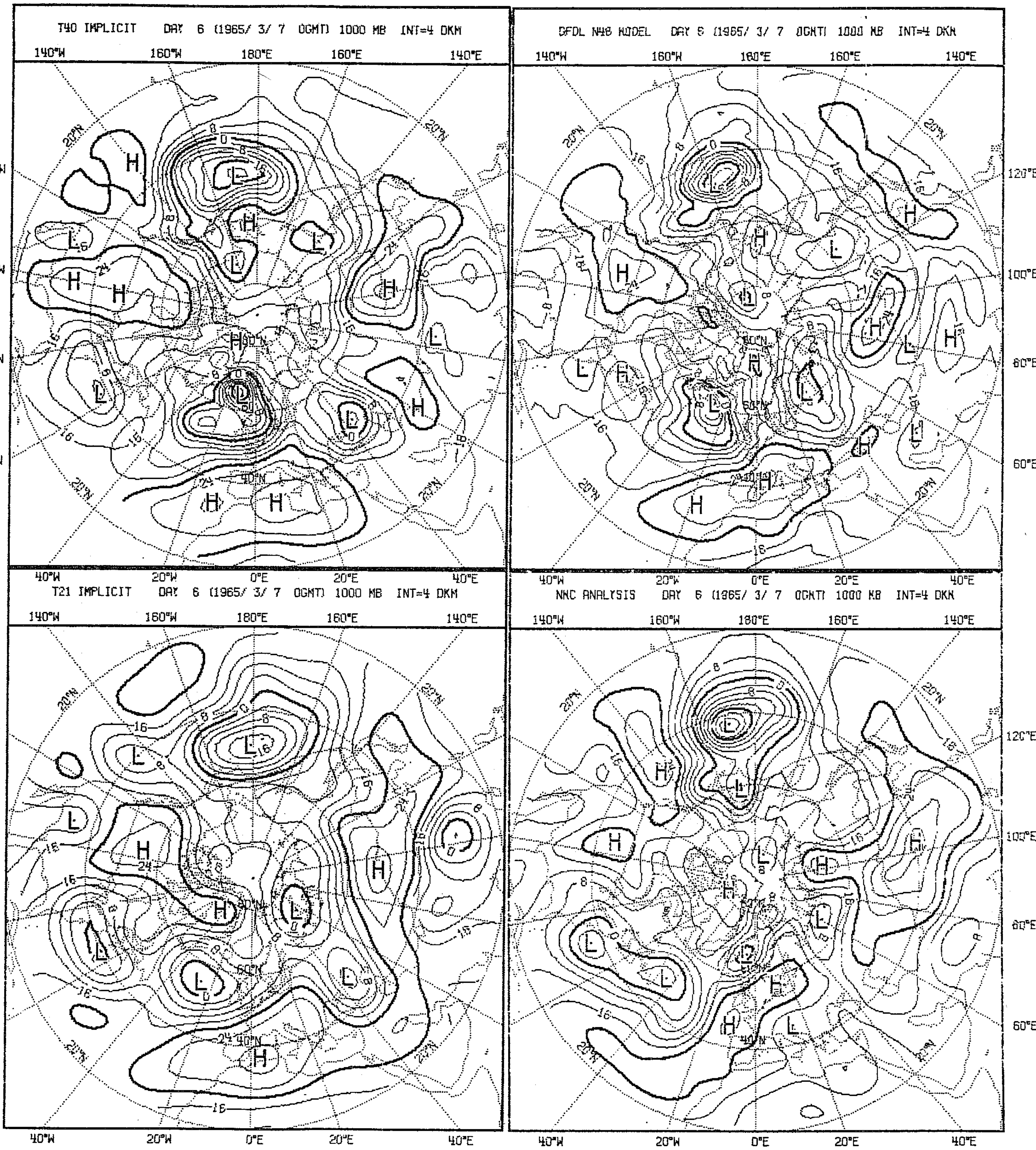

T40 IMPLICIT DAY 6 (1965/ 3/ 7 0GMT) 1000 MB INT=4 DKM

GFDL N48 MODEL DAY 6 (1965/ 3/ 7 0GMT) 1000 MB INT=4 DKM

T21 IMPLICIT DAY 6 (1965/ 3/ 7 0GMT) 1000 MB INT=4 DKM

NMC ANALYSIS DAY 6 (1965/ 3/ 7 0GMT) 1000 MB INT=4 DKM

Fig. 3.1.17 Observed (bottom right) and predicted fields of 1000 mb geopotential height, day 6.

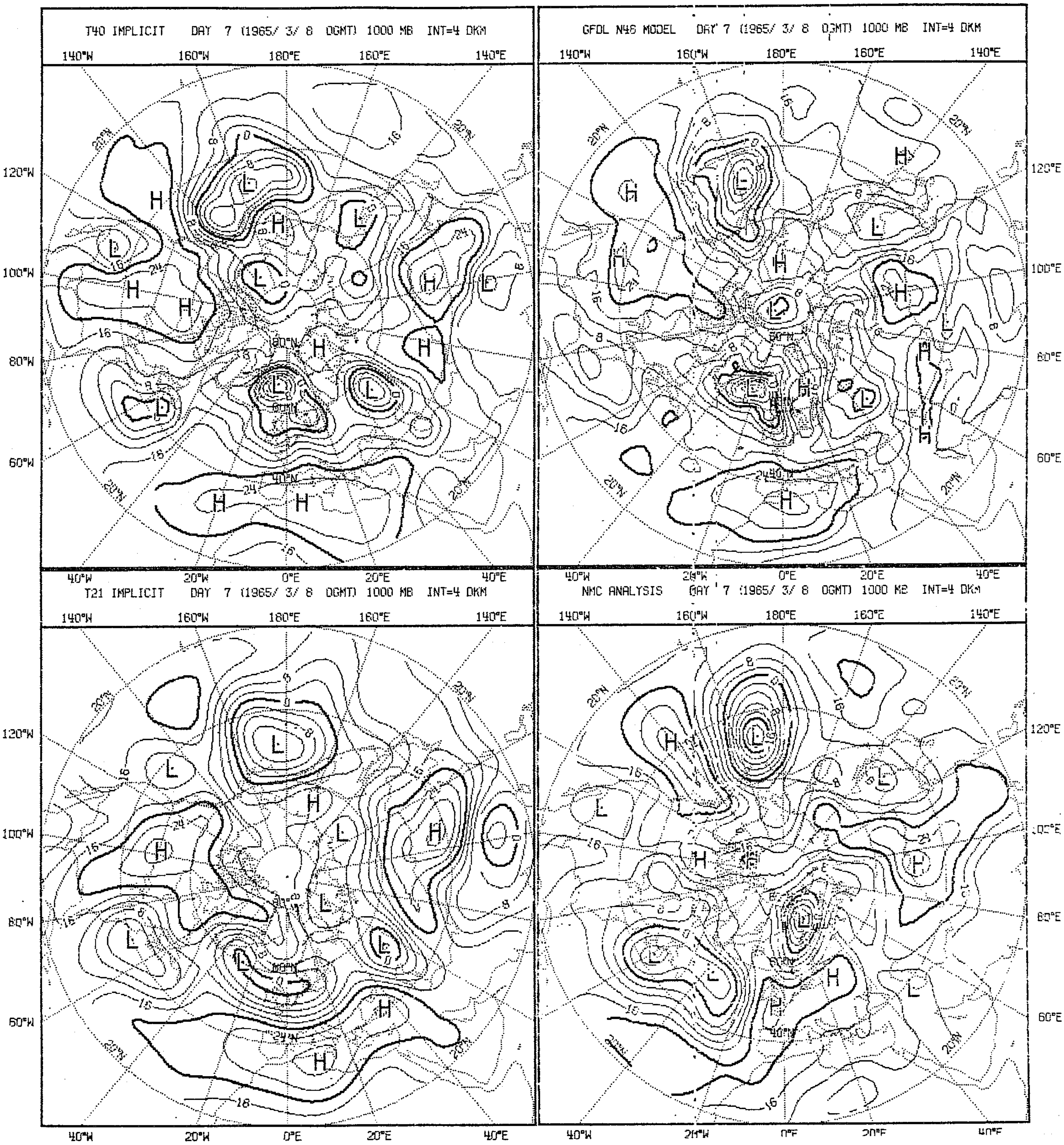

Fig. 3.1.18 Observed (bottom right) and predicted fields of 1000 mb geopotential height, day 7.

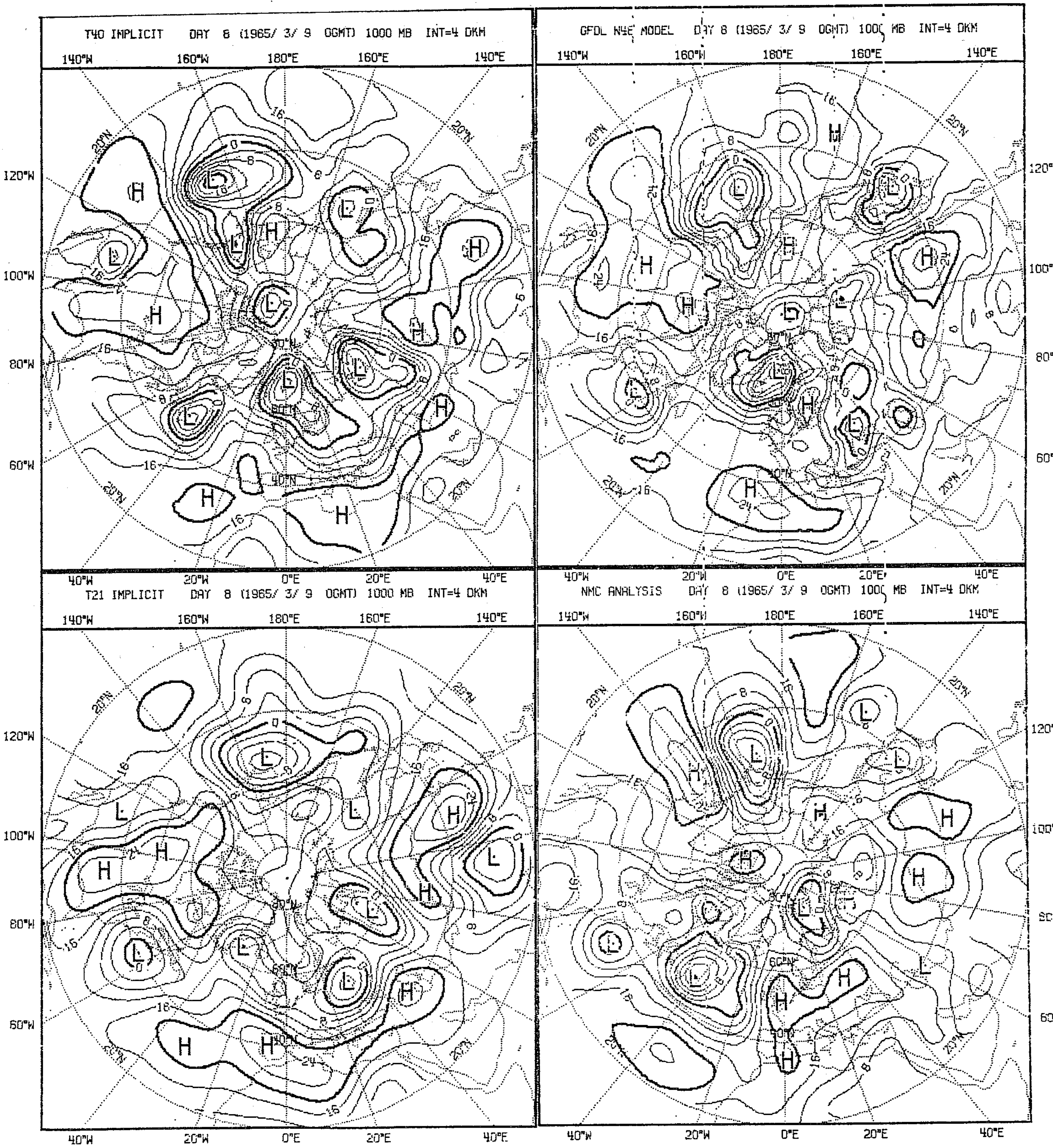

Fig. 3.1.19 Observed (bottom right) and predicted fields of 1000 mb geopotential height, day 8.

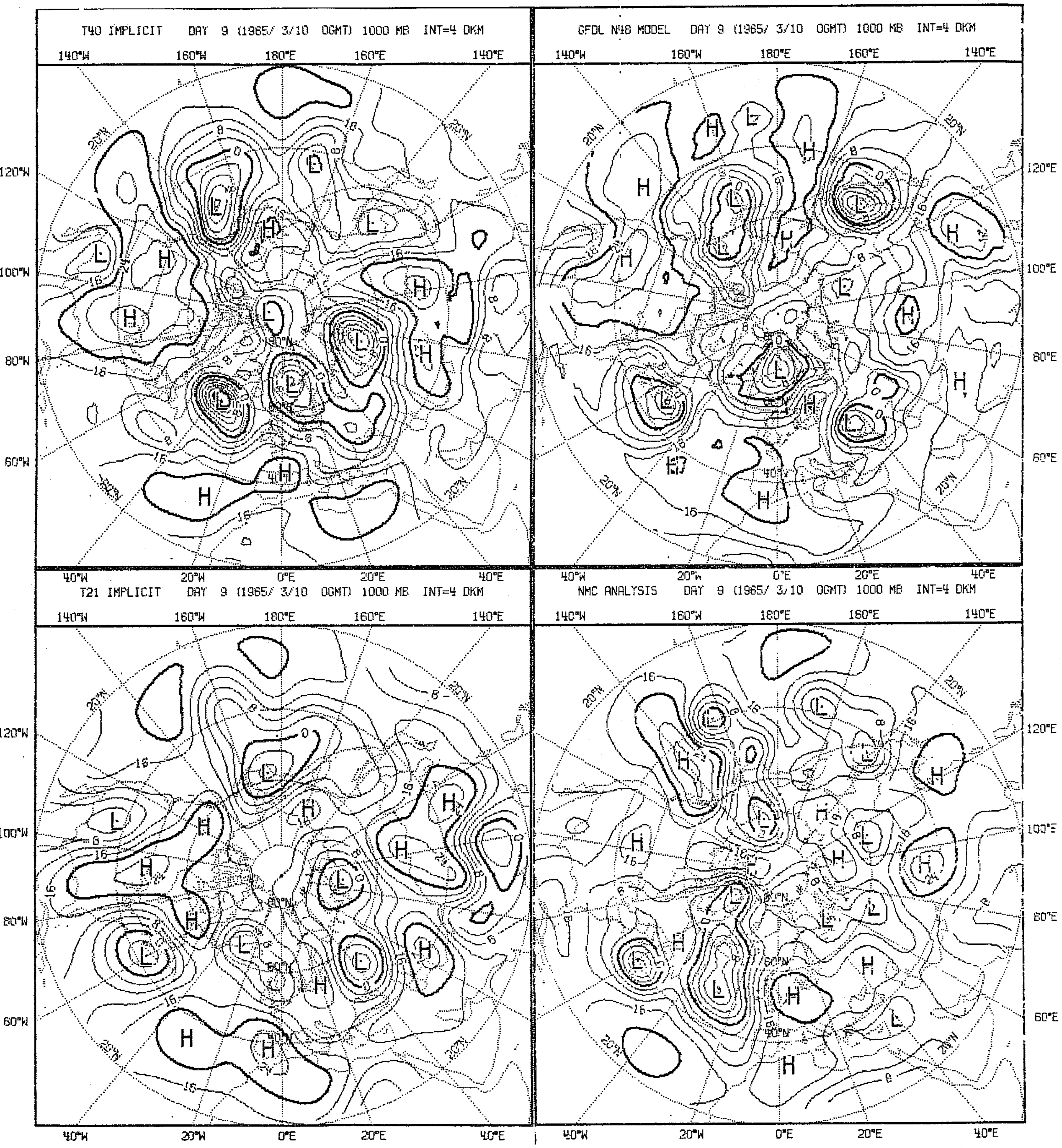

Fig. 3.1.20 Observed (bottom right) and predicted fields of 1000 mb geopotential height, day 9.

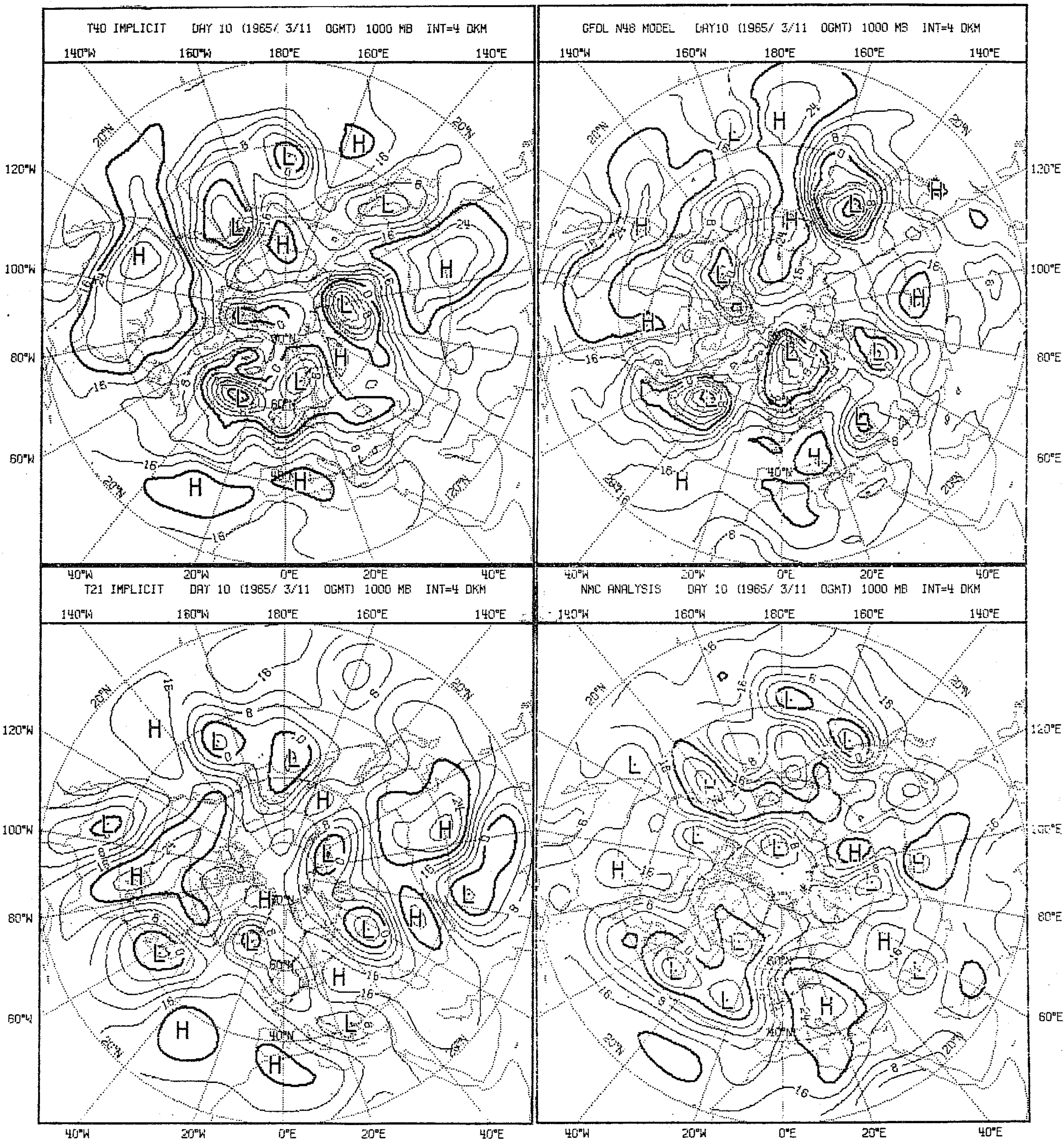

Fig. 3.1.21 Observed (bottom right) and predicted fields of 1000 mb geopotential height, day 10.

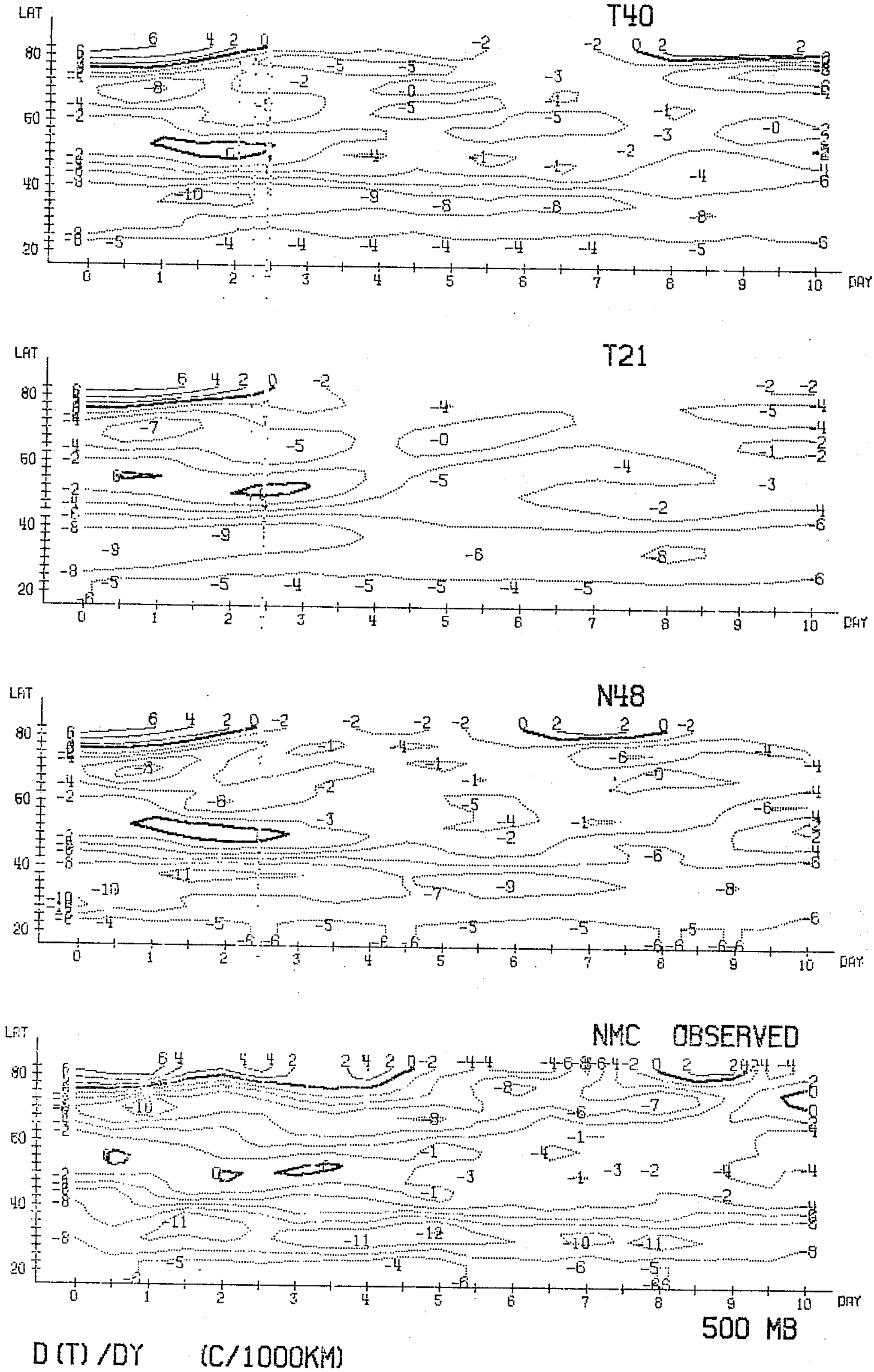

Fig. 3.1.22 Zonally averaged longitudinal temperature gradients as a function of latitude and time.

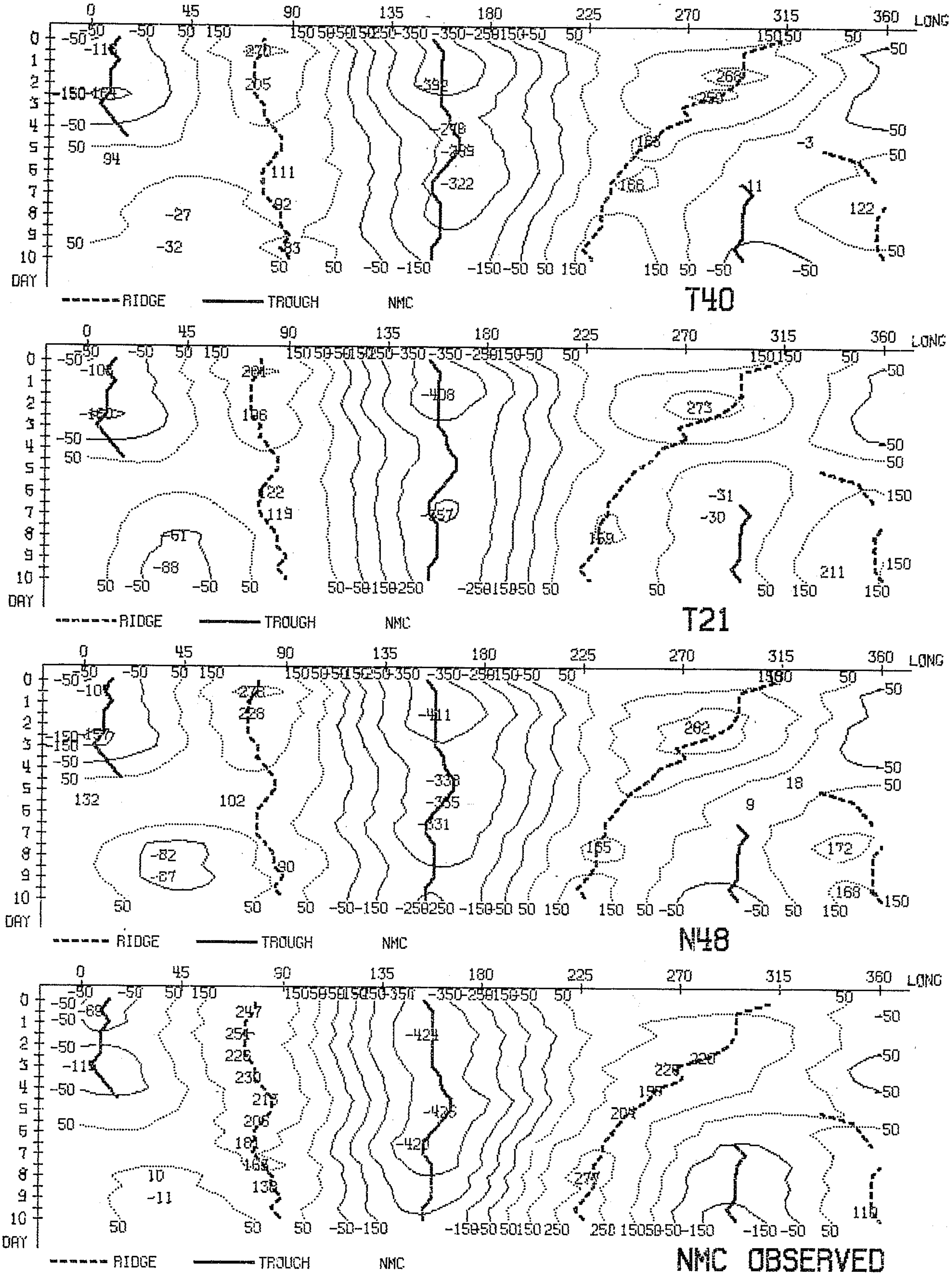

Fig.3.1.23 WAVENUMBER 1- 3 LATITUDE 50.0 N LEVEL 500 MB
GEOP. HEIGHT

Hovmöller diagram, forecast and observed.

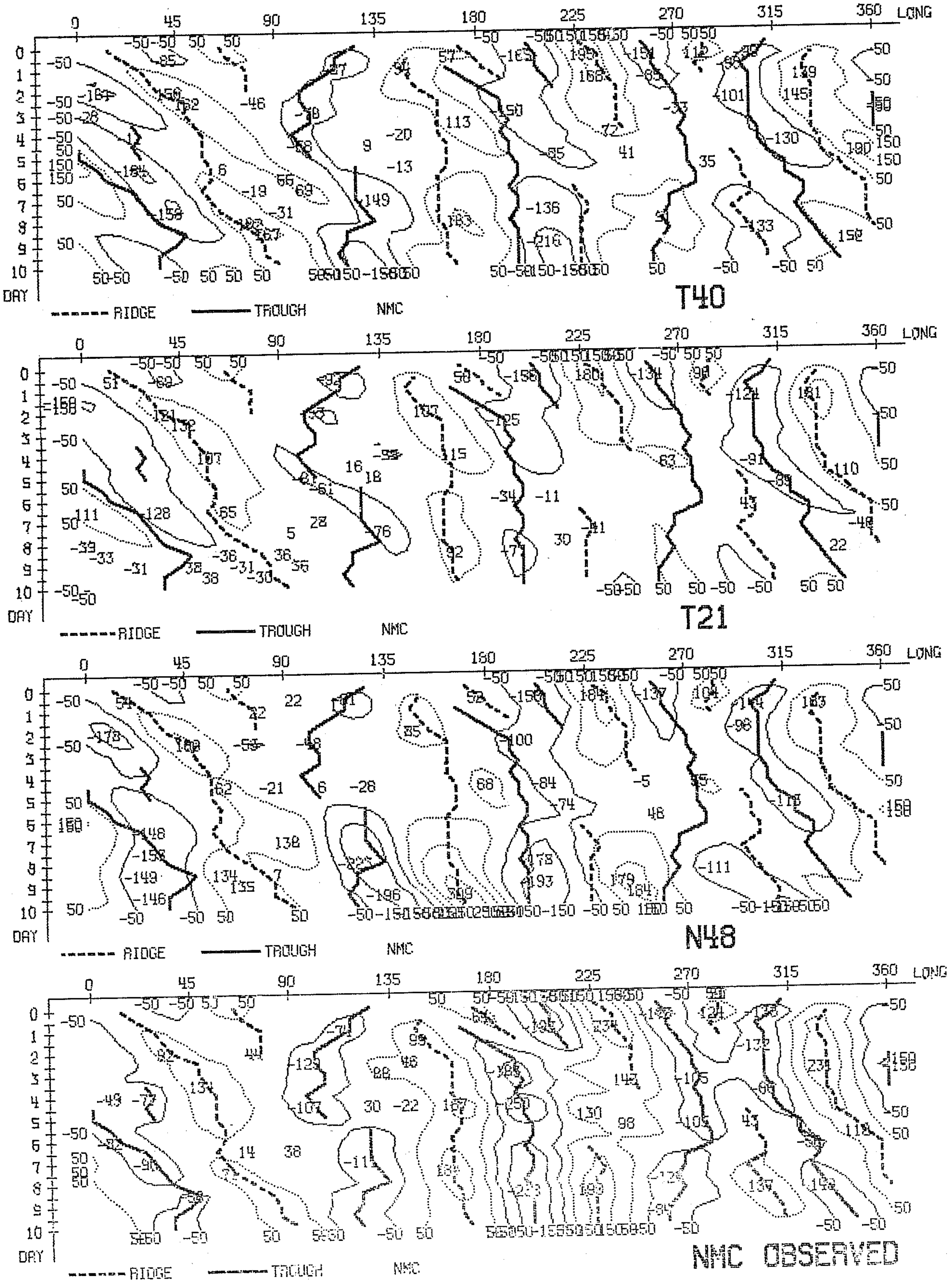

Fig.3.1.24 WAVENUMBER 4- 9 LATITUDE 50.0 N LEVEL 500 MB
GEOP. HEIGHT Hovmöller diagram, forecast and observed.

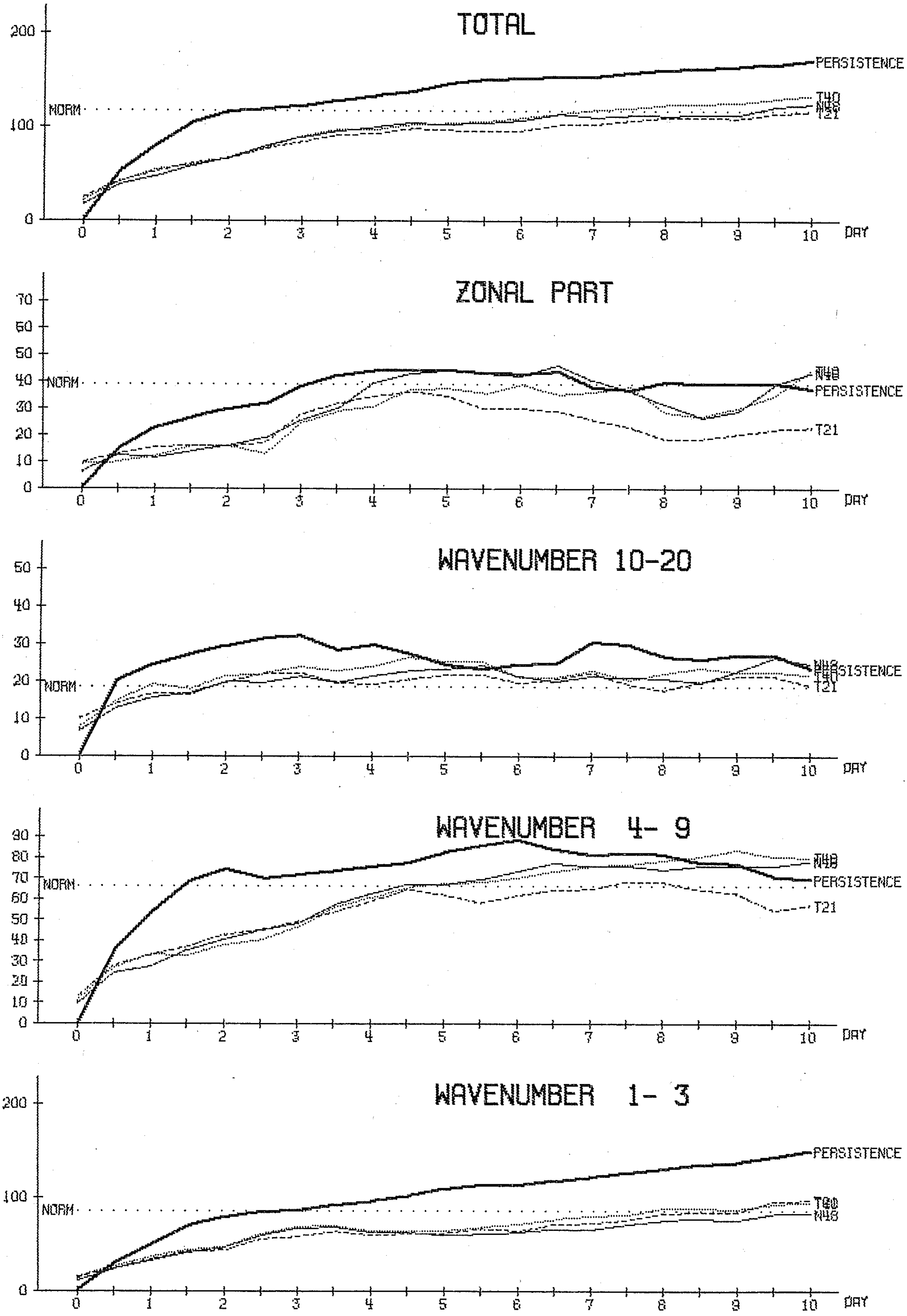

MEAN 1000- 200 MB AND 20.0- 82.5 N
RMS ERROR OF HEIGHT (M)

Fig. 3.2.1

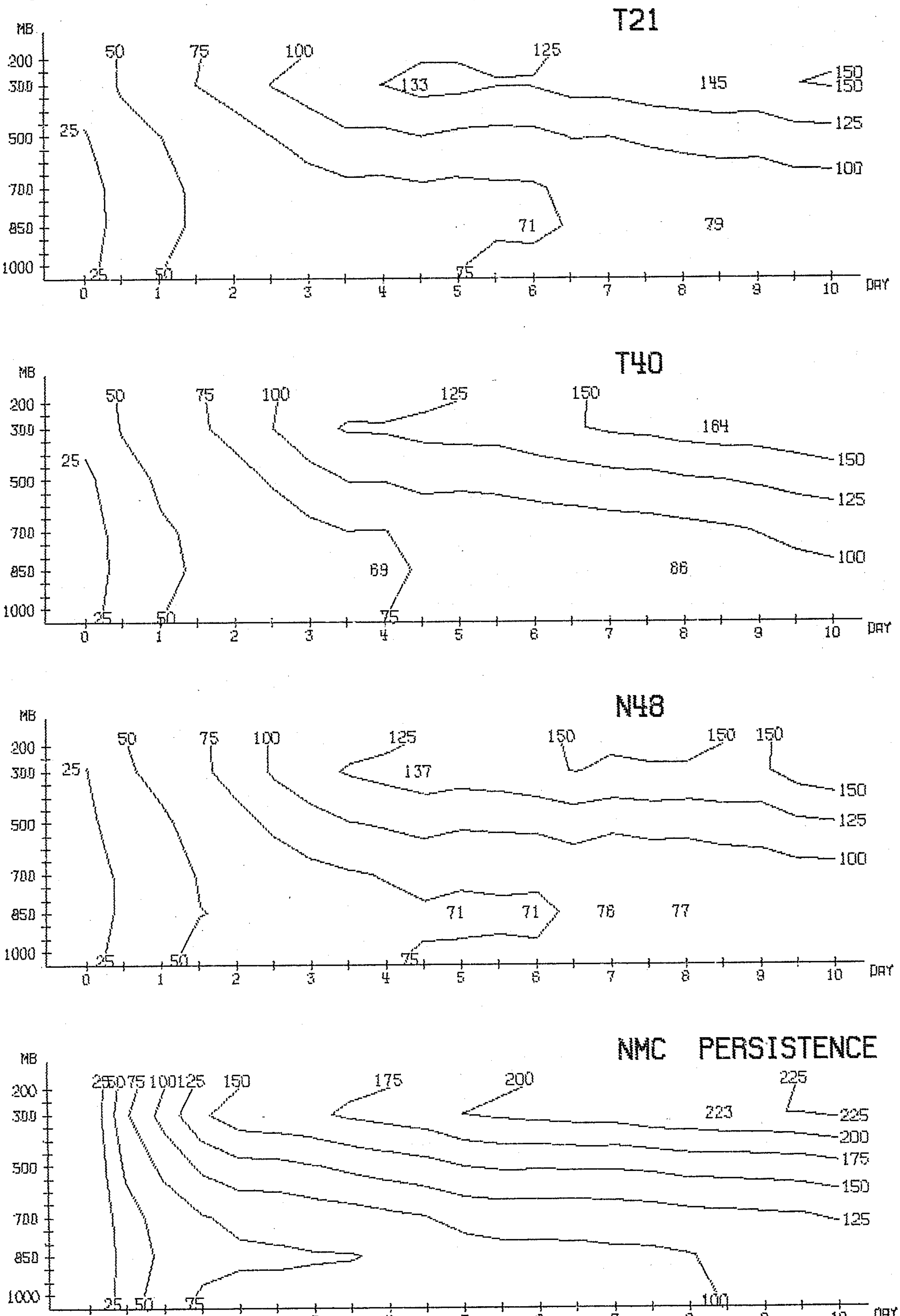

TOTAL MEAN BETWEEN 20.0 AND 82.5 N

RMS-ERROR OF HEIGHT (M)

Fig. 3.2.2

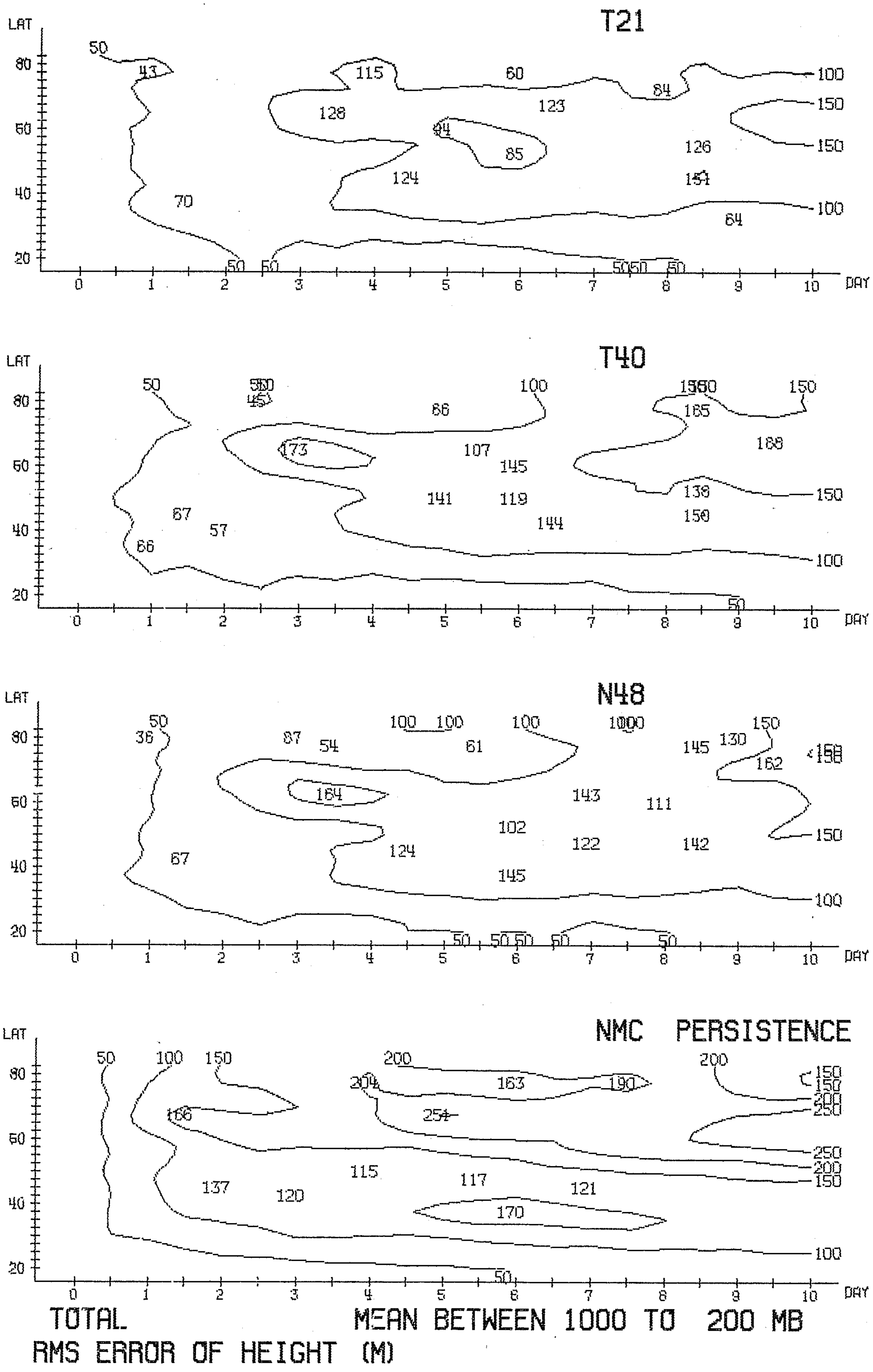
T21
T40
N48
NMC PERSISTENCE
LAT
DAY
20
40
60
80
0
1
2
3
4
5
6
7
8
9
10
50
43
115
60
84
100
128
123
150
84
85
126
124
154
70
64
128
173
107
145
141
119
144
67
57
66
165
168
138
150
87
54
61
36
164
143
111
102
122
124
67
145
142
145
130
162
200
163
190
204
254
166
250
137
120
115
117
121
170
TOTAL
MEAN BETWEEN 1000 TO 200 MB
RMS ERROR OF HEIGHT (M)

Fig. 3.2.3

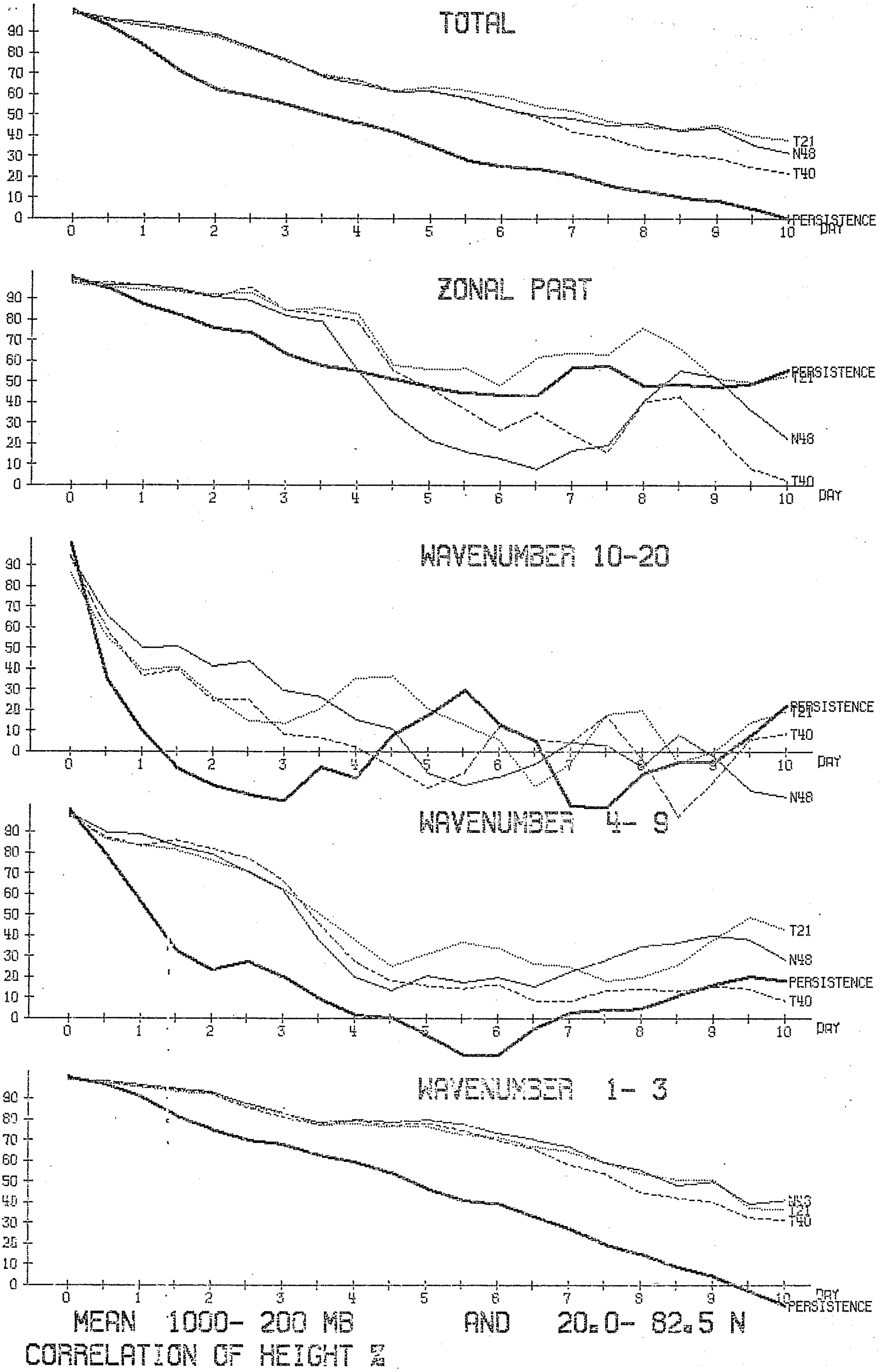
TOTAL
ZONAL PART
WAVENUMBER 10-20
WAVENUMBER 4- 9
WAVENUMBER 1- 3
0
10
20
30
40
50
60
70
80
90
0
1
2
3
4
5
6
7
8
9
10
DAY
T21
N48
T40
PERSISTENCE
MEAN 1000- 200 MB AND 20.0- 82.5 N
CORRELATION OF HEIGHT %

Fig. 3.2.4

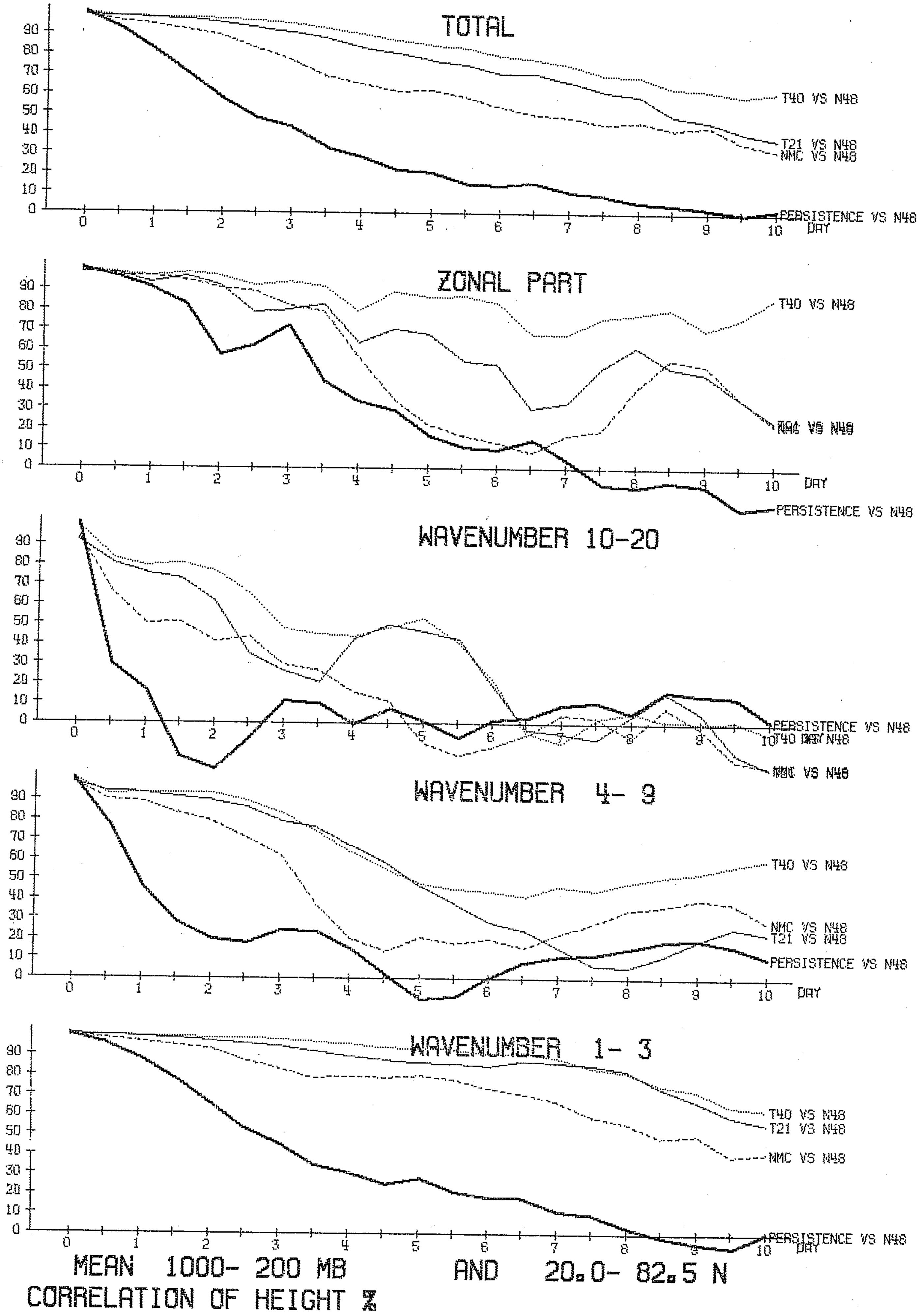
TOTAL
T40 VS N48
T21 VS N48
NMC VS N48
PERSISTENCE VS N48
ZONAL PART
T40 VS N48
T21 VS N48
NMC VS N48
PERSISTENCE VS N48
WAVENUMBER 10-20
PERSISTENCE VS N48
T40 VS N48
T21 VS N48
NMC VS N48
WAVENUMBER 4- 9
T40 VS N48
NMC VS N48
T21 VS N48
PERSISTENCE VS N48
WAVENUMBER 1- 3
T40 VS N48
T21 VS N48
NMC VS N48
PERSISTENCE VS N48
0
10
20
30
40
50
60
70
80
90
0
1
2
3
4
5
6
7
8
9
10
DAY
MEAN 1000- 200 MB AND 20.0- 82.5 N
CORRELATION OF HEIGHT %

Fig. 3.2.5

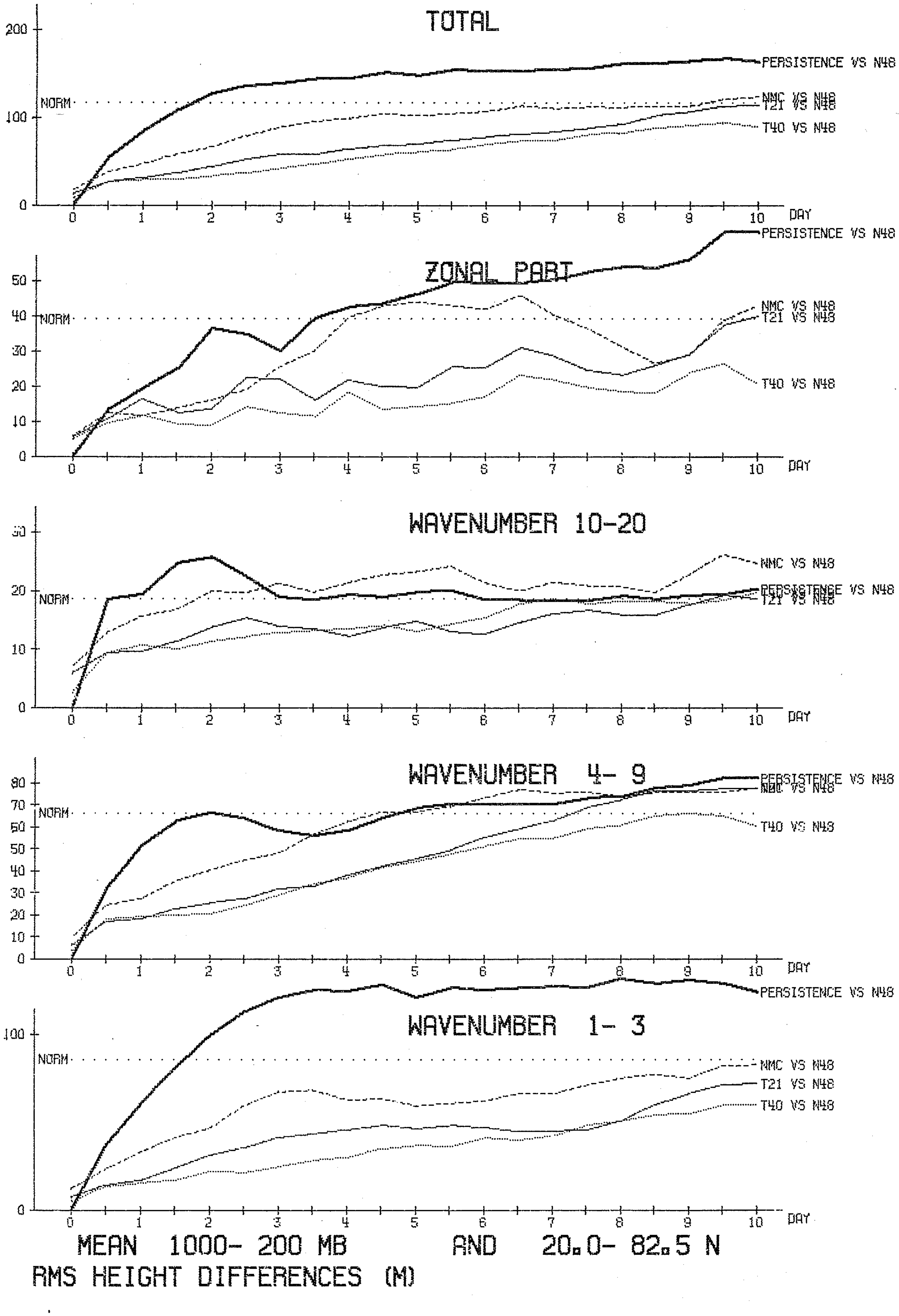
TOTAL
200
100
0
NORM
PERSISTENCE VS N48
NMC VS N48
T21 VS N48
T40 VS N48
0
1
2
3
4
5
6
7
8
9
10
DAY
ZONAL PART
50
40
30
20
10
0
NORM
PERSISTENCE VS N48
NMC VS N48
T21 VS N48
T40 VS N48
DAY
WAVENUMBER 10-20
30
20
10
0
NORM
NMC VS N48
PERSISTENCE VS N48
T40 VS N48
T21 VS N48
DAY
WAVENUMBER 4- 9
80
70
60
50
40
30
20
10
0
NORM
PERSISTENCE VS N48
NMC VS N48
T21 VS N48
T40 VS N48
DAY
WAVENUMBER 1- 3
100
0
NORM
PERSISTENCE VS N48
NMC VS N48
T21 VS N48
T40 VS N48
DAY
MEAN 1000- 200 MB AND 20.0- 82.5 N
RMS HEIGHT DIFFERENCES (M)

Fig. 3.2.6

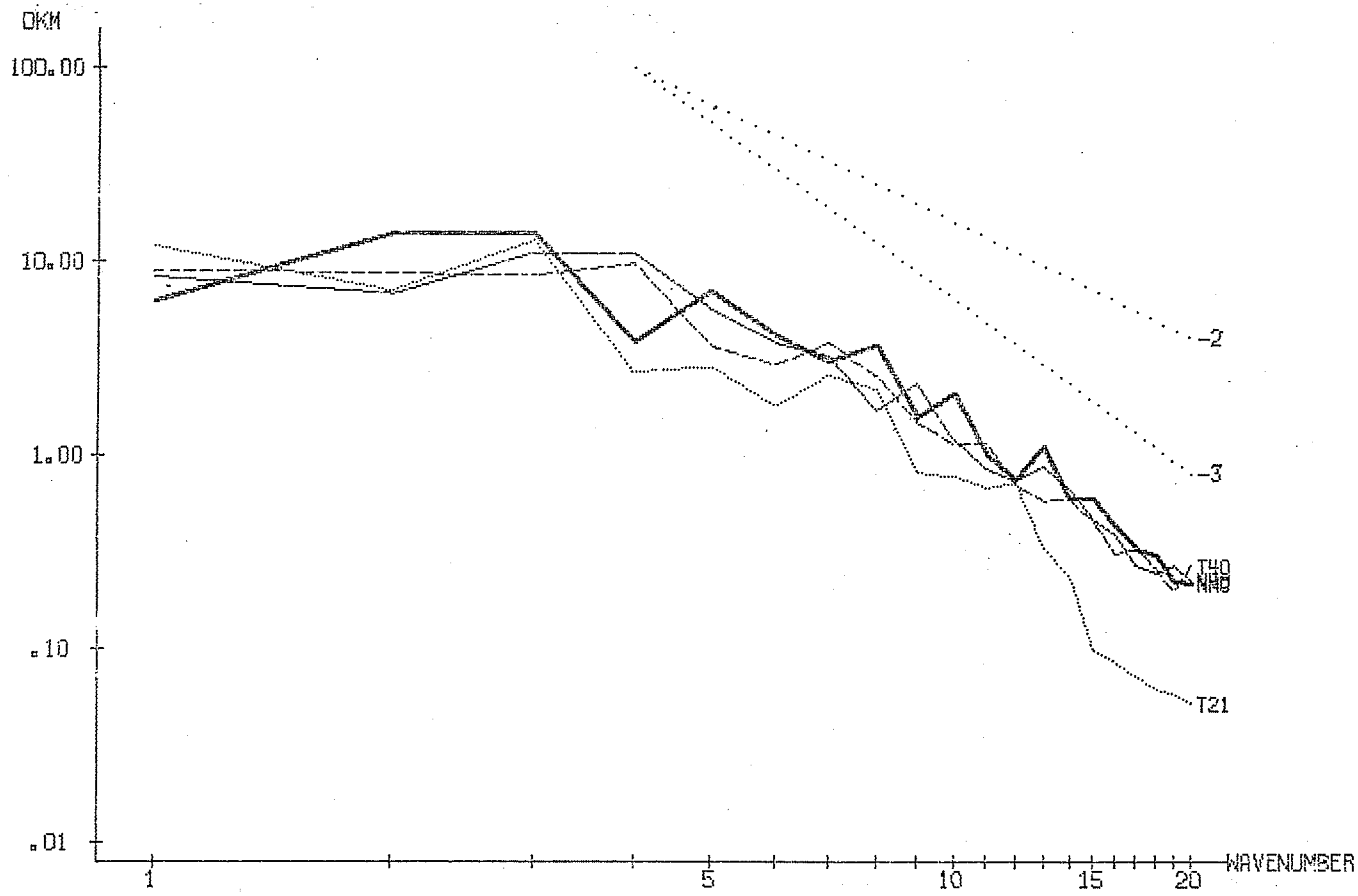

SPECTRUM OF HEIGHT 500 MB (DKM)

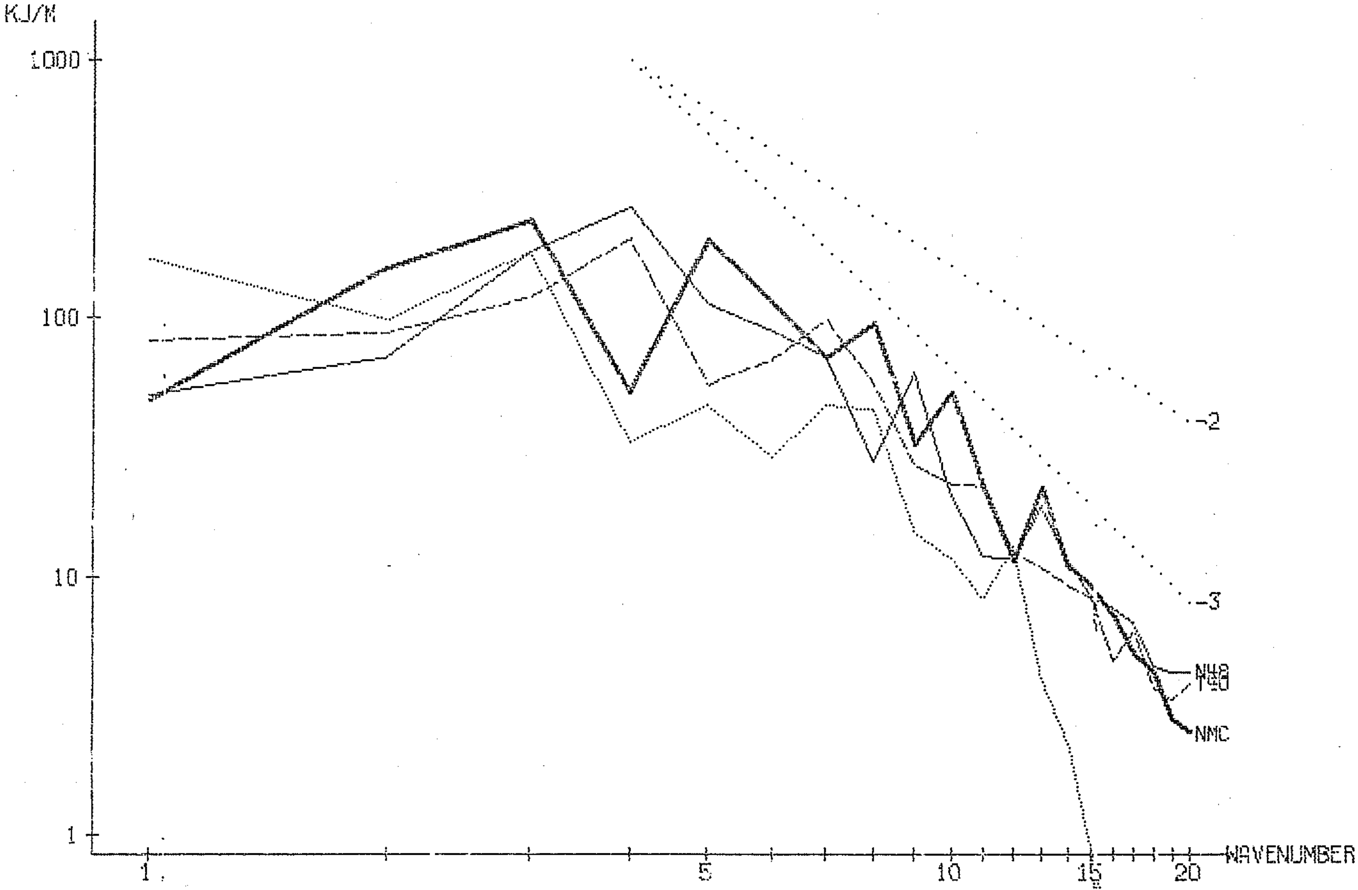

SPECTRUM OF KINETIC ENERGY TROPOSPHERE KJ/M2
DAY 7.5 TO 10.0 MEAN BETWEEN 40.0 AND 60.0

Fig. 3.3.1

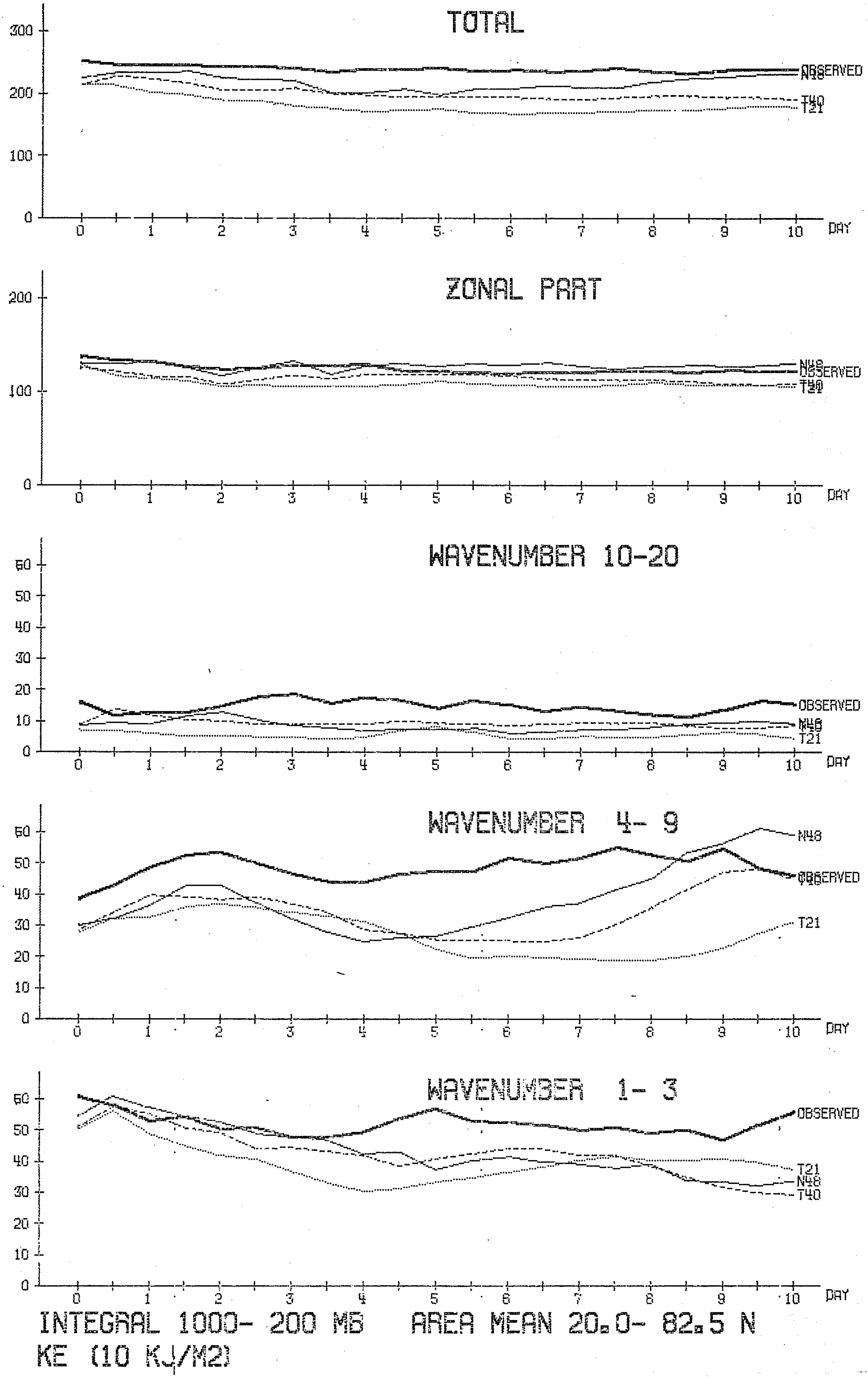
TOTAL
300
200
100
0
OBSERVED
N48
T40
T21
ZONAL PART
200
100
0
N48
OBSERVED
T40
T21
WAVENUMBER 10-20
60
50
40
30
20
10
0
OBSERVED
N48
T40
T21
WAVENUMBER 4- 9
60
50
40
30
20
10
0
N48
OBSERVED
T40
T21
WAVENUMBER 1- 3
60
50
40
30
20
10
0
OBSERVED
T21
N48
T40
0
1
2
3
4
5
6
7
8
9
10
DAY
INTEGRAL 1000- 200 MB AREA MEAN 20.0- 82.5 N
KE (10 KJ/M2)

Fig. 3.3.2.

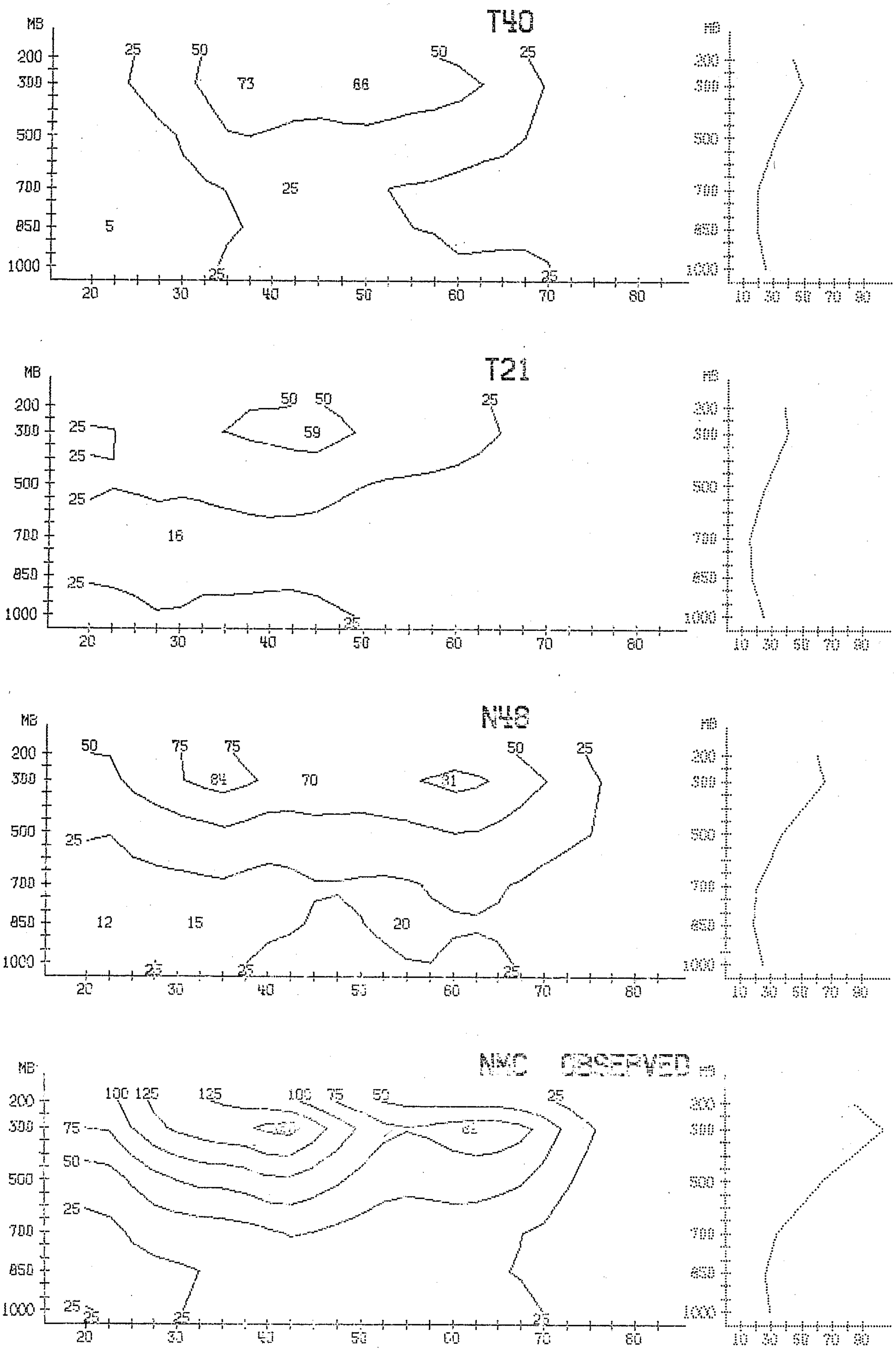

WAVENUMBER 4- 9 DAY 4.5 TO 7.0

KE (10 KJ/M2/BAR)

Fig. 3.3.3

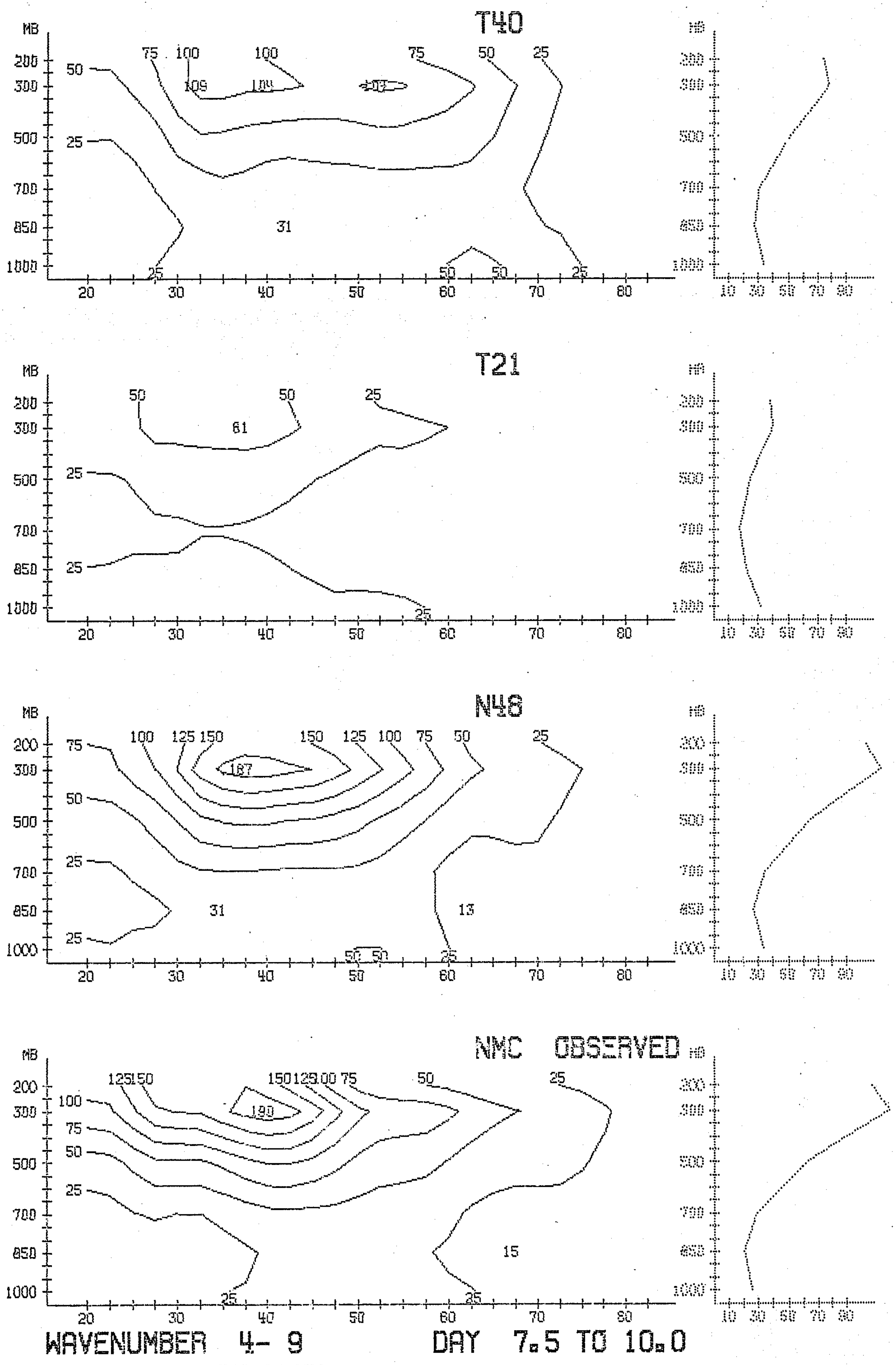
T40
MB
200
300
500
700
850
1000
50
25
75
100
109
104
107
31
20
30
40
50
60
70
80
10 30 50 70 90
T21
61
N48
125
150
187
13
NMC OBSERVED
180
15
WAVENUMBER 4- 9
DAY 7.5 TO 10.0
KE (10 KJ/M2/BAR)

Fig. 3.3.4

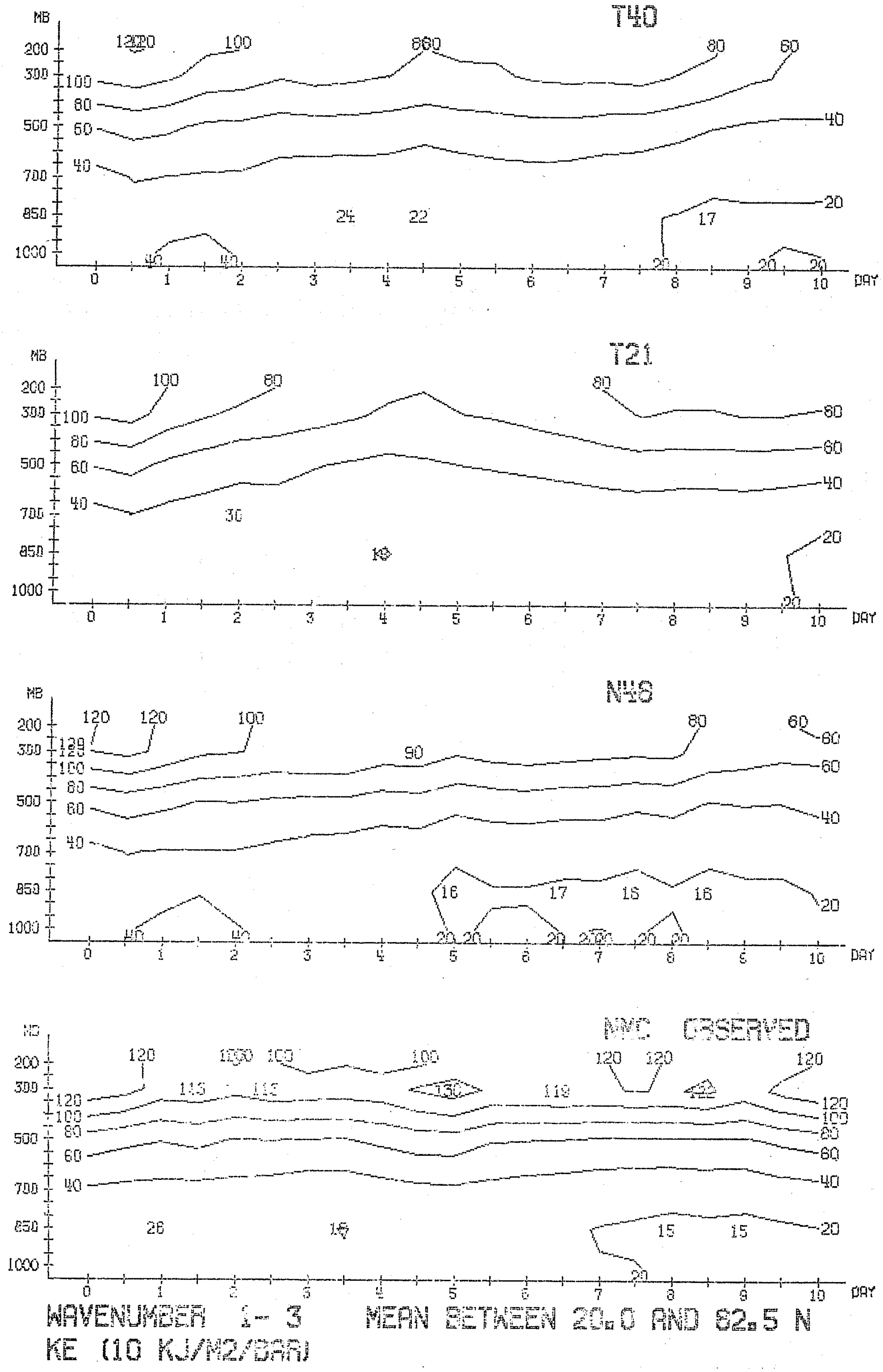
T40
T21
N48
NMC OBSERVED
MB
200
300
500
700
850
1000
DAY
0
1
2
3
4
5
6
7
8
9
10
120
100
80
60
40
20
30
24
22
17
16
15
26
90
113
112
118
130
WAVENUMBER 1- 3 MEAN BETWEEN 20.0 AND 82.5 N
KE (10 KJ/M2/BAR)

Fig. 3.3.5

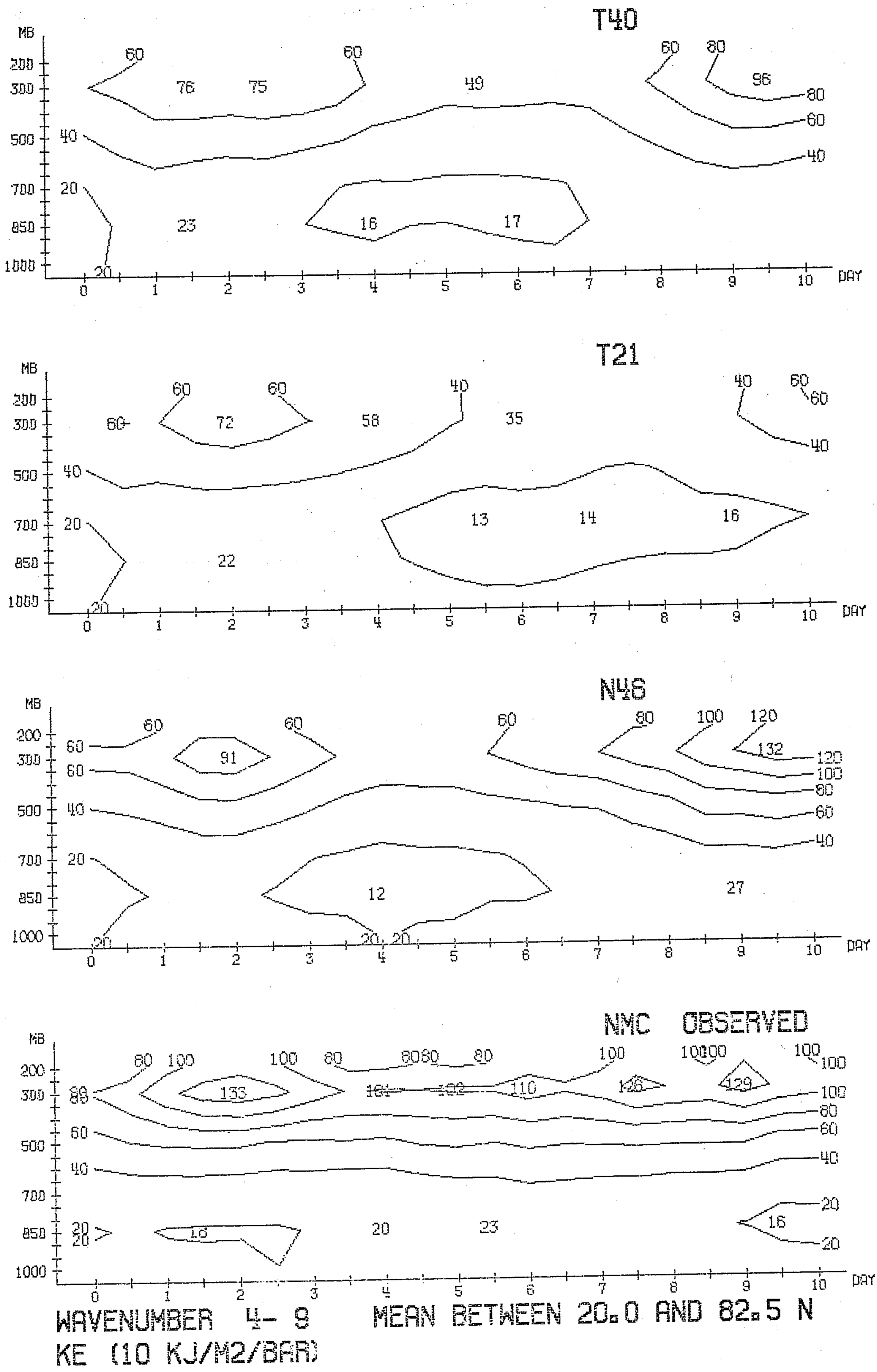
T40
T21
N48
NMC OBSERVED
MB
200
300
500
700
850
1000
DAY
0
1
2
3
4
5
6
7
8
9
10
60
76
75
49
80
96
40
20
23
16
17
72
58
35
22
13
14
91
100
120
132
12
27
133
110
126
129
WAVENUMBER 4- 9 MEAN BETWEEN 20.0 AND 82.5 N
KE (10 KJ/M2/BAR)

Fig. 3.3.6

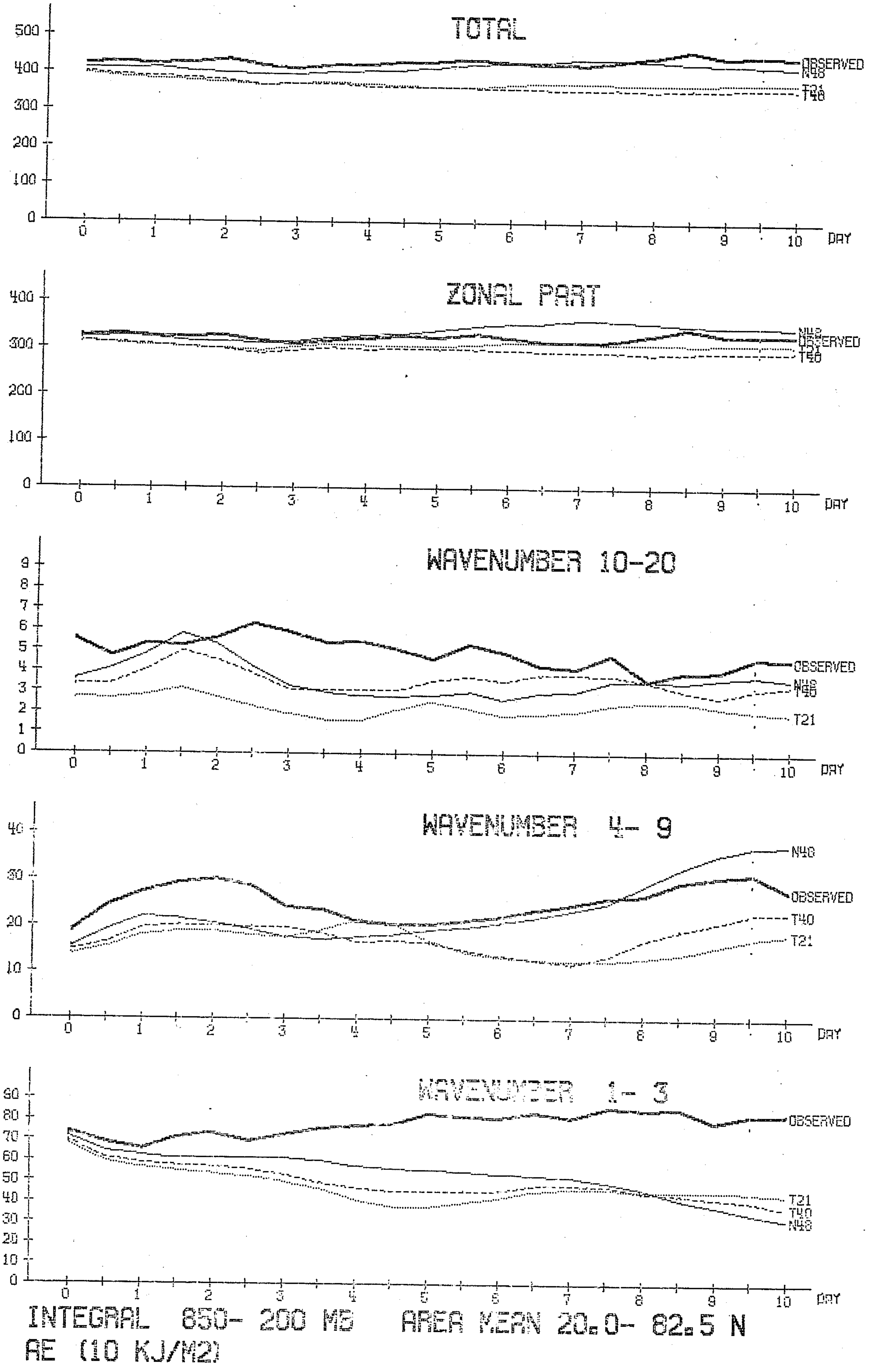
TOTAL
500
400
300
200
100
0
0 1 2 3 4 5 6 7 8 9 10 DAY
OBSERVED
N48
T21
T40
ZONAL PART
400
300
200
100
0
0 1 2 3 4 5 6 7 8 9 10 DAY
N48
OBSERVED
T21
T40
WAVENUMBER 10-20
9
8
7
6
5
4
3
2
1
0
0 1 2 3 4 5 6 7 8 9 10 DAY
OBSERVED
N48
T40
T21
WAVENUMBER 4- 9
40
30
20
10
0
0 1 2 3 4 5 6 7 8 9 10 DAY
N48
OBSERVED
T40
T21
WAVENUMBER 1- 3
90
80
70
60
50
40
30
20
10
0
0 1 2 3 4 5 6 7 8 9 10 DAY
OBSERVED
T21
T40
N48
INTEGRAL 850- 200 MB AREA MEAN 20.0- 82.5 N
AE (10 KJ/M2)

Fig. 3.3.7

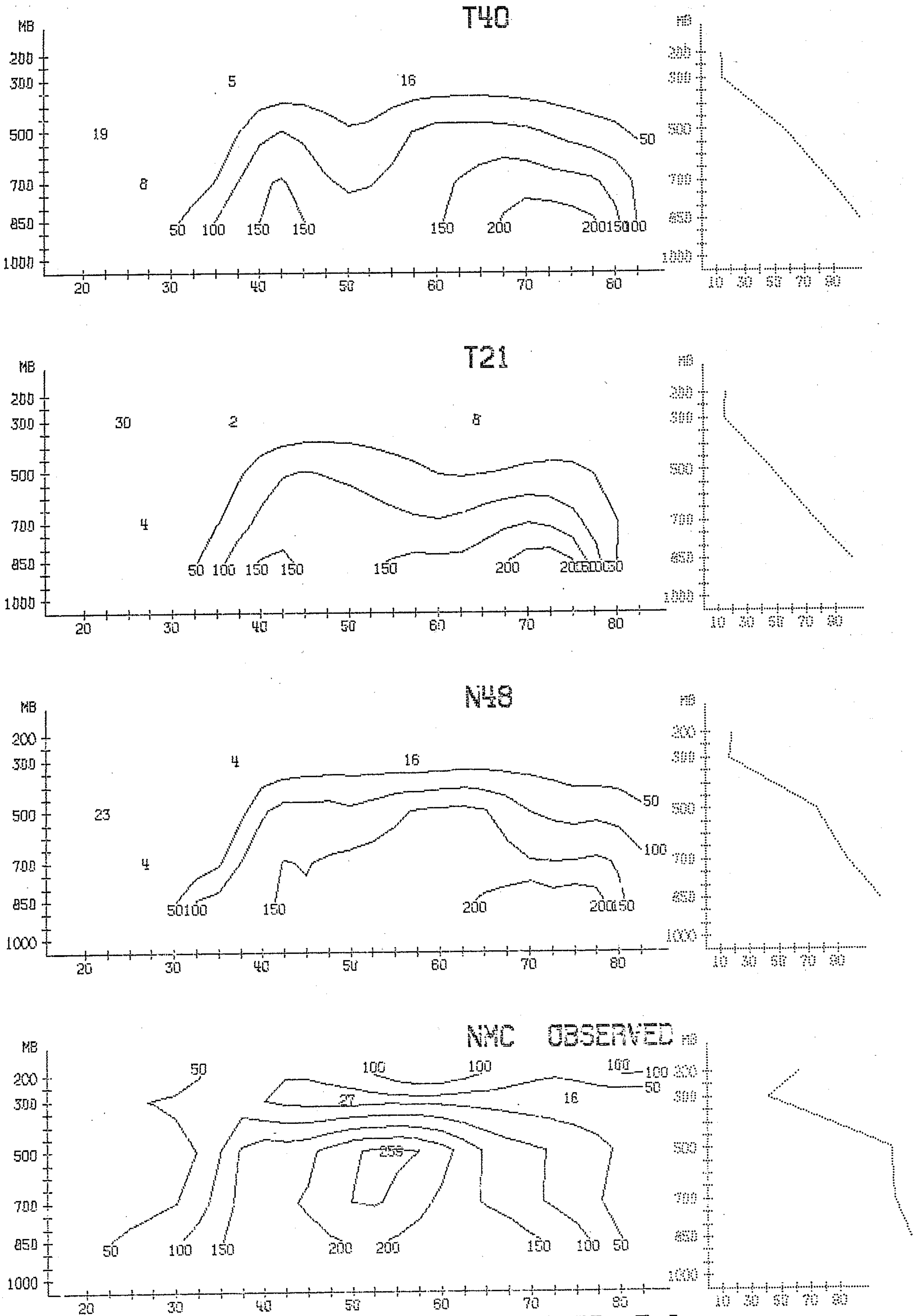

WAVENUMBER 1- 3 DAY 4.5 TO 7.0

AE (10 KJ/M2/BAR)

Fig. 3.3.8.

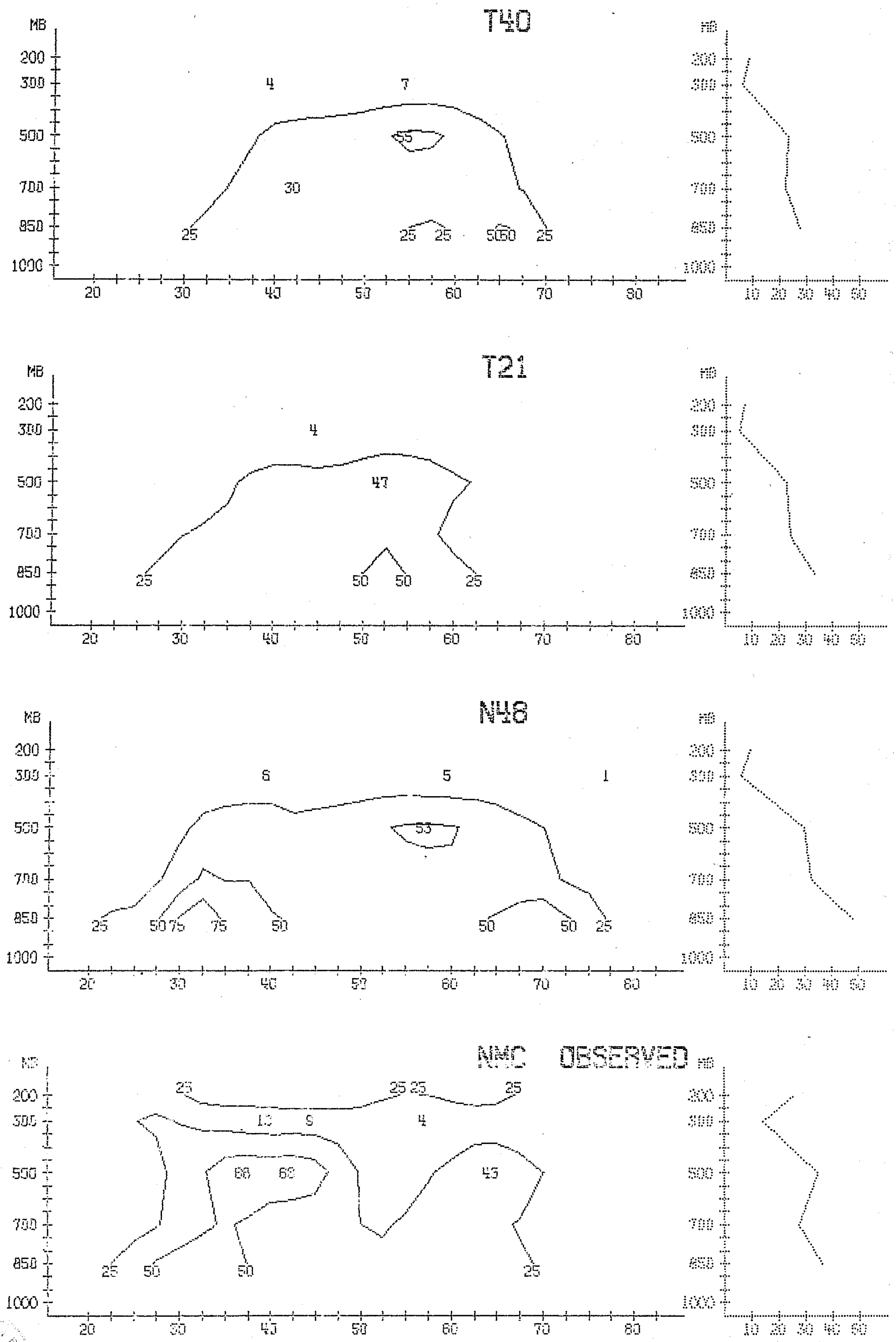

WAVENUMBER 4- 9 DAY 4.5 TO 7.0
AE (10 KJ/M2/BAR)

Fig. 3.3.9.

ECMWF LIBRARY

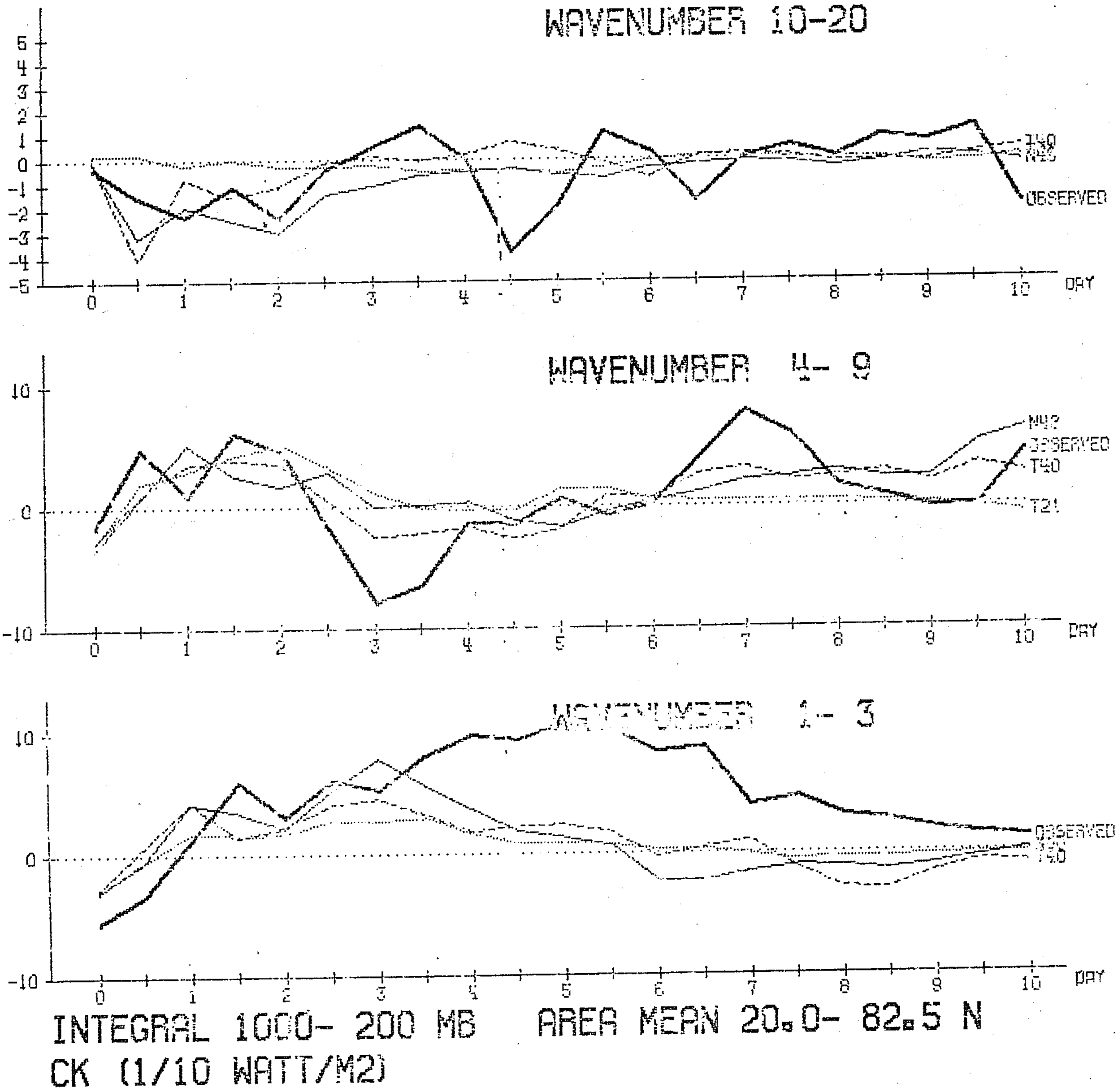
WAVENUMBER 10-20
5
4
3
2
1
0
-1
-2
-3
-4
-5
0
1
2
3
4
5
6
7
8
9
10
DAY
T40
N48
OBSERVED
WAVENUMBER 4- 9
10
0
-10
N48
OBSERVED
T40
T21
DAY
WAVENUMBER 1- 3
10
0
-10
OBSERVED
T40
DAY
INTEGRAL 1000- 200 MB AREA MEAN 20.0- 82.5 N
CK (1/10 WATT/M2)

Fig. 3.3.10

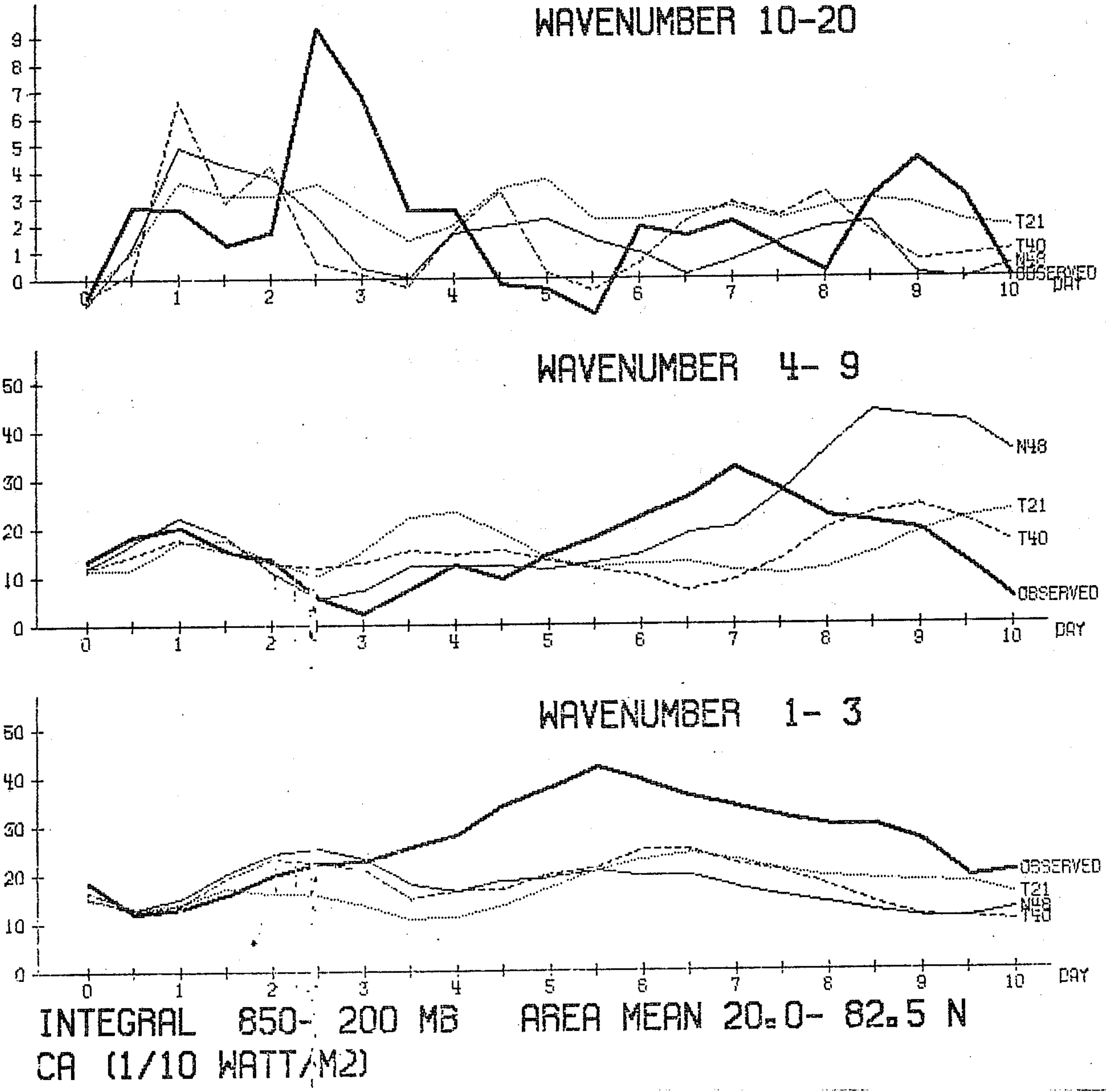
WAVENUMBER 10-20
0
1
2
3
4
5
6
7
8
9
0
1
2
3
4
5
6
7
8
9
10
DAY
T21
T40
N48
OBSERVED
WAVENUMBER 4- 9
0
10
20
30
40
50
N48
T21
T40
OBSERVED
DAY
WAVENUMBER 1- 3
0
10
20
30
40
50
OBSERVED
T21
N48
T40
DAY
INTEGRAL 850- 200 MB AREA MEAN 20.0- 82.5 N
CA (1/10 WATT/M2)

Fig. 3.3.11

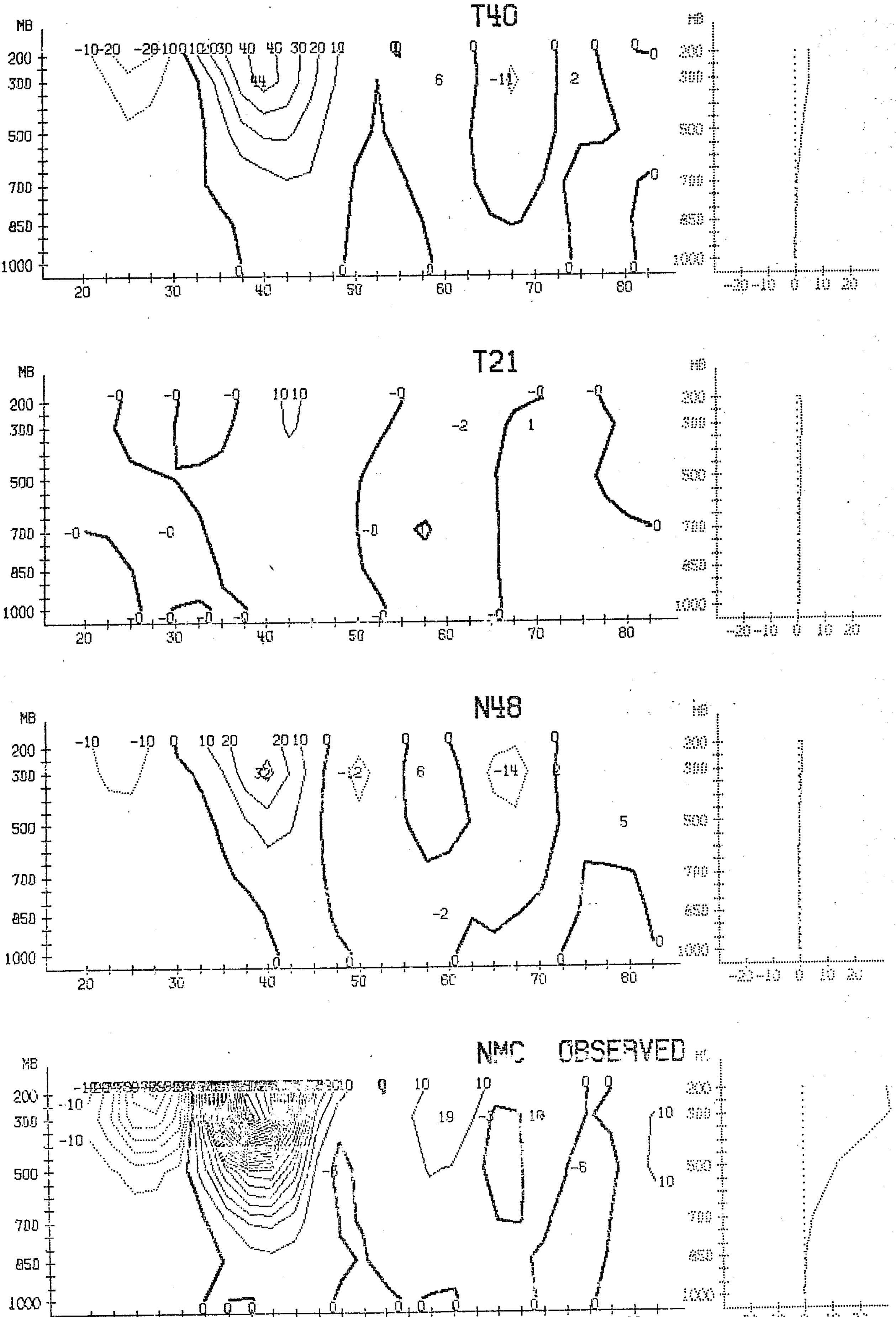

WAVENUMBER 1- 3 DAY 4.5 TO 7.0
CK (1/10 WATT/M2/BAR)

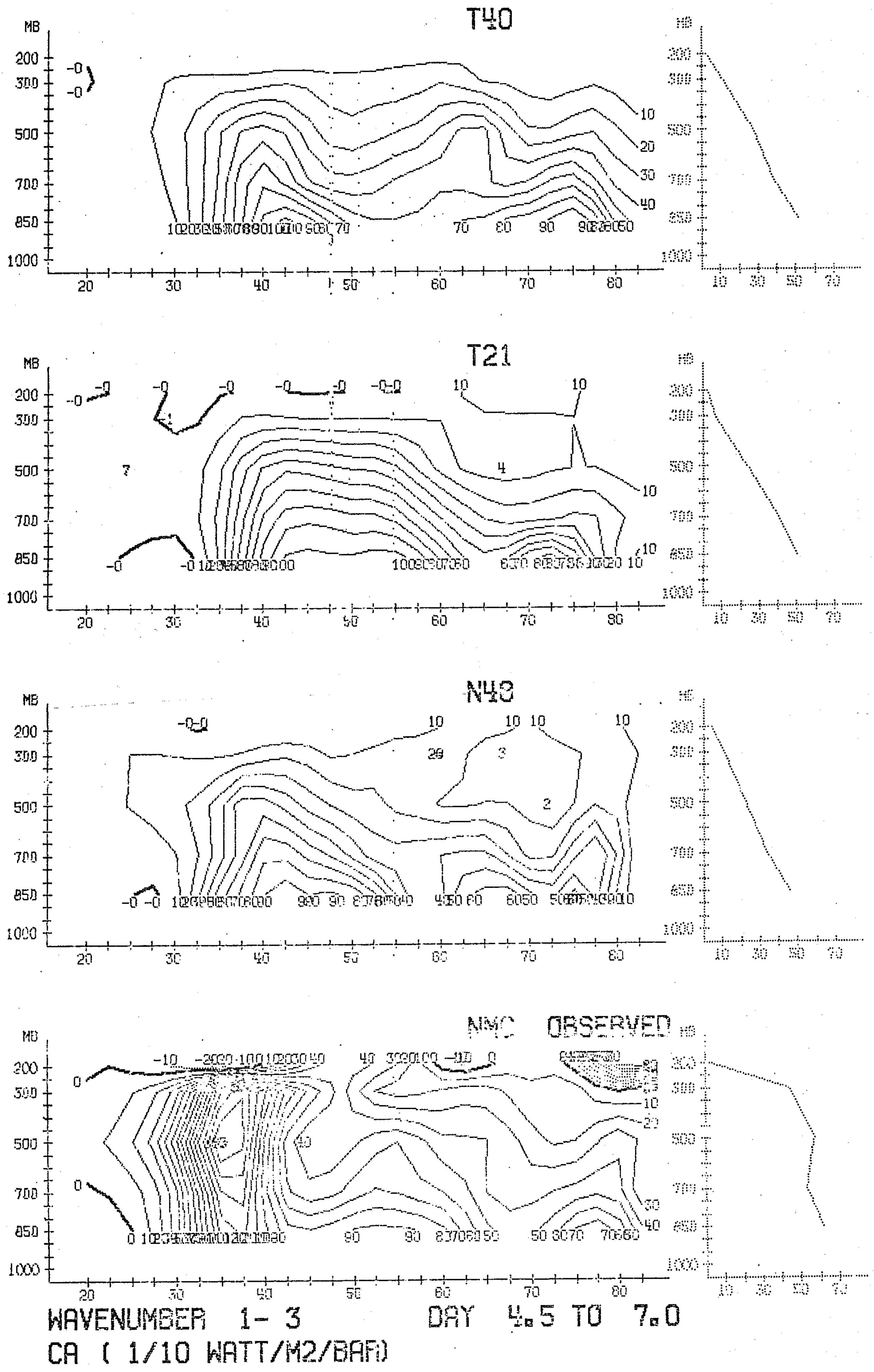
T40
T21
N48
NMC OBSERVED
MB
200
300
500
700
850
1000
20
30
40
50
60
70
80
10
30
50
70
WAVENUMBER 1- 3
DAY 4.5 TO 7.0
CA (1/10 WATT/M2/BAR)

Fig. 3.3.13

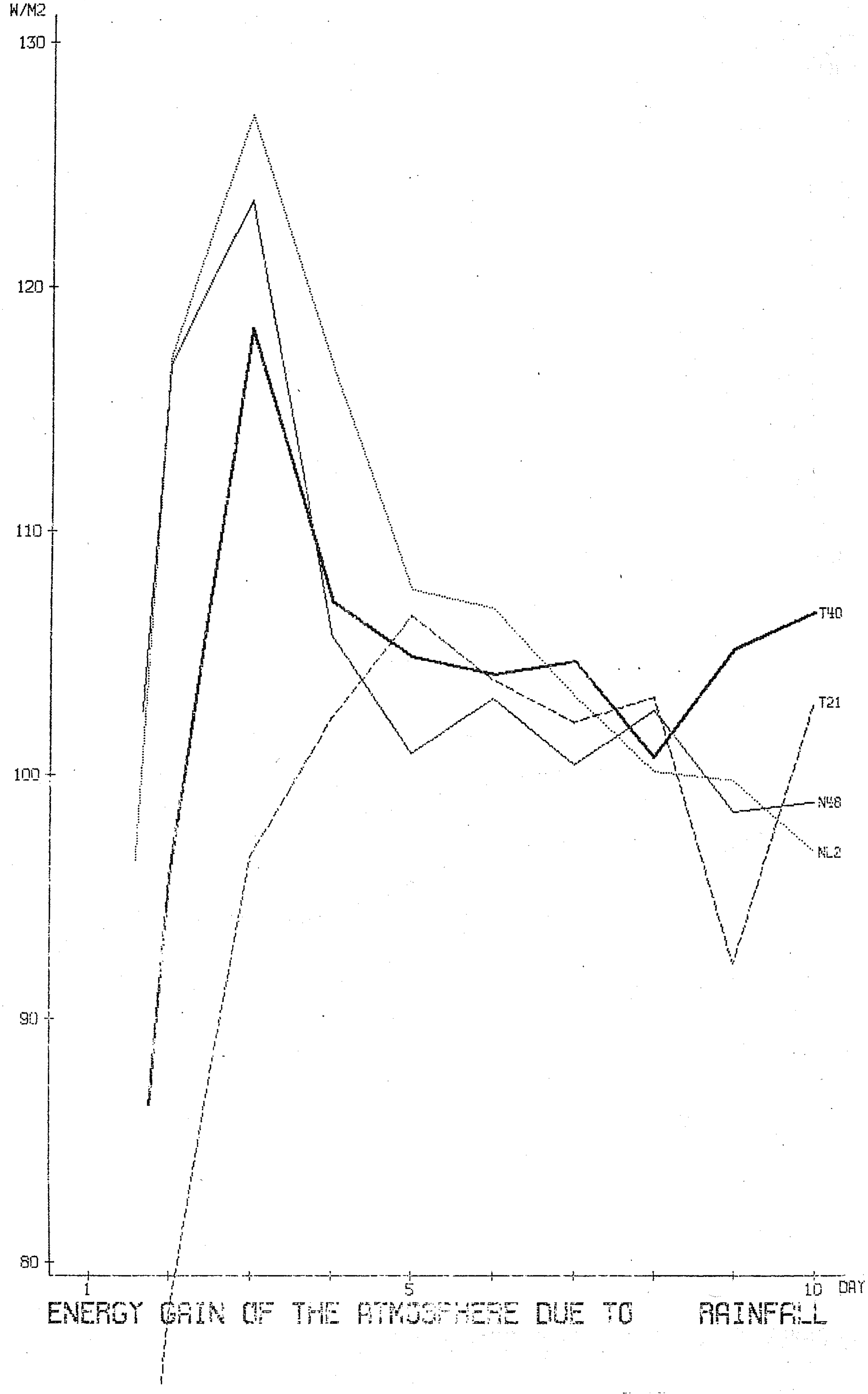

ENERGY GAIN OF THE ATMOSPHERE DUE TO RAINFALL

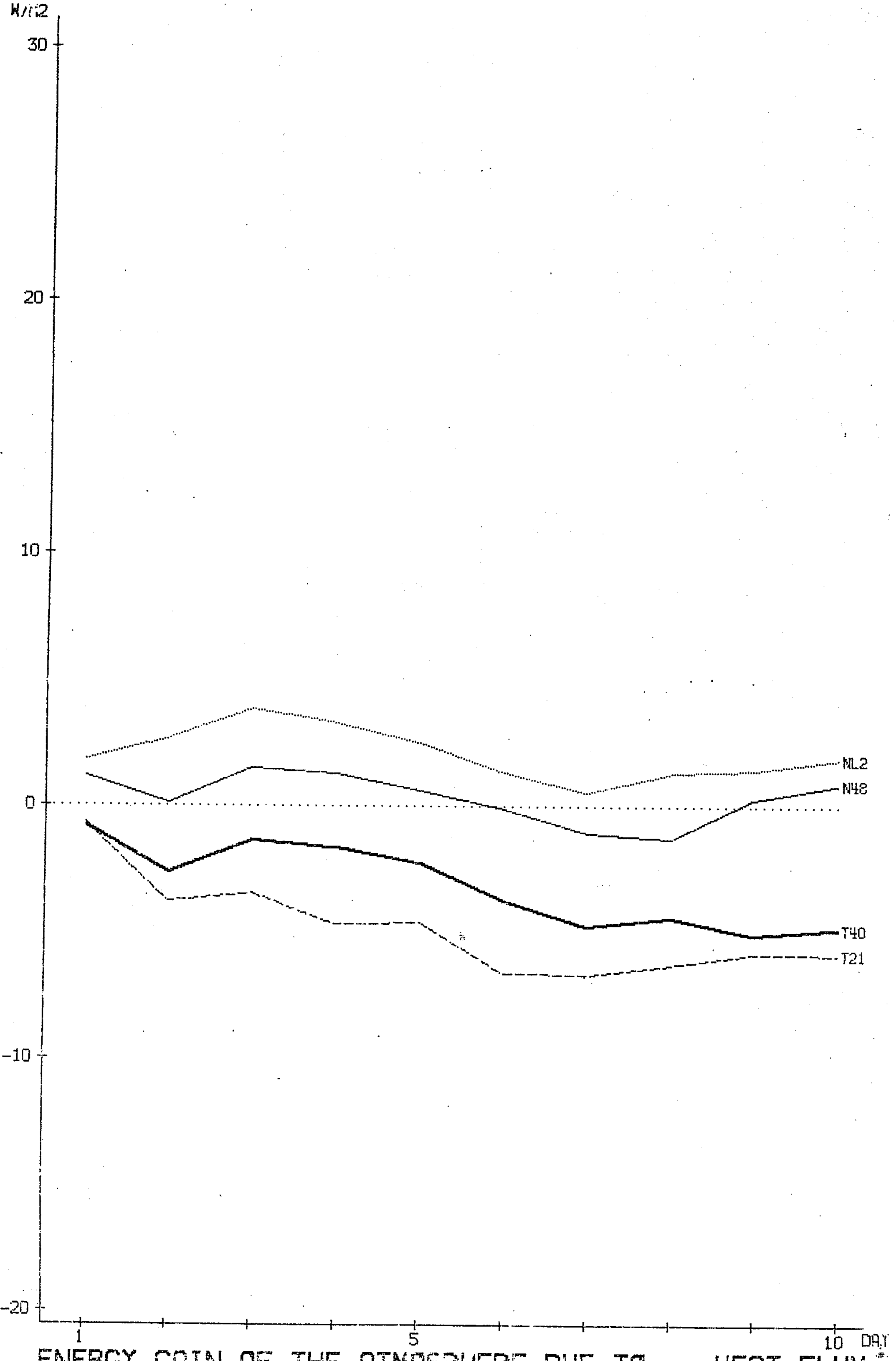

ENERGY GAIN OF THE ATMOSPHERE DUE TO HEAT FLUX

Fig. 3.3.15

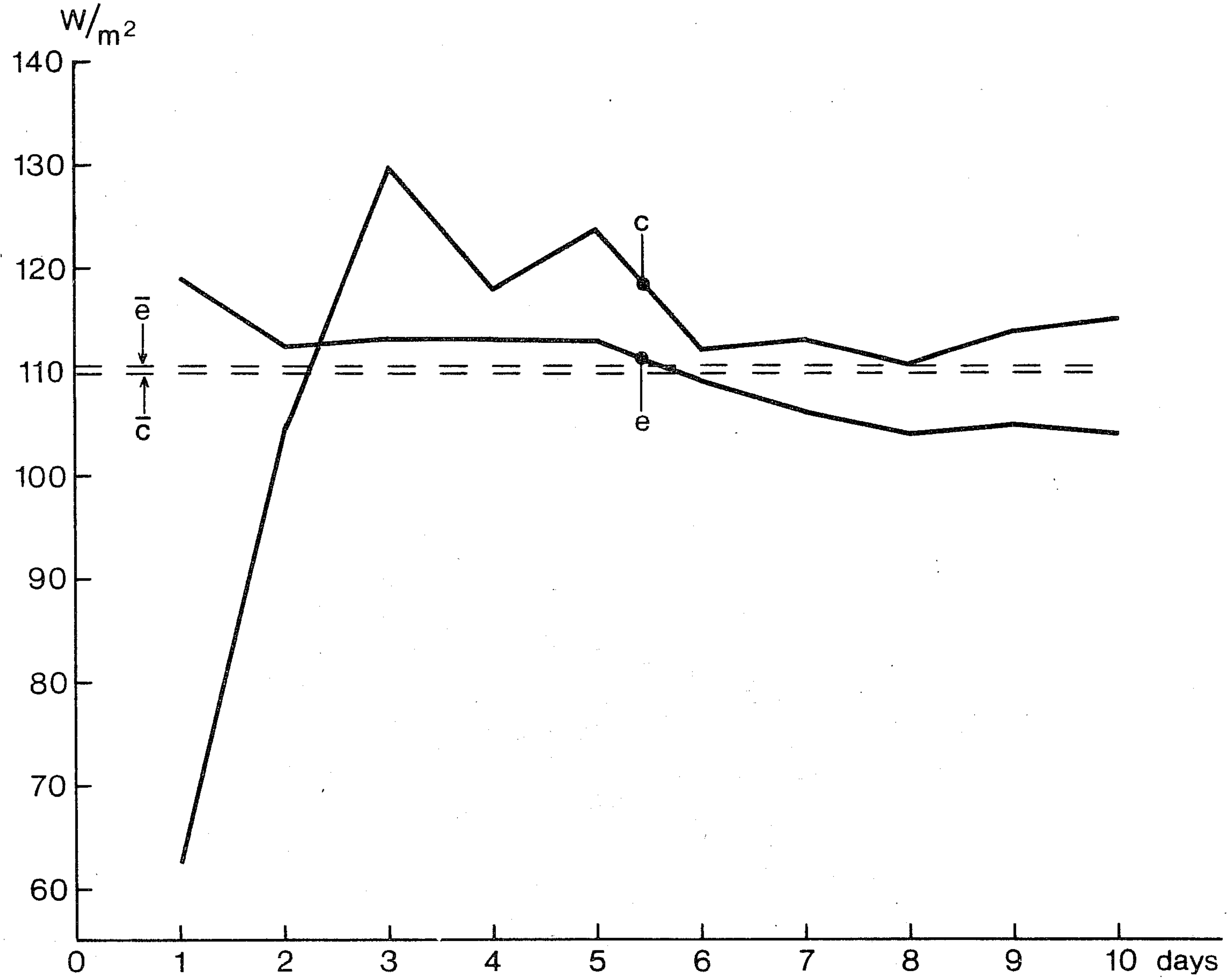

Fig. 3.3.16 Total condensation (c) and evaporation (e) in the T40 model as a function of time. The dashed lines indicate the averages of both quantities over the 10-day period.

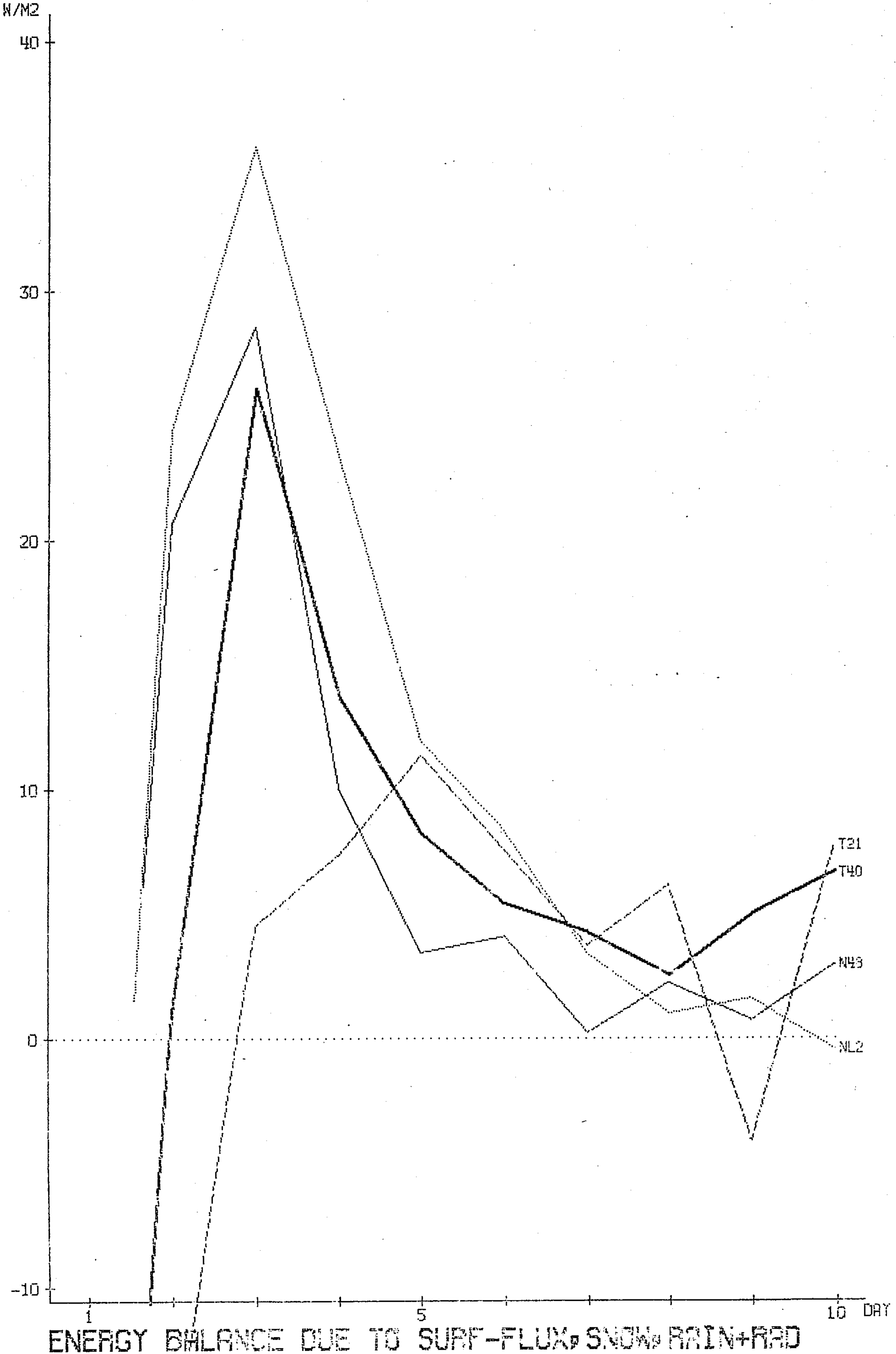
W/M2
40
30
20
10
0
-10
1
5
10
DAY
T21
T40
N43
NL2
ENERGY BALANCE DUE TO SURF-FLUX, SNOW, RAIN+RAD

Fig. 3.3.17

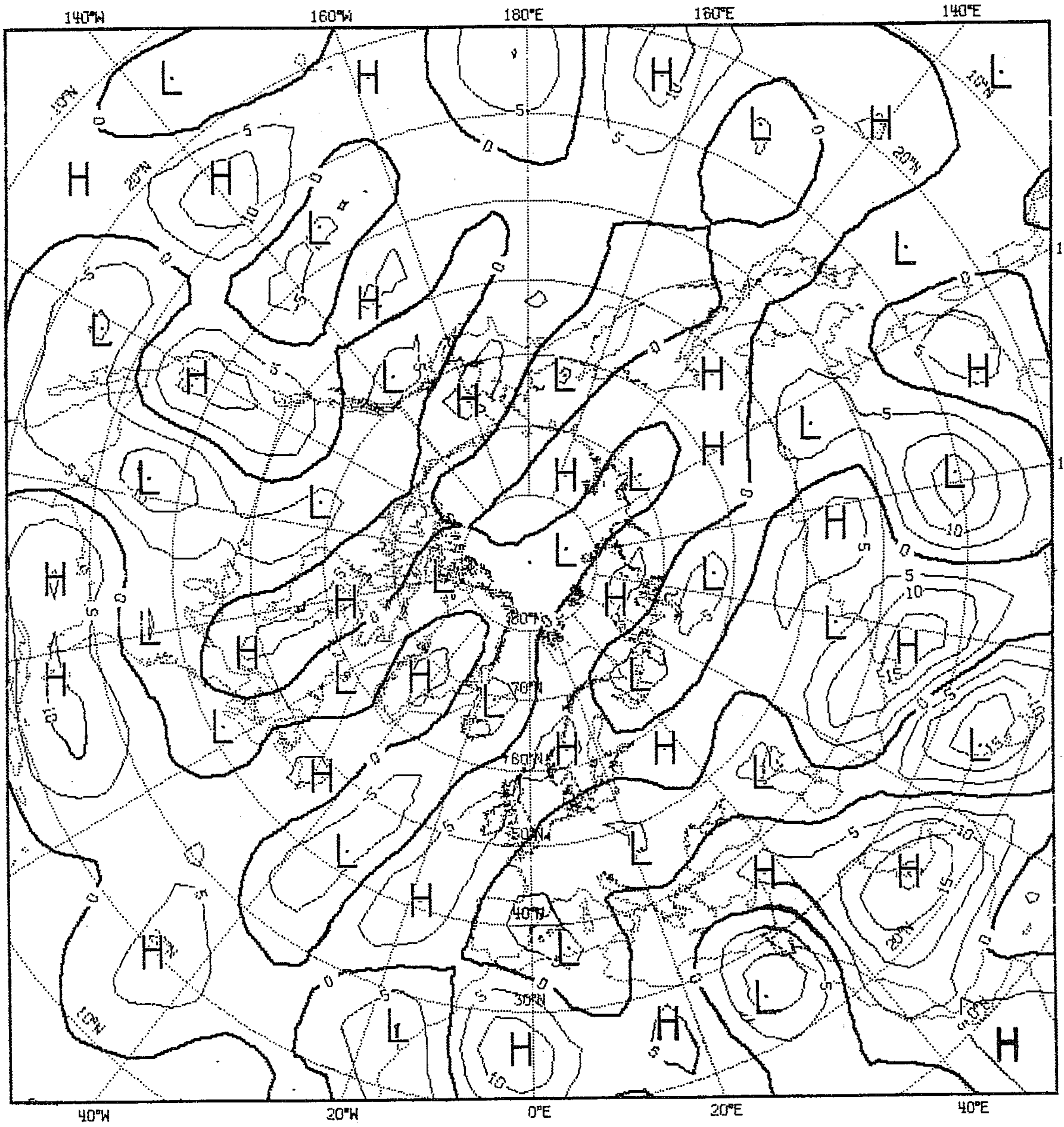

Fig. 3.3.18 Divergence of initial data set at lowest level. Units: 10^{-6} $\sec^{-1}$.

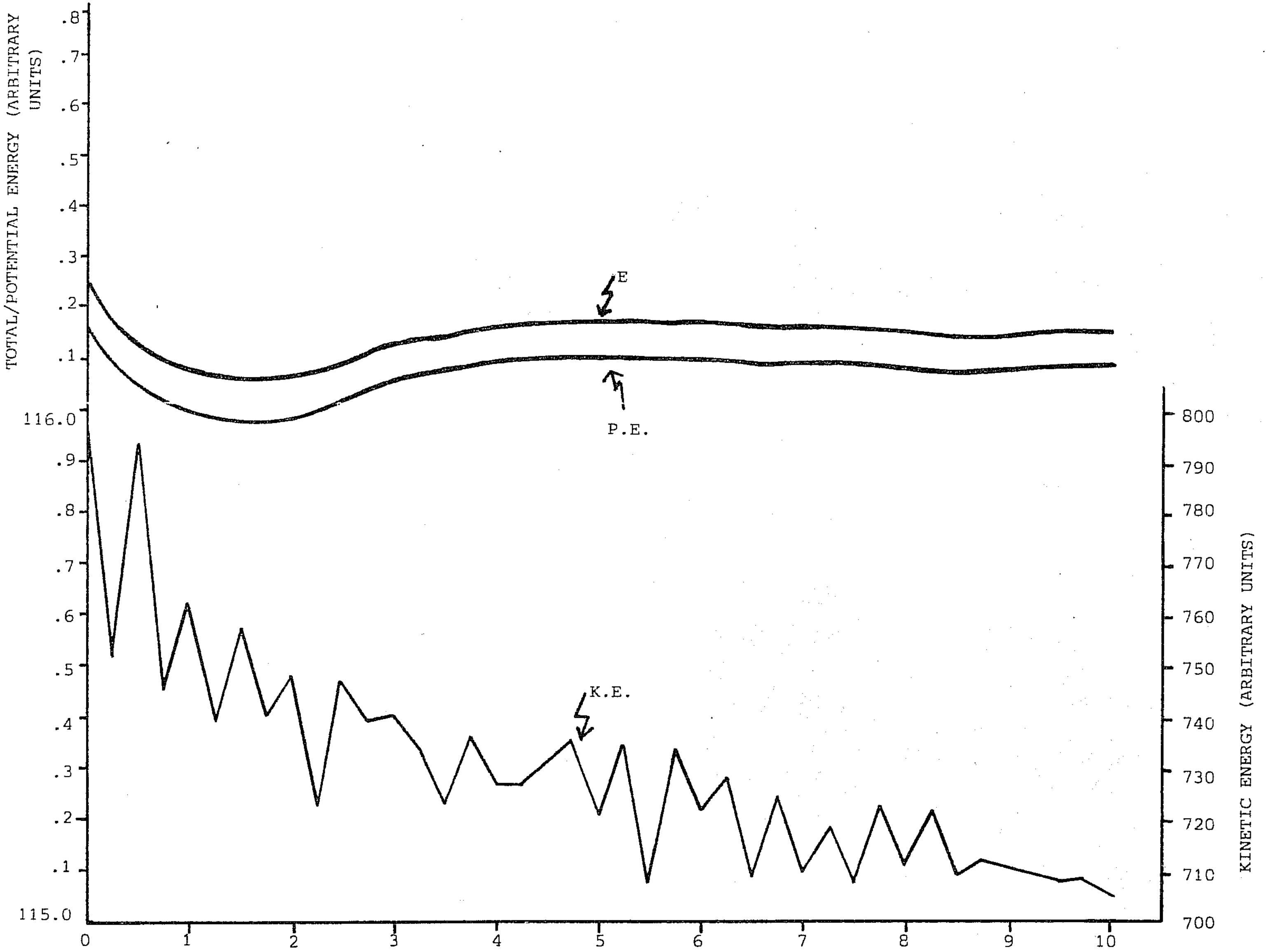

<u>Fig. 3.3.19</u> Global kinetic (K.E.) potential + internal (P.E.) and total (E) energy as a function of time in the T40 integration.

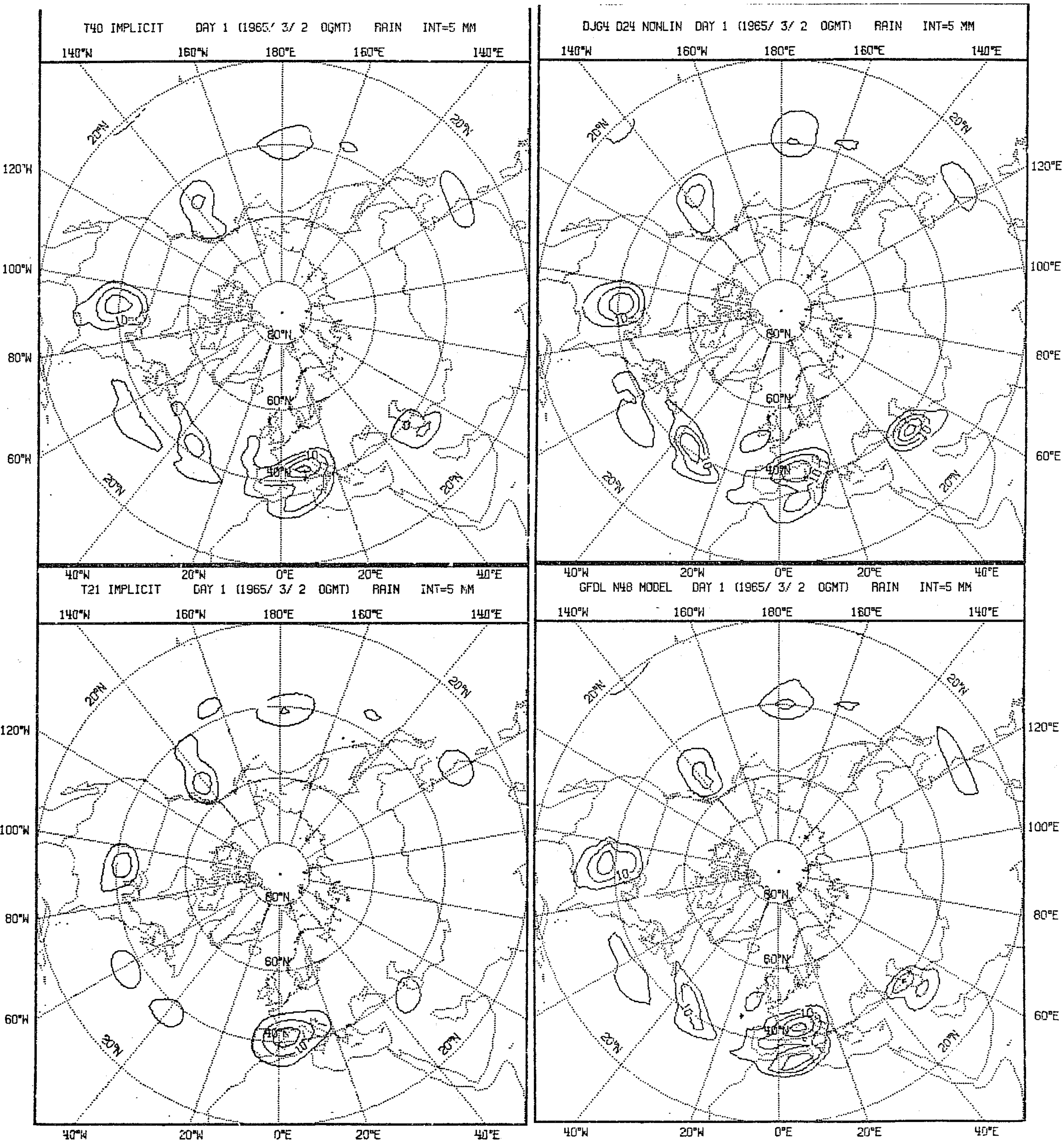

a. b.

Fig. 3.4.1 Predicted 24h accumulated rainfall patterns over the northern hemisphere, day 1.

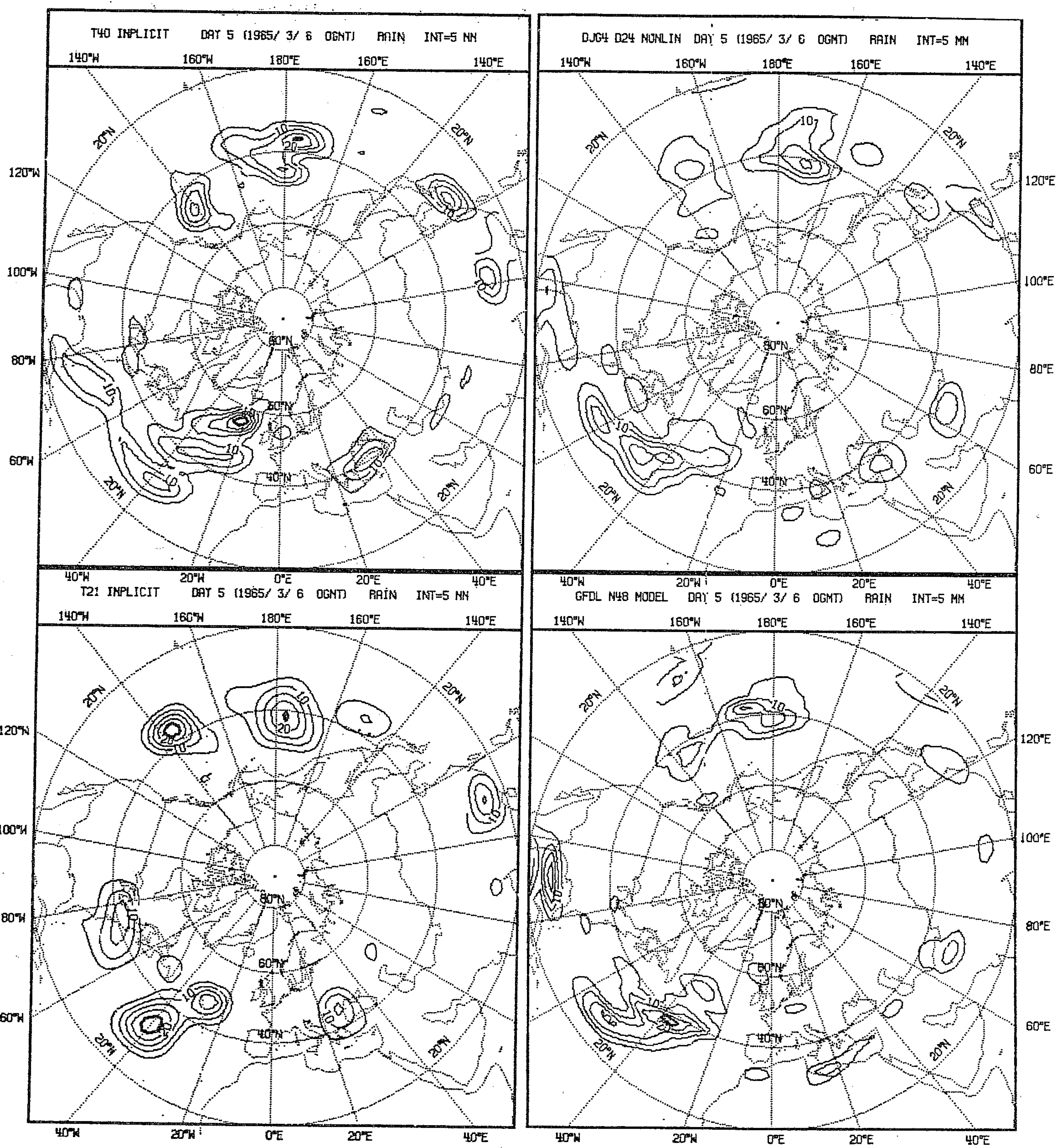

a.

b.

Fig. 3.4.2 Predicted 24h accumulated rainfall patterns over the northern hemisphere, day 5.

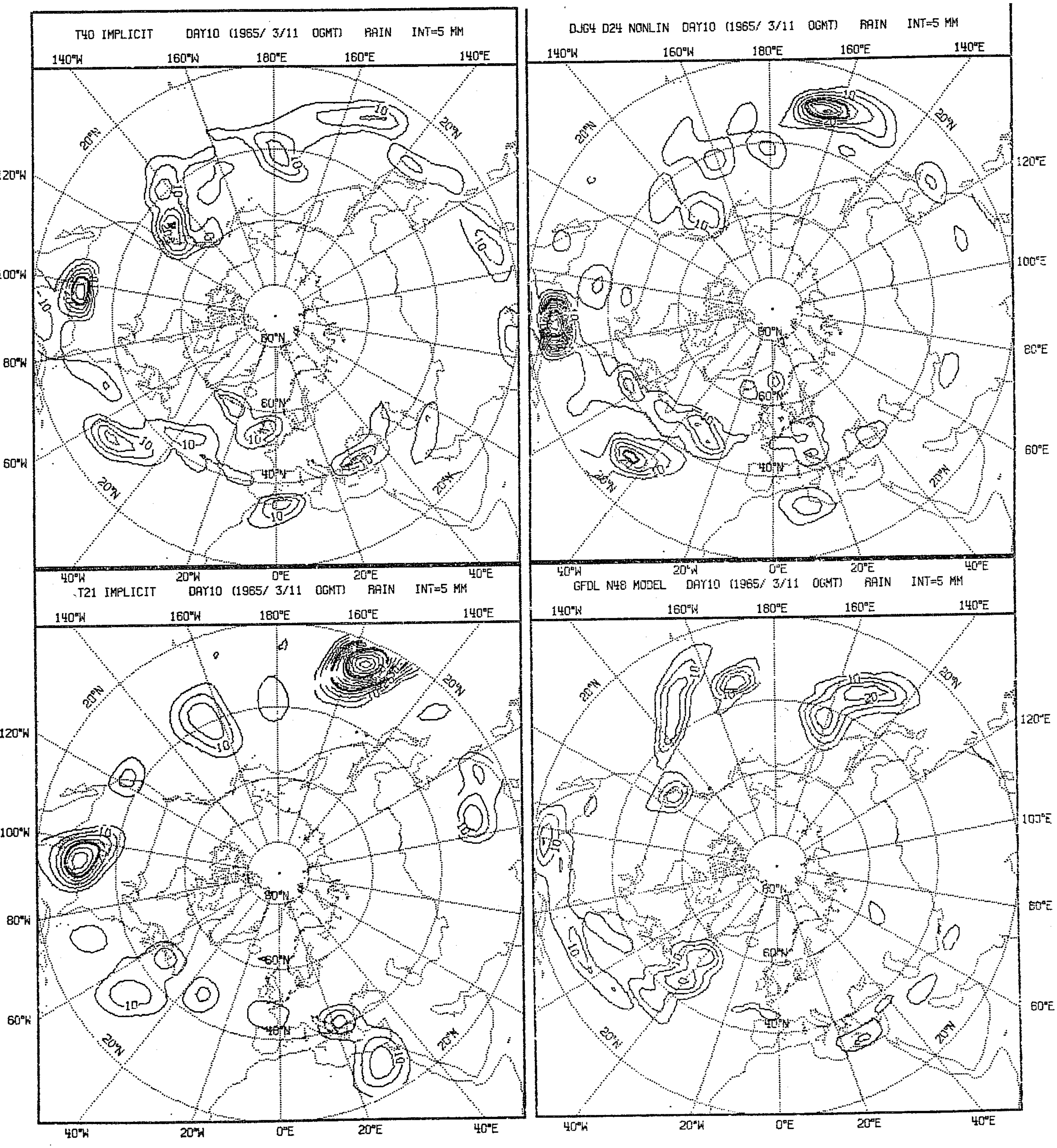

a.

b.

Fig. 3.4.3 Predicted 24h accumulated rainfall patterns over the northern hemisphere, day 10.

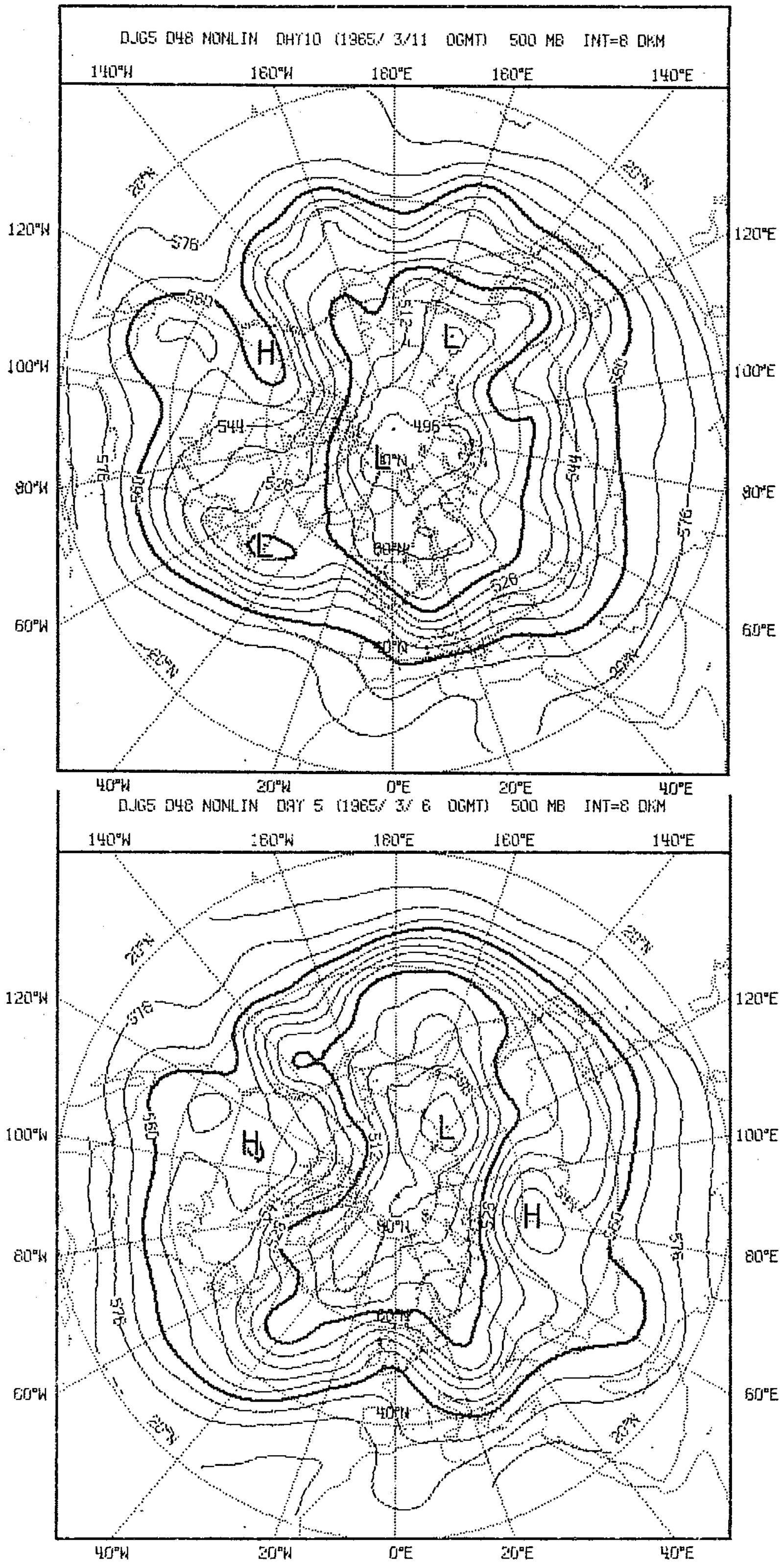

Fig. A1 Prediction of 500 mb geopotential height field by ECMWF's N48 model, day 5 (bottom) and day 9 (top).

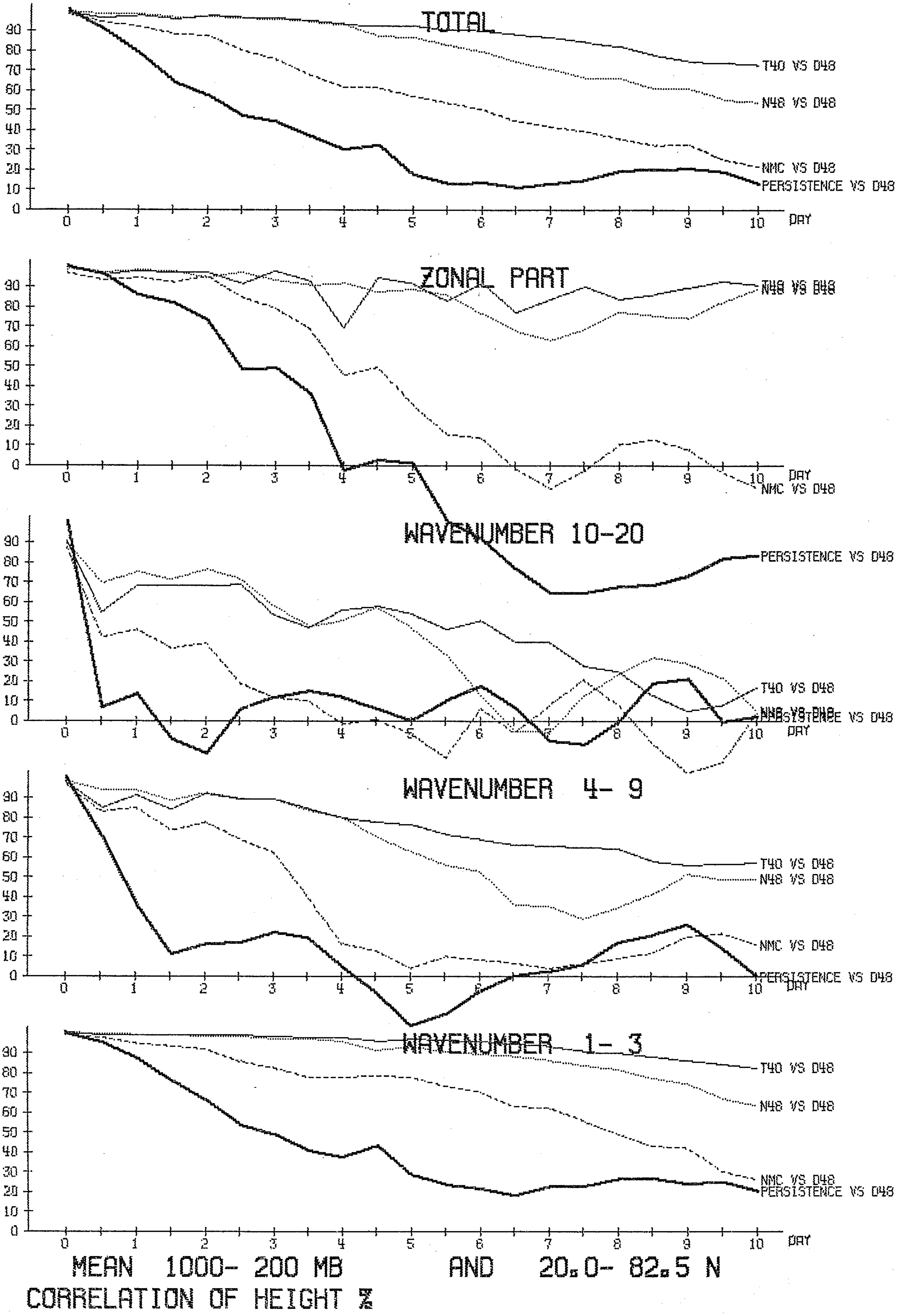
TOTAL
ZONAL PART
WAVENUMBER 10-20
WAVENUMBER 4- 9
WAVENUMBER 1- 3
0
10
20
30
40
50
60
70
80
90
0
1
2
3
4
5
6
7
8
9
10
DAY
T40 VS D48
N48 VS D48
NMC VS D48
PERSISTENCE VS D48
MEAN 1000- 200 MB AND 20.0- 82.5 N
CORRELATION OF HEIGHT %

Fig. A2

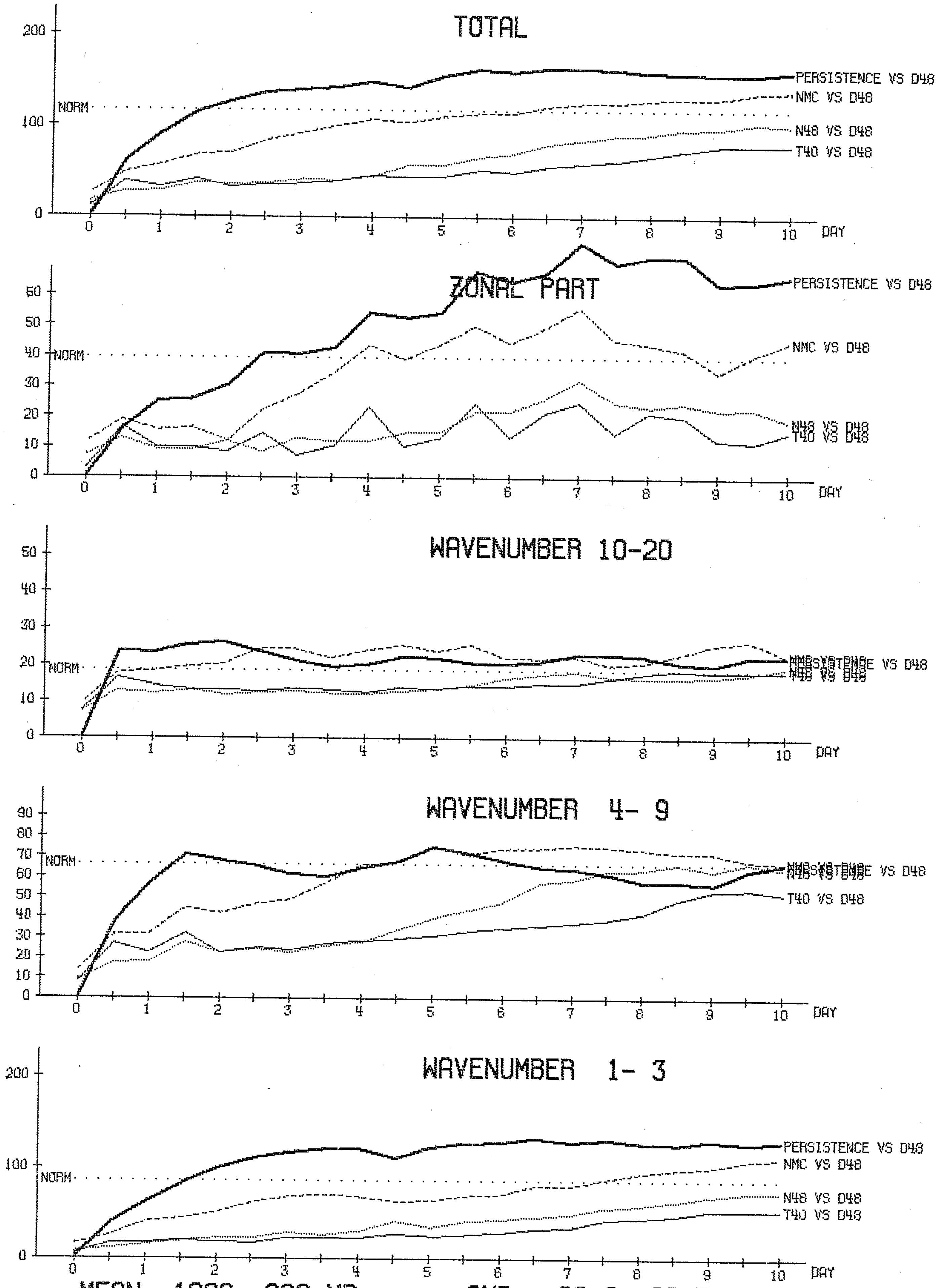

MEAN 1000- 200 MB AND 20.0- 82.5 N
RMS HEIGHT DIFFERENCES (M)

Fig. A3

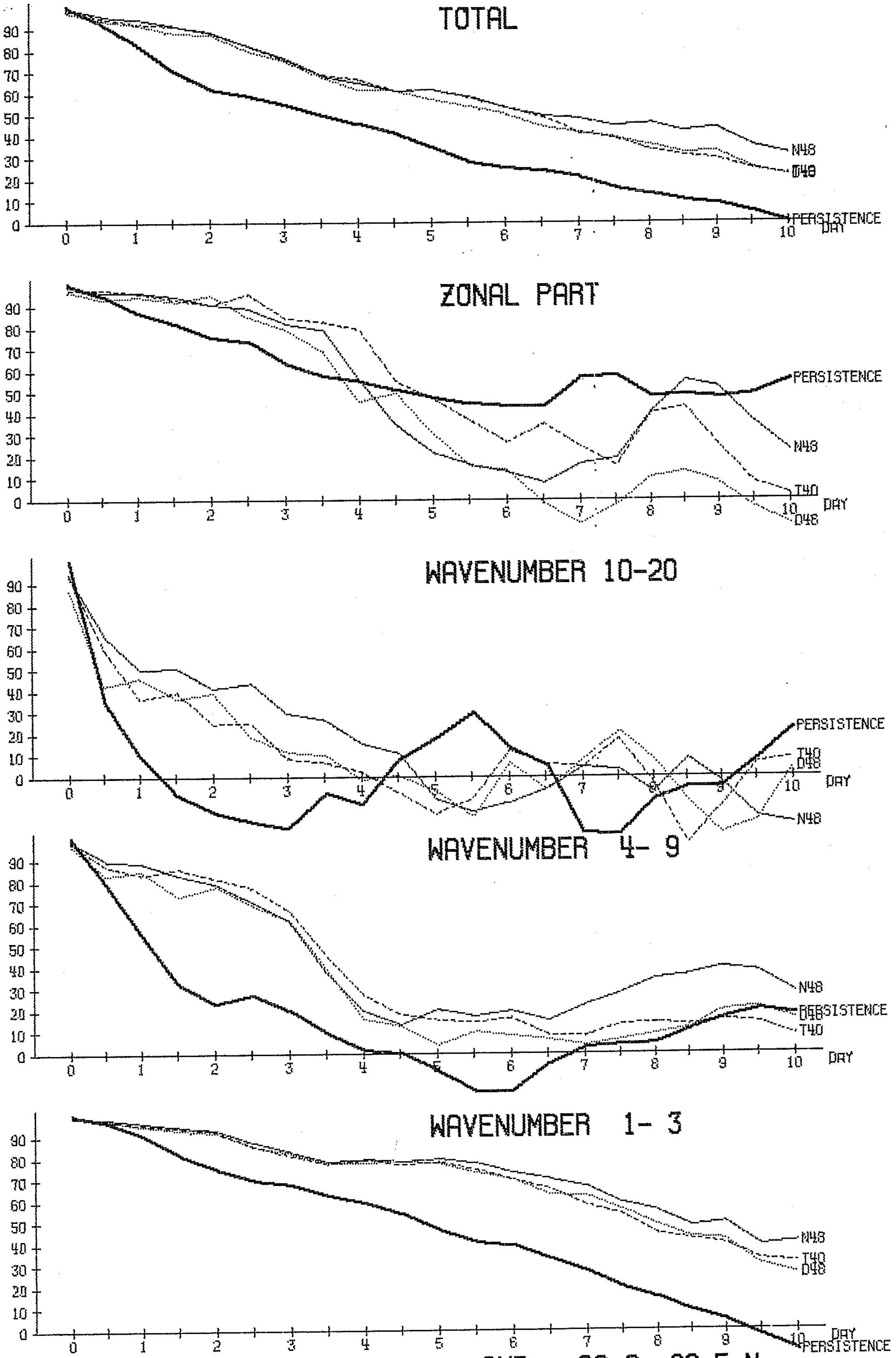

MEAN 1000- 200 MB AND 20.0- 82.5 N
CORRELATION OF HEIGHT %

Fig. A4

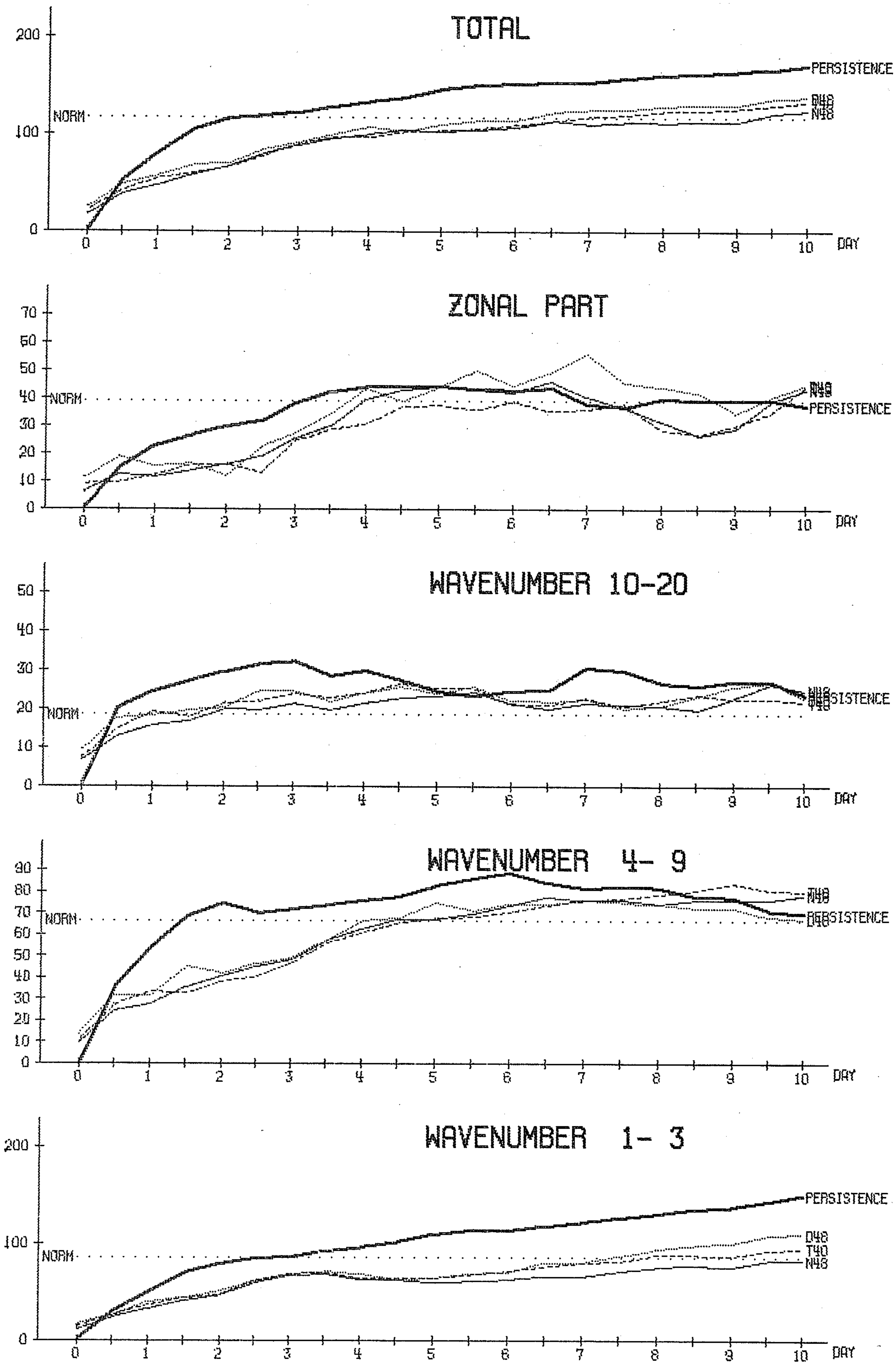

MEAN 1000- 200 MB AND 20.0- 82.5 N

RMS ERROR OF HEIGHT (M)

Fig. A5

References

Arpe, K., Bengtsson, L., Hollingsworth, A. and Janjic, Z.	(1976)	A case study of a ten day prediction. ECMWF Technical Report No. 1, 105 pp.
Bourke, W.	(1974)	A multi-level spectral model. I. Formulation and hemispheric integrations. Mo. Wea. Rev. 102, pp. 687-701.
Bourke, W., McAveney,B. Puri, K. and Thurling,R.	(1977)	Global modelling of atmospheric flow by spectral methods. Methods in Computational Physics, Vol. 17 Ed. J.Chang, Academic Press, 1977, pp.267-324.
Daley, R., Girard,C., Henderson, J. and Simmonds, I.	(1976A)	Short-term forecasting with a multi-level spectral primitive equation model. Part I - Model Formulation. Atmosphere 14, pp.98-116.
Daley, R., Girard C., Henderson,J. and Simmonds,I.	(1976B)	Part II - Hemispheric Prognoses and Verification. Atmosphere 14, pp.117-134.
Druyan, L.M. Somerville, R.C.J. and Quirk, W.J.	(1975)	Extended range forecasts with the GISS model of the global atmosphere. Tech.Note Inst. for Space Studies, Goddard Space Flight Centre, NASA, N.Y.
Gauntlett, D.J. Burridge,D.M. and Arpe, K.	(1977)	Comparative extended range numerical integrations with the ECMWF global forecasting model 1: The N24, non-adiabatic experiment. ECMWF Internal Report No. 6, 86 pp.

References:

Hansen, A.W. and Baede, A.P.M.	(1977)	ECMWF - Internal Report No. 15 -to be published-
Hoskins, B.J. and Simmons, A.J.	(1975)	A multi-layer spectral model and the semi-implicit method. Quart.J.R.Met.Soc.101, pp. 637-655.
Manabe, S. and Strickler,R.F.	(1964)	Thermal equilibrium of the atmosphere with a convective adjustment. J.A.S. 21 pp.361-385.
Manabe, S. and Wetherald, R.T.	(1967)	Thermal equilibrium of the atmosphere with a given distribution of relative humidity. J.A.S. 24, pp.241-259.
Miyakoda, K.	(1973)	Cumulative results of testing a mathematical model. The description of the model. Proc.Royal Irish Academy 73A, pp. 99-130.
Miyakoda, K., Hembree,G.D., Strickler, R.F. and Spelman,I.	(1972)	Cumulative results of extended forecast experiments. I. Model performance for Winter cases. M.W.R.,Vol.10, pp. 836-855.
Miyakoda,K., Moyer,R.W.,Stambler,H., Clarke, R.H. and Strickler,R.F.		A prediction experiment with a global model on the Kurihara Grid. Journal of Met. Soc. of Japan, 49, pp.521 - 536.
Miyakoda,K. Sadler, J.C. and Hembree, G.D.	(1970)	Numerical simulation of the breakdown of a polar-night-vortex in the stratosphere. Journal of Atm.Sci.,27, pp. 139-154.

References:

Simmons, A.J., Hoskins, B.J. and Burridge,D.M. (1977) To be published

Somerville, R.C.J., Stone, P.H., Halem, M., Hansen,J.E., Hogan,J.S., Duyan,L.M., Russel,G., Lacis,A.A., Quirk, W.J. and Tenenbaum, J. (1974) The GISS Model of the global atmosphere. J. Atmos. Sci. 31, pp. 84-117.

EUROPEAN CENTRE FOR MEDIUM RANGE WEATHER FORECASTS

Research Department (RD)

Technical Report No. 7

No. 1 A Case Study of a Ten Day Prediction

No. 2 The Effect of Arithmetic Precision on some Meteorological Integrations

No. 3 Mixed-Radix Fast Fourier Transforms without Reordering

No. 4 A Model for Medium Range Weather Forecasting - Adiabatic Formulation -

No. 5 A Study of some Parameterizations of Sub-Grid Processes in a Baroclinic Wave in a Two-Dimensional Model

No. 6 The ECMWF Analysis and Data-Assimilation Scheme: - Analysis of Mass and Wind Fields -

No. 7 A Ten-Day High-Resolution Non-Adiabatic Spectral Integration ; A Comparative Study

ECMWF LIBRARY